

2016-01-01

# Gravimetrically Characterizable Common Alkali Reducing Agents And Ligand Design Of A New Electron Rich Guanidinate

Efrain Maximiliano Castillo

University of Texas at El Paso, emcastillo2@miners.utep.edu

Follow this and additional works at: [https://digitalcommons.utep.edu/open\\_etd](https://digitalcommons.utep.edu/open_etd)

 Part of the [Inorganic Chemistry Commons](#), and the [Organic Chemistry Commons](#)

---

## Recommended Citation

Castillo, Efrain Maximiliano, "Gravimetrically Characterizable Common Alkali Reducing Agents And Ligand Design Of A New Electron Rich Guanidinate" (2016). *Open Access Theses & Dissertations*. 820.  
[https://digitalcommons.utep.edu/open\\_etd/820](https://digitalcommons.utep.edu/open_etd/820)

This is brought to you for free and open access by DigitalCommons@UTEP. It has been accepted for inclusion in Open Access Theses & Dissertations by an authorized administrator of DigitalCommons@UTEP. For more information, please contact [lweber@utep.edu](mailto:lweber@utep.edu).

GRAVIMETRICALLY CHARACTERIZABLE COMMON ALKALI  
REDUCING AGENTS AND LIGAND DESIGN OF A NEW ELECTRON RICH  
GUANIDINATE

EFRAIN MAXIMILIANO CASTILLO NORIS

Master's Program in Chemistry

APPROVED:

---

Skye Fortier, Ph.D., Chair

---

Dino Villagran, Ph.D.

---

Carl Dirk, Ph.D.

---

Chunqiang Li, Ph.D.

---

Charles Ambler, Ph.D.  
Dean of the Graduate School

Copyright ©

by

<Efrain M. Castillo>

<2016>

## **Dedication**

To my parents Efrain and Marcela and brother Emiliano for always supporting me in following my dreams.

GRAVIMETRICALLY CHARACTERIZABLE COMMON ALKALI  
REDUCING AGENTS AND LIGAND DESIGN OF A NEW ELECTRON RICH  
GUANIDINATE

by

EFRAIN MAXIMILIANO CASTILLO NORIS, B.S.

THESIS

Presented to the Faculty of the Graduate School of  
The University of Texas at El Paso  
in Partial Fulfillment  
of the Requirements  
for the Degree of

MASTER OF SCIENCE

Department of Chemistry  
THE UNIVERSITY OF TEXAS AT EL PASO

August 2016

## **Acknowledgements**

First and foremost, I would like to thank my advisor Dr. Skye Fortier for all the teachings, support, guidance and grilling needed for me to succeed as a chemist as well as being an inspiring example for me as an inorganic chemist.

I would also like to thank my committee members Dr. Villagran and Dr. Dirk for the continuous advise and help through my development. Special thanks to Dr. Maity for the day to day constructive talks in the laboratory, Dr. Salvador for inspiring me through his words and Dr. Michael for opening the door of research to me as an undergraduate.

I thank my current lab partners Rolando, Duer and David for all the quick chats about chemistry, all the laughs and tears we had to overcome during these 2 years. I thank my undergraduate student Omar, currently pursuing a Ph.D. in Chemistry, for all the work we did together and how we grew together in the lab. I would also like to thank Leonel, Brenda, Aldo and Joe for all the fun we had together in the lab.

Finally I thank my former lab mates Andrew, Alfredo, Luis and Nate for forming me in my early undergraduate research career. I thank the Villagran lab members for their strong support and help with project development as well as for being my continuous liquid nitrogen supply.

## Table of Contents

Acknowledgements.....	v
Table of Contents.....	vi
List of Tables .....	vii
List of Figures.....	viii
List of Schemes.....	xi
Chapter 1: Synthesis, characterization and isolation of alkali metal radical arenides using 18-crown-6.....	1
1.1 Introduction.....	1
1.2 Synthetic approach.....	3
1.3 Experimental considerations.....	4
1.4 General synthesis of $[M(18-c-6)(Solvent)_x][Arene]^{-\bullet}$ .....	5
1.5 Results and discussion .....	12
1.6 Conclusion .....	16
References.....	18
Chapter 2: Synthesis of a strong electron-donating guanidinate containing an imidazolin-2-iminato backbone and its properties on iron. ....	20
2.1 Introduction.....	20
2.2 Experimental considerations.....	23
2.3 Synthetic details.....	23
2.4 Results and discussion .....	26
2.5 Conclusion .....	34
References.....	35
Appendix.....	38
Vita .....	97

## List of Tables

<b>Table 1.1</b> Isolated arene radical monoanions and electronic properties .....	11
<b>Table 2.1</b> X-ray crystallographic data for <b>13</b> and <b>16</b> . ....	29
<b>Table S1.</b> Electrochemical data for <b>1</b> in DME (vs. $[\text{Cp}_2\text{Fe}]^{0/+}$ ).....	53
<b>Table S2.</b> Electrochemical data for <b>2</b> in DME (vs. $[\text{Cp}_2\text{Fe}]^{0/+}$ ).....	54
<b>Table S3.</b> Electrochemical data for <b>3</b> in DME (vs. $[\text{Cp}_2\text{Fe}]^{0/+}$ ).....	55
<b>Table S4</b> Electrochemical data for <b>4</b> in DME (vs. $[\text{Cp}_2\text{Fe}]^{0/+}$ ).....	56
<b>Table S5</b> Electrochemical data for <b>5</b> in DME (vs. $[\text{Cp}_2\text{Fe}]^{0/+}$ ).....	57
<b>Table S6</b> Electrochemical data for <b>6</b> in DME (vs. $[\text{Cp}_2\text{Fe}]^{0/+}$ ).....	58
<b>Table S7</b> Electrochemical data for <b>7</b> in DME (vs. $[\text{Cp}_2\text{Fe}]^{0/+}$ ).....	59
<b>Table S8.</b> Electrochemical data for <b>8</b> in DME (vs. $[\text{Cp}_2\text{Fe}]^{0/+}$ ).....	60
<b>Table S9.</b> Electrochemical data for <b>9</b> in DME (vs. $[\text{Cp}_2\text{Fe}]^{0/+}$ ).....	61
<b>Table S10.</b> Electrochemical data for <b>10</b> in DME (vs. $[\text{Cp}_2\text{Fe}]^{0/+}$ ).....	63
<b>Table S11.</b> Electrochemical data for <b>11</b> in DME (vs. $[\text{Cp}_2\text{Fe}]^{0/+}$ ).....	65
<b>Table S12</b> Electrochemical data for <b>12</b> in DME (vs. $[\text{Cp}_2\text{Fe}]^{0/+}$ ).....	66
<b>Table S13</b> X-ray crystallographic data for <b>1-12</b> .....	79
<b>Table S14</b> Electrochemical data for <b>16</b> in Fig. 2.3 in THF (vs. $[\text{Cp}_2\text{Fe}]^{0/+}$ ). ....	96



## List of Figures

<b>Figure 1.1</b> Solid-state molecular structure of <b>3</b> with 50% probability ellipsoids and respective bond length (Å) diagram. Asterisks denote symmetry generated atoms and bond lengths.....	12
<b>Figure 1.2</b> Solid-state molecular structure of <b>4</b> with 50% probability ellipsoids and respective bond length (Å) diagram.....	13
<b>Figure 1.3</b> Solid-state molecular structure of <b>10</b> with 50% probability ellipsoids and respective bond length (Å) diagram. Asterisks denote symmetry generated atoms and bond lengths.....	14
<b>Figure 1.4</b> Solid-state molecular structure of <b>5</b> with 50% probability ellipsoids and respective bond length (Å) diagram.....	15
<b>Figure 2.1</b> ORTEP diagram of <b>13</b> (top) and <b>16</b> ·C <sub>7</sub> H <sub>8</sub> (bottom). Hydrogens and the co-crystallized molecule of toluene omitted for clarity. ....	30
<b>Figure 2.2</b> Room temperature electronic absorption spectra for <b>16</b> (0.10 mM; blue), <b>5a</b> (0.09 mM; green), and <b>6a</b> (0.15 mM; red) in THF. ....	32
<b>Figure 2.3</b> Cyclic voltammogram of <b>16</b> in THF with [NBu <sub>4</sub> ][PF <sub>6</sub> ] as supporting electrolyte (vs [Cp <sub>2</sub> Fe] <sup>0/+</sup> ).....	33
<b>Figure S1.</b> Solid-state molecular structure of <b>1</b> with 50% probability ellipsoids and respective bond length diagram. ....	38
<b>Figure S3.</b> Solid-state molecular structure of <b>6</b> with 50% probability ellipsoids and respective bond length diagram. ....	40
<b>Figure S4.</b> Diagram of the incompletely refined molecular structure of <b>7</b> presented to demonstrate connectivity only. ....	41
<b>Figure S5.</b> Solid-state molecular structure of <b>8</b> with 50% probability ellipsoids and respective bond length diagram. Asterisks denote symmetry generated atoms and bond lengths. ....	42
<b>Figure S6.</b> Solid-state molecular structure of <b>9</b> with 50% probability ellipsoids and respective bond length diagram. ....	43
<b>Figure S7.</b> Solid-state molecular structure of <b>11</b> with 50% probability ellipsoids and respective bond length diagram. Asterisks denote symmetry generated atoms and bond lengths. ....	44
<b>Figure S8.</b> Solid-state molecular structure of <b>12</b> with 50% probability ellipsoids and respective bond length diagram. ....	45
<b>Figure S9.</b> Room temperature UV/vis-NIR absorption spectra for <b>1</b> (THF, 0.106 mM), <b>2</b> (THF, 0.139 mM), and <b>3</b> (THF, 0.114 mM).....	46
<b>Figure S10.</b> Room temperature UV/vis-NIR absorption spectra for <b>4</b> (THF, 0.284 mM), <b>5</b> (THF, 0.284 mM), and <b>6</b> (THF, 0.284 mM).....	47
<b>Figure S11.</b> Room temperature UV/vis-NIR absorption spectra for <b>10</b> (THF, 0.036 mM), <b>11</b> (THF, 0.052 mM), and <b>12</b> (THF, 0.054 mM).....	48
<b>Figure S12.</b> Room temperature cyclic voltammogram of <b>1</b> , <b>2</b> and <b>3</b> in DME (50mV/s scan rate) vs. [Cp <sub>2</sub> Fe] <sup>0/+</sup> . (0.1M [NBu <sub>4</sub> ][PF <sub>6</sub> ] as supporting electrolyte).....	49
<b>Figure S13.</b> Room temperature cyclic voltammogram of <b>4</b> (50mV/s scan rate), <b>5</b> (200mV/s scan rate) and <b>6</b> (50mV/s scan rate) in DME vs [Cp <sub>2</sub> Fe] <sup>0/+</sup> . (0.1M [NBu <sub>4</sub> ][PF <sub>6</sub> ] as supporting electrolyte).....	50
<b>Figure S14.</b> Room temperature cyclic voltammogram of <b>7</b> (50mV/s scan rate), <b>8</b> (300mV/s scan rate) and <b>9</b> (200mV/s scan rate) in DME vs [Cp <sub>2</sub> Fe] <sup>0/+</sup> . (0.1M [NBu <sub>4</sub> ][PF <sub>6</sub> ] as supporting electrolyte).....	51
<b>Figure S15.</b> Room temperature cyclic voltammogram of <b>10</b> , <b>11</b> and <b>12</b> in DME (200mV/s scan rate) vs [Cp <sub>2</sub> Fe] <sup>0/+</sup> . (0.1M [NBu <sub>4</sub> ][PF <sub>6</sub> ] as supporting electrolyte).....	52
<b>Figure S16.</b> Room temperature cyclic voltammogram of <b>1</b> in DME (vs [Cp <sub>2</sub> Fe] <sup>0/+</sup> ). (0.1M [NBu <sub>4</sub> ][PF <sub>6</sub> ] as supporting electrolyte).....	53

<b>Figure S17.</b> Room temperature cyclic voltammogram of <b>2</b> in DME (vs [Cp <sub>2</sub> Fe] <sup>0/+</sup> ). (0.1M [NBu <sub>4</sub> ][PF <sub>6</sub> ] as supporting electrolyte).....	54
<b>Figure S18.</b> Room temperature cyclic voltammogram of <b>3</b> in DME (vs [Cp <sub>2</sub> Fe] <sup>0/+</sup> ). (0.1M [NBu <sub>4</sub> ][PF <sub>6</sub> ] as supporting electrolyte).....	55
<b>Figure S19.</b> Room temperature cyclic voltammogram of <b>4</b> in DME (vs [Cp <sub>2</sub> Fe] <sup>0/+</sup> ). (0.1M [NBu <sub>4</sub> ][PF <sub>6</sub> ] as supporting electrolyte).....	56
<b>Figure S20.</b> Room temperature cyclic voltammogram of <b>5</b> in DME (vs [Cp <sub>2</sub> Fe] <sup>0/+</sup> ). (0.1M [NBu <sub>4</sub> ][PF <sub>6</sub> ] as supporting electrolyte).....	57
<b>Figure S21.</b> Room temperature cyclic voltammogram of <b>6</b> in DME (vs [Cp <sub>2</sub> Fe] <sup>0/+</sup> ). (0.1M [NBu <sub>4</sub> ][PF <sub>6</sub> ] as supporting electrolyte).....	58
<b>Figure S22.</b> Room temperature cyclic voltammogram of <b>7</b> in DME (vs [Cp <sub>2</sub> Fe] <sup>0/+</sup> ). (0.1M [NBu <sub>4</sub> ][PF <sub>6</sub> ] as supporting electrolyte).....	59
<b>Figure S23.</b> Room temperature cyclic voltammogram of <b>8</b> in DME (vs [Cp <sub>2</sub> Fe] <sup>0/+</sup> ). (0.1M [NBu <sub>4</sub> ][PF <sub>6</sub> ] as supporting electrolyte).....	60
<b>Figure S24.</b> Room temperature cyclic voltammogram of <b>9</b> in DME (vs [Cp <sub>2</sub> Fe] <sup>0/+</sup> ). (0.1M [NBu <sub>4</sub> ][PF <sub>6</sub> ] as supporting electrolyte).....	61
<b>Figure S25.</b> Room temperature cyclic voltammogram of <b>10</b> in DME (vs [Cp <sub>2</sub> Fe] <sup>0/+</sup> ). (0.1M [NBu <sub>4</sub> ][PF <sub>6</sub> ] as supporting electrolyte).....	62
<b>Figure S26.</b> Room temperature cyclic voltammogram of <b>11</b> in DME (vs [Cp <sub>2</sub> Fe] <sup>0/+</sup> ). (0.1M [NBu <sub>4</sub> ][PF <sub>6</sub> ] as supporting electrolyte).....	64
<b>Figure S27.</b> IR spectrum (KBr pellet) of <b>1</b> . ....	67
<b>Figure S28.</b> IR spectrum (KBr pellet) of <b>2</b> . ....	68
<b>Figure S29.</b> IR spectrum (KBr pellet) of <b>3</b> . ....	69
<b>Figure S30.</b> IR spectrum (KBr pellet) of <b>4</b> . ....	70
<b>Figure S31.</b> IR spectrum (KBr pellet) of <b>5</b> . ....	71
<b>Figure S32.</b> IR spectrum (KBr pellet) of <b>6</b> . ....	72
<b>Figure S33.</b> IR spectrum (KBr pellet) of <b>7</b> . ....	73
<b>Figure S34.</b> IR spectrum (KBr pellet) of <b>8</b> . ....	74
<b>Figure S35.</b> IR spectrum (KBr pellet) of <b>9</b> . ....	75
<b>Figure S35.</b> IR spectrum (KBr pellet) of <b>10</b> . ....	76
<b>Figure S36.</b> IR spectrum (KBr pellet) of <b>11</b> . ....	77
<b>Figure S37.</b> IR spectrum (KBr pellet) of <b>12</b> . ....	78
<b>Figure S38.</b> <sup>1</sup> H NMR spectrum of <b>13</b> in C <sub>6</sub> D <sub>6</sub> at 25 °C. ....	82
<b>Figure S39.</b> <sup>13</sup> C NMR spectrum of <b>13</b> in C <sub>6</sub> D <sub>6</sub> at 25 °C. ....	83
<b>Figure S40.</b> <sup>7</sup> Li NMR spectrum of <b>13</b> in C <sub>6</sub> D <sub>6</sub> at 25 °C. ....	84
<b>Figure S41.</b> IR spectrum (KBr pellet) of <b>13</b> . ....	85
<b>Figure S42.</b> <sup>1</sup> H NMR spectrum of <b>14</b> in C <sub>6</sub> D <sub>6</sub> at 25 °C. Asterisks denote the presence of residual Et <sub>2</sub> O. ....	86
<b>Figure S43.</b> <sup>13</sup> C NMR spectrum of <b>14</b> in C <sub>6</sub> D <sub>6</sub> at 25 °C. Asterisks denote the presence of residual Et <sub>2</sub> O. ....	87
<b>Figure S44.</b> ESI mass spectrum of <b>14</b> . Asterisk denotes - <sup>t</sup> Bu fragmentation of a group from the imidazolin-2-iminato ring ([M+H- <sup>t</sup> Bu] <sup>+</sup> ; calcd m/z 502.39). ....	88
<b>Figure S45.</b> IR spectrum (KBr pellet) of <b>14</b> . Asterisk denotes background subtraction error. ....	89
<b>Figure S46.</b> <sup>1</sup> H NMR spectrum of <b>15</b> in C <sub>6</sub> D <sub>6</sub> at 25 °C. ....	90
<b>Figure S47.</b> <sup>13</sup> C NMR spectrum of <b>15</b> in C <sub>6</sub> D <sub>6</sub> at 25 °C. ....	91
<b>Figure S48.</b> IR spectrum (KBr pellet) of <b>15</b> . Asterisk denotes background subtraction error. ....	92
<b>Figure S49.</b> <sup>1</sup> H NMR spectrum of <b>16</b> in C <sub>6</sub> D <sub>6</sub> at 25 °C. ....	93
<b>Figure S50.</b> IR spectrum (KBr pellet) of <b>16</b> . Asterisk denotes background subtraction error. ....	94

<b>Figure S51.</b> Room temperature cyclic voltammogram of <b>16</b> in THF vs $[\text{Cp}_2\text{Fe}]^{0/+}$ using 0.1 M $[\text{nBu}_4][\text{PF}_6]$ as supporting electrolyte.....	95
--	----

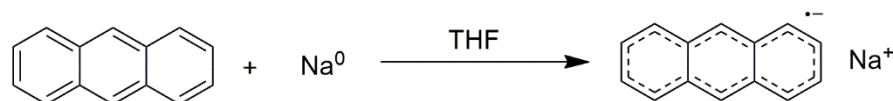
## List of Schemes

<b>Scheme 1.1</b> Synthesis of Sodium Anthracenide, the first reported arene radical. <sup>3</sup> .....	1
<b>Scheme 1.2</b> Examples of previously isolated metal arenides.....	2
<b>Scheme 1.3</b> Synthetic steps for $M[(18\text{-c-}6)(\text{THF})_n][\text{arene}]$ .....	3
<b>Scheme 2.1</b> Possible resonance structures of ketimine and $\text{Im}^{\text{R}}\text{N}$ functionalized guanidines, D–G, and H–K, respectively. ....	20
<b>Scheme 2.2</b> Resonance forms of the $\text{Im}^{\text{R}}\text{N}$ - ligand.....	21
<b>Scheme 2.3</b> Examples of neutral ligands incorporating the $\text{Im}^{\text{R}}\text{N}$ - functionality and their limiting resonance forms. ....	22
<b>Scheme 2.4</b> Synthesis of $[\text{Li}(\text{THF})_2][(\text{Im}^{\text{tBu}}\text{N})\text{C}(\text{Ndipp})_2]$ ( <b>13</b> ).....	27
<b>Scheme 2.5</b> Synthesis of $\{[(\text{Im}^{\text{tBu}}\text{N})\text{C}(\text{Ndipp})_2]\text{FeBr}\}_2$ ( <b>16</b> ).....	28
<b>Scheme 2.6</b> Comparison of selected bond distances (Å) and angles (°) in <b>13</b> and <b>16</b> vs. <b>5a</b> and <b>6a</b> .....	31

# Chapter 1: Synthesis, characterization and isolation of alkali metal radical arenides using 18-crown-6.<sup>1</sup>

## 1.1 Introduction

From the time since Schlenk reported the synthesis of the first arene radical “sodium anthracenide” in 1914 (Scheme 1.1),<sup>2</sup> alkali metals have been used extensively to reduce arenes over the past century.<sup>3</sup> This reduction is possible due to the low-energy  $\pi^*$  LUMO in the arene, which upon reduction gives deeply colored arenides. From an electronic standpoint, arenides display novel aromaticity and have been shown to exhibit long-range magnetic ordering in the solid-state.<sup>5-10</sup> These radical arenides are commonly used as anionic polymerization initiators,<sup>11</sup> strong bases,<sup>4,12</sup> graphitic battery materials,<sup>13</sup> and are important intermediates observed in Birch reductions.<sup>14</sup> However, arenides are most commonly known as potent outer-sphere one-electron reducing agents.

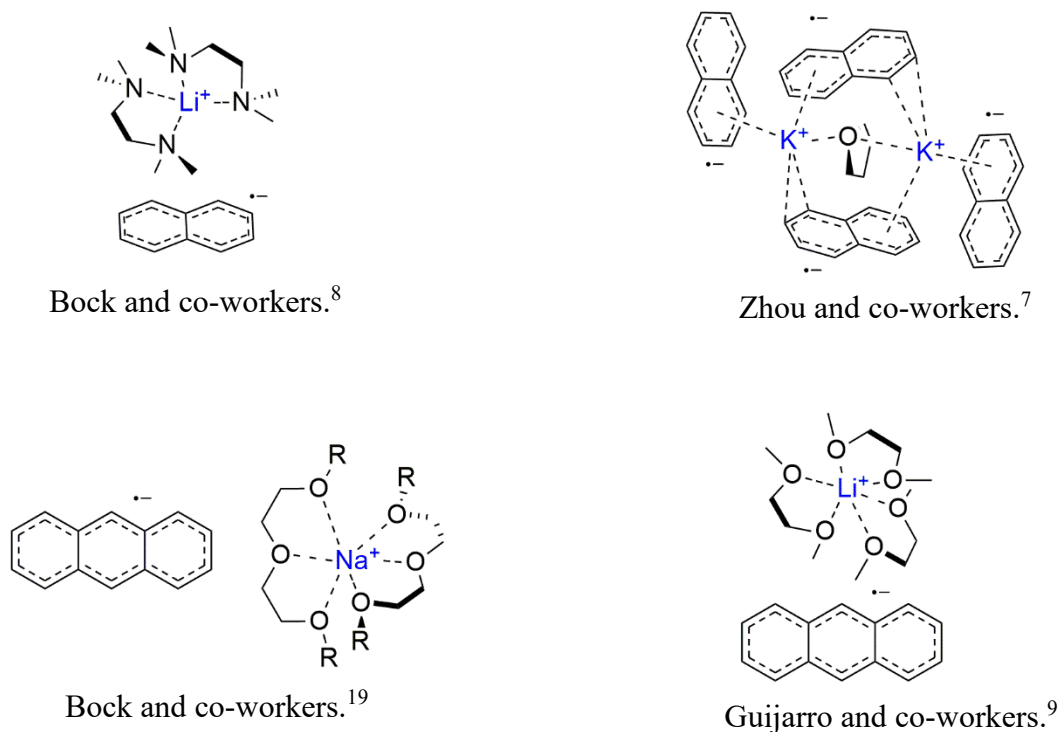


**Scheme 1.1** Synthesis of Sodium Anthracenide, the first reported arene radical.<sup>3</sup>

Alkali metal derivatives of  $C_{10}H_8^{\bullet-}$ ,  $C_{12}H_{10}^{\bullet-}$ ,  $C_{14}H_{10}^{\bullet-}$  and  $C_{20}H_{12}^{\bullet-}$  are readily used as strong reductants. However, isolating these species is not straight forward for a number of reasons. Because of their radical nature, these compounds are prone to decomposition under air or aqueous conditions thus requiring strict anaerobic and anhydrous handling and preparation.<sup>15</sup> Moreover, these radical species are kinetically unstable and have short storage times, compromising the integrity of the arenide in a solvent-dependent equilibrium.<sup>4,16,17</sup> For those reasons, alkali arenide solutions have to be prepared *in situ* before use and require multi-step titrations to ensure correct concentration.<sup>15</sup> As shown, several complications

<sup>1</sup> This chapter previously appeared as an article in the New Journal of Chemistry. The original citation is as follows: Castillo, M.; Metta-Magana, A. J.; Fortier, S.; Isolation of gravimetrically quantifiable alkali metal arenides using 18-crown-6, *New J. Chem.*, **2016**, 40, pp. 1923-1926

put a limit on the storage, handling, and identity of these reducing agents, affecting the utility and ability to gravimetrically measure exact amounts.



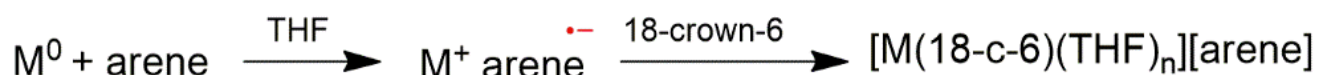
**Scheme 1.2** Examples of previously isolated metal arenides.

Despite this, a few radical arenides using various alkali metals under different reaction and crystallization conditions have been isolated and characterized in the solid-state.<sup>6-10,14,18</sup> Of the few isolated, Bock and co-workers characterized a set of alkali arenides by XRD including  $[\text{Na}(\text{triglyme})_2][\text{C}_{14}\text{H}_{10}]$ ,<sup>8</sup>  $[\text{M}(\text{solvent})_n][\text{C}_{20}\text{H}_{12}]$  ( $\text{M} = \text{Li}$ , solvent = DME,  $n = 3$ ;  $\text{M} = \text{Na/K}$ , solvent = triglyme,  $n = 2$ ;  $\text{M} = \text{Cs}$ , solvent = tetraglyme,  $n = 2$ ),<sup>19</sup> with specific combinations of solvent, metal and arene for each compound. Additionally, Guijarro and co-workers successfully isolated  $[\text{Li}(\text{tmeda})_2][\text{C}_{10}\text{H}_8]$ <sup>9</sup> and Zhou and co-workers reported the doubly reduced arene  $\text{K}_2(\text{THF})(\text{C}_{10}\text{H}_8)$  shown in Scheme 1.2.<sup>7</sup> Among the previously known alkali metal arenides, the isolation of  $[\text{K}(18\text{-c-}6)(\text{THF})_2][\text{C}_{10}\text{H}_8]^\bullet$  and  $[\text{K}(18\text{-c-}6)(\text{THF})_2][\text{C}_{14}\text{H}_{10}]^\bullet$  was achieved by Kochi solely for the study of structural changes in aromatic systems bearing radical character.<sup>6</sup>

Having discussed the importance of these isolated examples, there is a lack of a general straightforward procedure to isolate the widely utilized popular arenides  $C_{10}H_8^{\bullet-}$ ,  $C_{12}H_{10}^{\bullet-}$ ,  $C_{14}H_{10}^{\bullet-}$  and  $C_{20}H_{12}^{\bullet-}$  in a solid form. Attempting to address this problem, we sought to find a method to isolate a set of alkali arenides in the solid form providing a known composition and well-defined properties.

Herein we report the synthesis, characterization and isolation of twelve common radical arenes with reduction potentials ranging between -2.2 V and -3.2 V (vs  $Fc^{0/+}$ ). Single crystal X-ray diffraction, UV-vis/NIR and Infrared spectroscopy, solid state magnetic susceptibility and cyclic voltammetry were used to characterize the isolated arenes in this study.

## 1.2 SYNTHETIC APPROACH



**Scheme 1.3** Synthetic steps for  $M[(18\text{-c-6})(\text{THF})_n][\text{arene}]$

We found that storing concentrated solutions of the arenides ( $M = \text{Li, Na, K}$ ; arene = Biphenyl, Anthracene, Naphthalene) at  $-25^\circ\text{C}$  produced deeply-colored blocks of crystals of the respective alkali arene pair in hours. Unfortunately, all attempts to isolate these crystals were unsuccessful, as removing the crystals from its solvent matrix compromised their integrity by through desolvation in seconds and forming oily intractable products. We hypothesized that stabilizing the alkali metal arenide anion pair by adding a chelating base would allow us to have isolable materials by avoiding solvent loss and molecular disproportionation.

Supported by our hypothesis, treatment of  $M[\text{Arene}]^{\bullet-}$  ( $M = \text{Li, Na, K}$ ; arene = Biphenyl, Anthracene, Naphthalene, Perylene) solution in THF with 1 equiv. of the polyether 18-crown-6 should yield crystalline material with the structure  $[M(18\text{-c-6})(\text{Solvent})_n][\text{Arene}]^{\bullet-}$  in all the cases. (Scheme 1.3).

### 1.3 EXPERIMENTAL CONSIDERATIONS

All air and moisture sensitive operations were performed in an M. Braun dry box under an atmosphere of purified nitrogen or using high-vacuum standard Schlenk techniques. DME, Hexanes and THF were dried using a Pure Process Technology Solvent Purification System and subsequently stored under a nitrogen atmosphere over activated 4 Å molecular sieves. Solvents denoted “cold” were placed in a -25°C freezer for at least 2 hours prior to use. 18-crown-6 was purchased from Oakwood Products, Inc. and made anhydrous using the Gokel method.<sup>24</sup> IR data were collected using a Thermo Scientific Nicolet iS5 spectrometer. UV-vis/NIR spectra were recorded on a Cary 5000 spectrophotometer. Cyclic voltammetric measurements were performed using a CH Instruments 600e potentiostat with a PC unit controlled with CHI software (version 13.12). Experiments were performed in a glovebox under an inert N<sub>2</sub> atmosphere using platinum disks (2 mm diameter), embedded in Kel-F thermoplastic, as the counter and working electrodes while the reference electrode consisted of a platinum wire. Solutions utilized in the electrochemical studies were approximately 1 mM in arene complex with [NBu<sub>4</sub>][PF<sub>6</sub>] (0.1M, THF) as supporting electrolyte. All potentials are reported versus the [Cp<sub>2</sub>Fe]<sup>0/+</sup> couple, referenced as internal standard. Data for **1-12** was collected on a Bruker 3-axis platform diffractometer equipped with a APEX I CCD detector using a graphite monochromator with a Mo Kα X-ray source ( $\alpha = 0.71073$  Å). The crystal was mounted on a Mitigen Kapton loop, coated in NVH oil, and maintained at 100(2) K under a flow of nitrogen gas during data collection. A hemisphere of data was collected using  $\omega$  and  $\phi$  scans with 0.3° frame widths. Data collection and cell parameter determination were conducted using the SMART program.<sup>25</sup> Integration of the data and final cell parameter refinements were performed using SAINT3 software with data absorption correction implemented through SADABS. 4 Structures were solved using direct, S4 charge flipping, or structure expansion methods and difference Fourier techniques. All hydrogen atom positions in **1-12** were idealized and rode on the atom. Structure solution, refinement, graphics, and creation of publication materials were performed using SHELXTL5 or the Olex2 crystallographic package.<sup>26</sup> Some of the coordinated THF molecules in **4-6** and **12** exhibit slight positional disorder which was addressed by modeling the disordered atoms over two orientations in a 50:50 ratio. A summary of relevant crystallographic data is presented in appendix Table S13. Weak



diffraction data precluded satisfactory structure refinement of **7**; however, a diagram illustrating its connectivity, based up the diffraction data, is shown in appendix Figure S4.

#### 1.4 GENERAL SYNTHESIS OF $[M(18-C-6)(SOLVENT)_X][ARENE]^{-}$

Freshly cut alkali metal pieces were added to a stirring solution of the aromatic hydrocarbon in THF. The reaction was left to stir for 4 h during which time the reaction mixture turned to a deep color. At this stage, any unreacted metal was removed and 18-crown-6 was added to the solution as a solid. After addition of the crown ether, the reaction mixture was stirred for 15 minutes. Storage of this solution at -25°C for 12 hours afforded a crop of crystals. The mixture was poured over a medium porosity glass frit and the collected crystals were washed with cold THF (1 x 5 mL) and cold hexanes (1 x 5 mL). The solid was dried under vacuum to give dark crystalline material.

##### 1.4.1 Synthesis of $[Li(18-c-6)][C_{10}H_8]$ , **1**.

The synthesis of **1** was performed using 0.113 g (0.881 mmol) of  $C_{10}H_8$  and 0.006 g (0.864 mmol) of lithium metal in 5 mL of THF to which 0.228 g (0.864 mmol) of 18-crown-6 was added. Yield: 0.128 g, 37%. Dark green crystals of **1** for X-ray crystallographic analysis were grown from a concentrated dark green THF solution stored at -25 °C. 1.53  $\mu B$  (Gouy measurement). UV-vis/NIR (THF, 0.106 mM, 25 °C,  $L \cdot mol^{-1} \cdot cm^{-1}$ ): 294 ( $\epsilon = 9173$ ), 318 ( $\epsilon = 4230$ ), 327 ( $\epsilon = 6584$ ), 376 ( $\epsilon = 2812$ ), 419 (sh,  $\epsilon = 1904$ ), 435 ( $\epsilon = 1764$ ), 468 ( $\epsilon = 1089$ ) 799 ( $\epsilon = 1284$ ). IR (KBr pellet): 3673(w), 3435(w), 3046(m), 3010(m), 2978(m), 2910(s), 2859(s), 2875(s), 2823(m), 2798(m), 2744(m), 2705(m), 2539(w), 2479(w), 2404(w), 2370(w), 2343(w), 2238(w), 2166(w), 2132(w), 1970(w), 1940(w), 1772(w), 1671(w), 1612(m), 1593(m), 1500(m), 1477(s), 1457(s), 1390(m), 1350(s), 1292(m), 1283(m), 1244(s), 1187(s), 1107(s), 1006(w), 993(m), 964(w), 927(m), 894(w), 836(m), 809(s), 783(m), 734(w), 711(m), 617(w), 593(m), 565(w), 531(w), 512(w), 482(m), 471(m), 441(w), 419(w).

##### 1.4.2 Synthesis of $[Na(18-c-6)DME][C_{10}H_8]$ , **2**.

While the initial synthesis of **2** was performed using THF followed by recrystallization from DME, it was found that the reaction can be performed in DME from the outset. Accordingly, **2** was synthesized using 0.142 g (1.107 mmol) of  $C_{10}H_8$  and 0.023 g (1.000 mmol) of sodium metal in 5 mL of

DME to which 0.262 g (0.991 mmol) of 18-crown-6 was added. Yield: 0.400 g, 79%. Dark green crystals of **2** for X-ray crystallographic analysis were grown from a concentrated dark green DME solution stored at -25 °C. 1.67  $\mu$ B (Gouy measurement). UV-vis/NIR (THF, 0.139 mM, 25 °C, L $\cdot$ mol $^{-1}$   $\cdot$ cm $^{-1}$ ): 294 ( $\epsilon$  = 10709), 322 (sh,  $\epsilon$  = 5364), 327 ( $\epsilon$  = 9057), 373 ( $\epsilon$  = 3140), 409 (sh,  $\epsilon$  = 1900), 442 ( $\epsilon$  = 1560), 455 (sh,  $\epsilon$  = 1363), 469 ( $\epsilon$  = 1125), 695 (sh,  $\epsilon$  = 1133), 798 ( $\epsilon$  = 1650), 875 ( $\epsilon$  = 1545). IR (KBr pellet): 3046(m), 3015(m), 2904(s), 2890(s), 2821(m), 2794(w), 2743(w), 2706(w), 1972(w), 1593(w), 1495(w), 1490(m), 1473(m), 1454(m), 1389(w), 1351(s), 1284(m), 1248(m), 1185(s), 1100(s), 1009(w), 996(s), 963(s), 837(m), 808(m), 787(m), 714(m), 617(w), 594(w), 531(w), 482(w).

#### 1.4.3 Synthesis of {[K(18-c-6)][ $\mu$ : $\eta^2$ -C<sub>10</sub>H<sub>8</sub>]} $_{\infty}$ , **3**.

The synthesis of **3** was performed using 0.103.8 g (0.810 mmol) of C<sub>10</sub>H<sub>8</sub> and 31.7 g (0.810 mmol) of potassium metal in 8 mL of THF to which 0.215 g (0.813 mmol) of 18-crown-6 was added. Yield: 0.280 g, 80%. Dark green crystals of **3** for X-ray crystallographic analysis were grown from a concentrated dark green THF solution stored at -25 °C. 2.11  $\mu$ B (Gouy measurement). UV-vis/NIR (THF, 0.114 mM, 25 °C, L $\cdot$ mol $^{-1}$   $\cdot$ cm $^{-1}$ ): 294 ( $\epsilon$  = 6190), 321 (sh,  $\epsilon$  = 2753), 326 ( $\epsilon$  = 4643), 374 ( $\epsilon$  = 1574), 408 (sh,  $\epsilon$  = 948), 445 ( $\epsilon$  = 787), 452 (sh,  $\epsilon$  = 715), 469 ( $\epsilon$  = 579), 688 (sh,  $\epsilon$  = 511), 771 ( $\epsilon$  = 811), 856 ( $\epsilon$  = 793). IR (KBr pellet): 3046(m), 3015(s), 2935(m), 2883(s), 2853(s), 2821(s), 2792(m), 2742(m), 2712(m), 2687(w), 2537(w), 2485(w), 2406(w), 2386(w), 2349(w), 2286(w), 2245(w), 2166(w), 2133(w), 1972(w), 1944(w), 1834(w), 1764(w), 1693(w), 1668(w), 1593(m), 1492(s), 1464(s), 1454(s), 1431(s), S7 1364(s), 1350(s), 1282(s), 1252(s), 1235(m), 1187(s), 1101(s), 1057(m), 997(s), 959(s), 838(s), 801(m), 786(m), 712(s), 594(m), 527(w), 464(m).

#### 1.4.4 Synthesis of [Li( $\kappa^3$ -18-c-6)(THF)<sub>2</sub>][C<sub>12</sub>H<sub>10</sub>], **4**.

The synthesis of **4** was performed using 0.300 g (1.945 mmol) of C<sub>12</sub>H<sub>10</sub> and 0.014 g (1.945 mmol) of lithium metal in 6 mL of THF to which 0.524 g (1.982 mmol) of 18-crown-6 was added. Yield: 0.352 g, 42%. Dark indigo crystals of **4** for X-ray crystallographic analysis were grown from a concentrated dark turquoise THF solution stored at -25 °C. 2.08  $\mu$ B (Gouy measurement). UV-vis/NIR (THF, 0.284 mM, 25 °C, L $\cdot$ mol $^{-1}$   $\cdot$ cm $^{-1}$ ): 411 ( $\epsilon$  = 12987), 451 (sh,  $\epsilon$  = 3433), 609 (sh,  $\epsilon$  = 5163), 643 ( $\epsilon$  = 5765), 748 (sh,  $\epsilon$  = 1971), 829 ( $\epsilon$  = 1135). IR (KBr pellet): 3039(s), 2912(s), 2871(s), 2721(w),

2621(w), 2584(w), 2520(w), 2407(w), 1849(w), 1729(w), 1654(w), 1567(s), 1367, 1461(m), 1460(s), 1451(m), 1372(m), 1326(m), 1323(s), 1295(w), 1292(w), 1288(m), 1277(m), 1243(m), 1161(s), 1110(s), 1069(s), 1051(s), 1029(m), 988(s), 987(s), 963(m), 935(m), 892(w), 891(w), 775(m), 729(w), 728(w), 687(w), 668(s), 568(w), 523(w), 421(w).

#### 1.4.5 Synthesis of [Na(18-c-6)(THF)<sub>2</sub>][C<sub>12</sub>H<sub>10</sub>], **5**.

The synthesis of **5** was performed using 0.222 g (1.439 mmol) of C<sub>12</sub>H<sub>10</sub> and 0.030 g (1.304 mmol) of sodium metal in 8 mL of THF to which 0.344 g (1.304 mmol) of 18-crown-6 was added. Yield: 0.413 g, 53%. Dark indigo crystals of **5** for X-ray crystallographic analysis were grown from a concentrated dark turquoise THF solution stored at -25 °C. 2.24 μB (Gouy measurement). UV-vis/NIR (THF, 0.284 mM, 25 °C, L•mol<sup>-1</sup> •cm<sup>-1</sup>): 410 (ε = 11579), 451 (ε = 5911), 610 (ε = 6420), 653 (ε = 3260), 747 (ε = 1611), 837 (ε = 589). IR (KBr pellet): 3031(w), 2989(w), 2898(s), 2823(w), 2749, 1930(w), 1561(s), 1480(m), 1430(m), 1351(s), 1321(m), 1284(m), 1251(s), 1158(s), 1104(s), 1004(w), 987(m), 963(s), 936(s), 838(s), 778(w), 741(m), 729(s), 699(m), 688(w), 663(w), 610(w), 530(w).

#### 1.4.6 Synthesis of [K(18-c-6)(THF)<sub>2</sub>][C<sub>12</sub>H<sub>10</sub>], **6**.

The synthesis of **6** was performed using 0.268 g (1.744 mmol) of C<sub>12</sub>H<sub>10</sub> and 0.068 g (1.744 mmol) of potassium metal in 5 mL of THF to which 0.460 g (1.740 mmol) of 18-crown-6 was added. Yield: 0.400 g, 38%. Dark indigo crystals of **6** for X-ray crystallographic analysis were grown from a concentrated dark turquoise THF solution stored at -25 °C. 2.20 μB (Gouy measurement). UV-vis/NIR (THF, 0.284 mM, 25 °C, L•mol<sup>-1</sup> •cm<sup>-1</sup>): 403 (ε = 13327), 435 (ε = 6961), 610 (ε = 5073), 649 (ε = 5641), 747 (ε = 1086), 831 (ε = 907). IR (KBr pellet): 3045(m), 2992(m), 2884(s), 2820(m), 2793(m), 2743(w), 2710(w), 2687(w), 2620(w), 2587(w), 2522(w), 2404(w), 2304(w), 2244(w), 2102(w), 2046(m), 1975(w), 1914(w), 1846(w), 1728(w), 1654(w), 1565(s), 1500(w), 1493(m), 1467(s), 1452(m), 1431(w), 1379(m), 1350(s), 1322(s), 1283(m), 1248(m), 1201(w), 1152(s), 1100(s), 1060(m), 1004(m), 987(s), 962(s), 936(s), 905(w), 838(m), 772(w), 742(w), 707(w), 688(w), 671(s), 549(w), 536(w), 530(w).

#### 1.4.7 Synthesis of [Li(18-c-6)][C<sub>14</sub>H<sub>10</sub>], **7**.

The synthesis of **7** was performed using 0.102 g (0.572 mmol) of C<sub>14</sub>H<sub>10</sub> and 0.003 g (0.432mmol) of lithium metal in 3 mL of THF to which 0.139 g (0.525 mmol) of 18-crown-6 was added. Yield: 0.070 g, 30%. Dark blue crystals of **7** for X-ray crystallographic analysis were grown from a concentrated dark blue DME solution layered with hexanes and stored at -25 °C. 1.67 μB (Gouy measurement). UV-vis/NIR (THF, 0.105 mM, 25 °C, L•mol<sup>-1</sup> •cm<sup>-1</sup>): 328 (ε = 21450), 340 (ε = 10142), 348 (ε = 10019), 358 (ε = 11087), 369 (ε = 18888), 378 (ε = 5705), 407 (ε = 2464), 478 (ε = 783), 513 (ε = 1046), 550 (ε = 1543), 585 (ε = 1892), 598 (ε = 2245), 641 (ε = 2542), 659 (ε = 3478), 696 (ε = 4726), 735 (ε = 5918), 759 (ε = 5752), 813 (ε = 1452), 843, (ε = 966), 921 (ε = 622), 956 (ε = 392). IR (KBr pellet): 3057(w), 3033(m), 3002(m), 2965(m), 2909(s), 2873(s), 2731(w), 2709(w), 2677(m), 2580(w), 2555(w), 2529(w), 2487(w), 2455(w), 2357(w), 2268(w), 2156(w), 2116(w), 2045(w), 1840(m), 1769(w), 1753 (m), 1697(w), 1648(m), 1560(m), 1512(s), 1463(s), 1450(s), 1378(s), 1364(m), 1320(s), 1293(s), 1280(s), 1264(s), 1243(m), 1189(w), 1170(s), 1153(s), 1113(s), 1068(s), 1049(s), 1021(s), 963(w), 932(s), 897(w), 883(m), 836(w), 823(w), 799(s), 772(s), 726(w), 701(m), 692(s), 620(w), 590(w), 588(w), 569(w), 518(m), 460(s), 421(w).

#### 1.4.8 Synthesis of [Na(18-c-6)(DME)][C<sub>14</sub>H<sub>10</sub>], **8**.

The synthesis of **8** was performed using 0.246 g (1.380 mmol) of C<sub>14</sub>H<sub>10</sub> and 0.034 g (1.478mmol) of sodium metal in 8 mL of DME to which 0.400 g (1.513 mmol) of 18-crown-6 was added. Yield: 0.673 g, 87%. Dark blue crystals of **8** for X-ray crystallographic analyses were grown from a concentrated dark blue DME solution stored at -25 °C. 1.90 μB (Gouy measurement). UV-vis/NIR (THF, 0.115 mM, 25 °C, L•mol<sup>-1</sup> •cm<sup>-1</sup>): 328 (ε = 26757), 349 (ε = 12184), 363 (ε = 11631), 368 (ε = 23879), 378 (sh, ε = 4411), 406 (sh, ε = 2749), 475 (ε = 875), 512 (ε = 1274), 539 (sh, ε = 1835), 553 (ε = 2054), 588 (ε = 2589), 599 (ε = 2927), 642 (sh ε = 3412), 663 (ε = 4519), 699 (ε = 6340), 734 (ε = 8185), 761 (ε = 7764), 819 (ε = 1871), 837 (ε = 1360), 934 (ε = 739). IR (KBr pellet): 3039(w), 3033(w), 3005(w), 2893(s), 2867(s), 2740(w), 2675(w), 1831(w), 1784(w), 1748(w), 1636(w), 1620(w), 1561(w), 1534(w), 1512(m), 1452(m), 1449(m), 1379(s), 1375(m), 1320(s), 1288(m),

1249(m), 1169(m), 1101(s), 1019(m), 997(w), 963(s), 883(s), 836(m), 798(m), 738(m), 744(m), 726(s), 699(m), 602(w), 531(w), 474(m), 461(w).

#### 1.4.9 Synthesis of [K(18-c-6)(THF)<sub>2</sub>][C<sub>14</sub>H<sub>10</sub>], **9**.

The synthesis of **9** was performed using 0.115 g (0.645 mmol) of C<sub>14</sub>H<sub>10</sub> and 0.025 g (0.639 mmol) of potassium metal in 8 mL of DME to which 0.148 g (0.559 mmol) of 18-crown-6 was added. Yield: 0.225 g, 64%. Dark blue crystals of **9** for X-ray crystallographic analyses were grown from a concentrated dark blue THF solution stored at -25 °C. 1.97 μB (Gouy measurement). UV-vis/NIR (THF, 0.116 mM, 25 °C, L•mol<sup>-1</sup> •cm<sup>-1</sup>): 328 (ε = 30268), 340 (sh, ε = 14422), 348 (ε = 14570), 358 (ε = 13896), 367 (ε = 27078), 378 (sh, ε = 510 5275), 407 (ε = 3746), 478 (sh, ε = 1003), 513 (sh, ε = 1496), 550 (ε = 2489), 585 (sh, ε = 2651), 598 (ε = 3600), 640 (ε = 3953), 661 (ε = 5661), 698 (ε = 7691), 733 (ε = 9709), 759 (ε = 8589), 813 (ε = 2098), 843 (sh, ε = 1442), 925 (ε = 919), 956 (sh, ε = 521). IR (KBr pellet): 3501(w), 3013(m), 2916(m), 2883(s), 2879(s), 2822(m), 2810(m), 2741(m), 2689(m), 2678(m), 1837(w), 1790(w), 1744(m), 1562(m), 1523, 1514(s), 1469(s), 1450(s), 1430(m), 1383(s), 1375(s), 1320(s), 1282(s), 1245(s), 1241(s), 1179(w), 1170(s), 1127(s), 1099(s), 1059(s), 1020(s), 962(s), 849(s), 803(s), 800(s), 774(s), 738(s), 709(s), 702(s), 602(w), 529(w), 470(s).

#### 1.4.10 Synthesis of [Li(κ<sup>3</sup>-18-c-6)(DME)][C<sub>20</sub>H<sub>12</sub>]•0.5C<sub>20</sub>H<sub>12</sub>, **10**.

The synthesis of **10** was performed using 0.224 g (0.887 mmol) of C<sub>20</sub>H<sub>12</sub> and 0.006 g (0.864 mmol) of lithium metal in 8 mL of THF to which 0.250 g (0.945 mmol) of 18-crown-6 was added. Yield: 0.361 g, 55%. Dark purple crystals of **10** for X-ray crystallographic analyses were grown from a concentrated dark blue-purple DME solution stored at -25 °C. 2.20 μB (Gouy measurement). UV-vis/NIR (THF, 0.036 mM, 25 °C, L•mol<sup>-1</sup> •cm<sup>-1</sup>): 322 (ε = 13169), 376 (sh, ε = 3502), 392 (ε = 6108), 411 (ε = 12220), 437 (ε = - 16010), 536 (sh, ε = 7123), 579 (ε = 40270), 688 (ε = 3809), 740 (ε = 3308), 761 (ε = 3342), 782 (ε = 3105), 813 (ε = 2782), 847 (ε = 2653), 882 (sh, ε = 2215), 903 (ε = 2466), 1007 (ε = 1088). IR (KBr pellet): 3064(w), 3049(m), 2903(s), 2871(s), 1591(w), 1563(w), 1535(s), 1480(w), 1468(m), 1455(m), 1405(w), 1380(m), 1364(m), 1352(m), 1310(s), 1280(s), 1250(m), 1215(w), 1185(w), 1108(s), 1071(s), 1051(m), 1019(m), 964(m), 931(w), 898(w), 837(w), 811(s), 788(m), 766(s), 748(s), 585(w), 568(w), 541(w), 529(w), 465(w), 458(w).

#### 1.4.11 Synthesis of [Na(18-c-6)(DME)][C<sub>20</sub>H<sub>12</sub>], **11**.

The synthesis of **11** was performed using 0.114 g (0.564 mmol) of C<sub>20</sub>H<sub>12</sub> and 0.017 g (0.739 mmol) of sodium metal in 8 mL of DME to which 0.198 g (0.564 mmol) of 18-crown-6 was added. Yield: 0.300 g, 84%. Dark purple crystals of **11** for X-ray crystallographic analyses were grown from a concentrated dark blue-purple DME solution stored at -25 °C. 2.29 μB (Gouy measurement). UV-vis/NIR (THF, 0.052 mM, 25 °C, L•mol<sup>-1</sup> •cm<sup>-1</sup>): 323 (ε = 11424), 375 (sh, ε = 3734), 393 (ε = 5298), 414 (ε = 8664), 438 (ε = 13276), 465 (ε = 8595), 535 (sh, ε = 7418), 580 (ε = 33319), 692 (ε = 5764), 737 (ε = 4688), 761 (sh, ε = 4503), 782 (ε = 2669), 813 (ε = 2512), 849 (ε = 2193), 882 (sh, ε = 2119), 906 (ε = 2410), 1010 (ε = 1103). IR (KBr pellet): 3085(w), 3048(m), 3032(m), 2894(s), 2872(s), 1969(w), 1923(w), 1863(w), 1564(m), 1548(m), 1534(s), 1494(w), 1469(m), 1405(w), 1392(w), 1380(w), 1350(s), 1330(m), 1312(s), 1280(s), 1250(s), 1215(w), 1203(w), 1184(w), 1125(s), 1103(s), 1019(s), 962(s), 949(s), 862(w), 840(m), 811, 788(m), 767(s), 749(s), 541(w), 529(w), 487(w), 457(w).

#### 1.4.12 Synthesis of [K(18-c-6)(THF)<sub>2</sub>][C<sub>20</sub>H<sub>12</sub>], **12**.

The synthesis of **12** was performed using 0.488 g (2.415 mmol) of C<sub>20</sub>H<sub>12</sub> and 0.071 g (1.815 mmol) of potassium metal in 8 mL of DME to which 0.486 g (1.838 mmol) of 18-crown-6 was added. Yield: 0.480 g, 38%. Dark purple crystals of **12** for X-ray crystallographic analyses were grown from a concentrated dark blue-purple THF solution stored at -25 °C. 2.10 μB (Gouy measurement). UV-vis/NIR (THF, 0.056 mM, 25 °C, L•mol<sup>-1</sup> •cm<sup>-1</sup>): 323 (ε = 18863), 371 (sh, ε = 3845), 393 (ε = 5272), 413 (ε = 8311), 438 (ε = 10908), 468 (sh, ε = 1733), 532 (sh, ε = 10780), 580 (ε = 58459), 689 (ε = 6518), 741 (ε = 6111), 757 (ε = 6257), 778 (ε = 5957), 812 (ε = 4993), 847 (ε = 4966), 885 (sh, ε = 4385), 903 (ε = 4474), 1008 (ε = 2291). IR (KBr pellet): 3501(w), 3085(w), 3031(m), 2881(s), 2825(s), 2745(s), 1971(w), 1871(w), 1688(w), 1638(w), 1620(w), 1564(s), 1548(s), 1536(s), 1466(s), 1450(m), 1431(w), 1406(w), 1392(w), 1365(w), 1350(s), 1331(s), 1311(s), 1283(s), 1262(s), 1253(s), 1205(w), 1133(s), 1105(s), 1020(s), 992(w), 961(s), 839(s), 811(w), 802(m), 788(s), 752(s), 568(w), 532(w), 526(w), 489(w), 455(m).

**Table 1.1** Isolated arene radical monoanions and electronic properties

Compound	% Yield	$E_{1/2}^a$ (V)	$\lambda$ (nm)	$\mu_{\text{eff}}^b$ ( $\mu_B$ )
[Li(18-c-6)][C <sub>10</sub> H <sub>8</sub> ] (1)	37	−3.09	294, 318, 327, 376, 435, 468, 799	1.53
[Na(18-c-6)(DME)][C <sub>10</sub> H <sub>8</sub> ] (2)	79	−3.09	294, 327, 373, 442, 469, 798, 875	1.67
{[K(18-c-6)][μ:η <sup>2</sup> -C <sub>10</sub> H <sub>8</sub> ]} <sub>∞</sub> (3)	80	−3.13	294, 326, 374, 445, 469, 771, 856	2.11
[Li(κ <sup>3</sup> -18-c-6)(THF) <sub>2</sub> ][C <sub>12</sub> H <sub>10</sub> ] (4)	42	−3.18	411, 643, 829	2.08
[Na(18-c-6)(THF) <sub>2</sub> ][C <sub>12</sub> H <sub>10</sub> ] (5)	53	−3.15	410, 451, 653, 837	2.24
[K(18-c-6)(THF) <sub>2</sub> ][C <sub>12</sub> H <sub>10</sub> ] (6)	37	−3.17	403, 649, 831	2.20
[Li(18-c-6)][C <sub>14</sub> H <sub>10</sub> ] (7)	30	−2.53	328, 348, 358, 369, 407, 550, 598, 641, 659, 696, 735, 759, 813, 921	1.67
[Na(18-c-6)(DME)][C <sub>14</sub> H <sub>10</sub> ] (8)	87	−2.48	329, 342, 353, 359, 368, 379, 407, 546, 595, 638, 659, 698, 728, 752, 813, 922	1.90
[K(18-c-6)(THF) <sub>2</sub> ][C <sub>14</sub> H <sub>10</sub> ] (9)	31	−2.49	328, 348, 358, 367, 407, 550, 598, 640, 661, 698, 733, 759, 813, 925	1.97
[Li(κ <sup>3</sup> -18-c-6)(DME)][C <sub>20</sub> H <sub>12</sub> ]·0.5C <sub>20</sub> H <sub>12</sub> (10)	55	−2.20, −2.87	322, 388, 411, 437, 579, 688, 740, 761, 782, 813, 847, 903, 1007	2.20
[Na(18-c-6)(DME)][C <sub>20</sub> H <sub>12</sub> ] (11)	84	−2.19, −2.77	323, 393, 414, 438, 465, 580, 692, 737, 782, 813, 849, 906, 1010	2.29
[K(18-c-6)(THF) <sub>2</sub> ][C <sub>20</sub> H <sub>12</sub> ] (12)	38	−2.28, −2.80	323, 393, 413, 438, 580, 689, 741, 757, 778, 812, 847, 903, 1008	2.10

<sup>a</sup> Referenced vs. Fe<sup>0/+</sup>. <sup>b</sup> Guoy balance measurement.

## 1.5 RESULTS AND DISCUSSION

### 1.5.1 Isolation and magnetic susceptibility

Even though 18-crown-6 is a known polyether for chelating  $K^+$ , we demonstrated that this relative common and inexpensive reagent is also suitable for use in concert with  $Li^+$  and  $Na^+$ , allowing the isolation of the respective alkali arenides. The number of coordinated molecules to the alkali metal cannot be quantified by NMR spectroscopy due to the paramagnetic nature of these radicals, giving rise

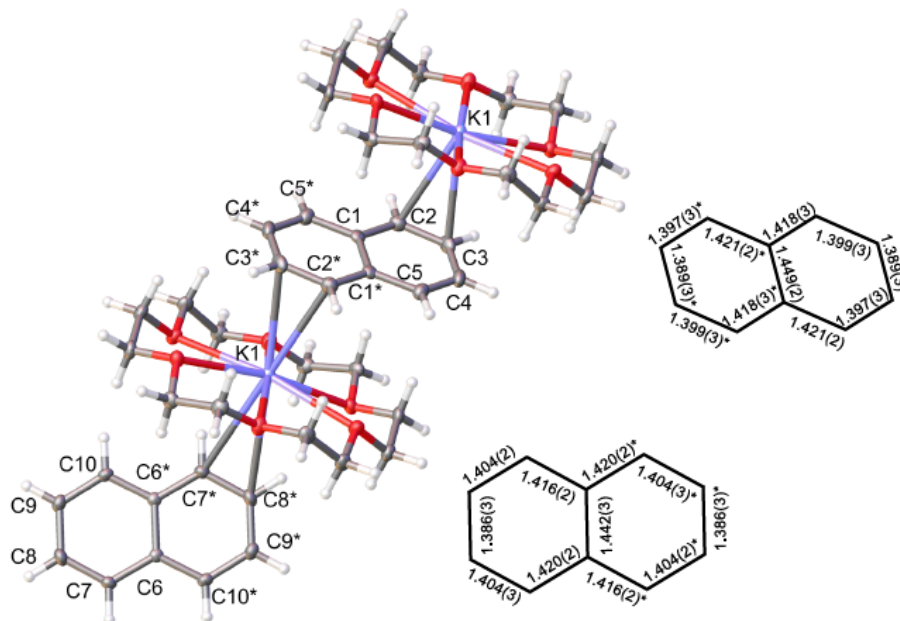


**Figure 1.1** Solid-state molecular structure of **3** with 50% probability ellipsoids and respective bond length (Å) diagram. Asterisks denote symmetry generated atoms and bond lengths.

to significant signal broadening. Luckily, the high crystallinity of these molecules allows us to unambiguously characterize them by X-ray diffractometry. Harvested crystals from THF were suitable for XRD analyses in most of the cases. However, when dealing with lithium and sodium salts of naphthalene and perylene, very fine needles were obtained, unsuitable for x-ray diffraction. In such cases, recrystallization of the isolated needles from DME solutions yields X-ray quality crystals.



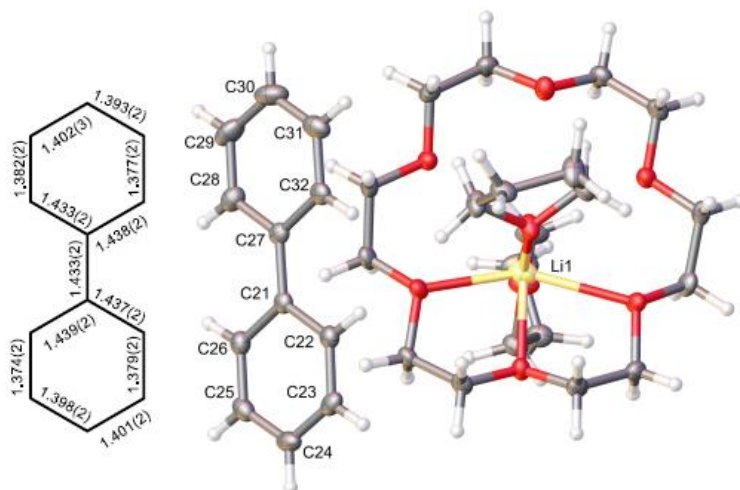


**Figure 1.2** Solid-state molecular structure of **4** with 50% probability ellipsoids and respective bond length (Å) diagram.

Solid-state, room temperature magnetic susceptibility of the crystalline open-shell compounds **1-12** was measured in a Gouy Balance under strict anaerobic conditions. The effective magnetic moments of our complexes were found between 1.53 to 2.28  $\mu_B$  (Table 1.1). These values fall in the range of 1.7  $\mu_B$ , calculated for an isolated  $S = \frac{1}{2}$  system and are comparable to that found in  $[K_2(THF)][C_{10}H_8]$  (1.69  $\mu_B$  per anion).<sup>7</sup>

### 1.5.2 Solid-state X-ray Structure

Examination of the crystal structures of **1-12** shows that all ionic pairs are non-interacting in the solid state with one notable exception,  $\{[K(18-c-6)][\mu:\eta^2-C_{10}H_8]\}_\infty$  (**3**) (appendix Figure S1-S8). In Figure 1.1, each  $K(18-c-6)^+$  is approached by two  $C_{10}H_8^{\bullet-}$  units with different binding mode forming a polymeric 1D ionic network. One of the  $C_{10}H_8^{\bullet-}$  coordinates to potassium in a  $\eta^2$ -binding mode giving evidence of a  $\pi$ -cationic interaction (K-C bond avg. 3.13 Å, dihedral angle. 120.3°), whereas the other  $C_{10}H_8^{\bullet-}$  moiety engages with potassium through longer bonds consistent with agostic interactions between the C-H bonds in naphthalene and potassium (K-C bond avg. 3.45 Å, dihedral angle. 150.3°).<sup>22</sup> It is to be noted that the previously reported  $[K(18-c-6)(THF)_2][C_{10}H_8]$  exists as a separated ion pair.<sup>4</sup> We attribute this structural variation to the different crystallization methods and conditions used for the isolation of compounds **1-12** vs. that for  $[K(18-c-6)(THF)_2][C_{10}H_8]$ .

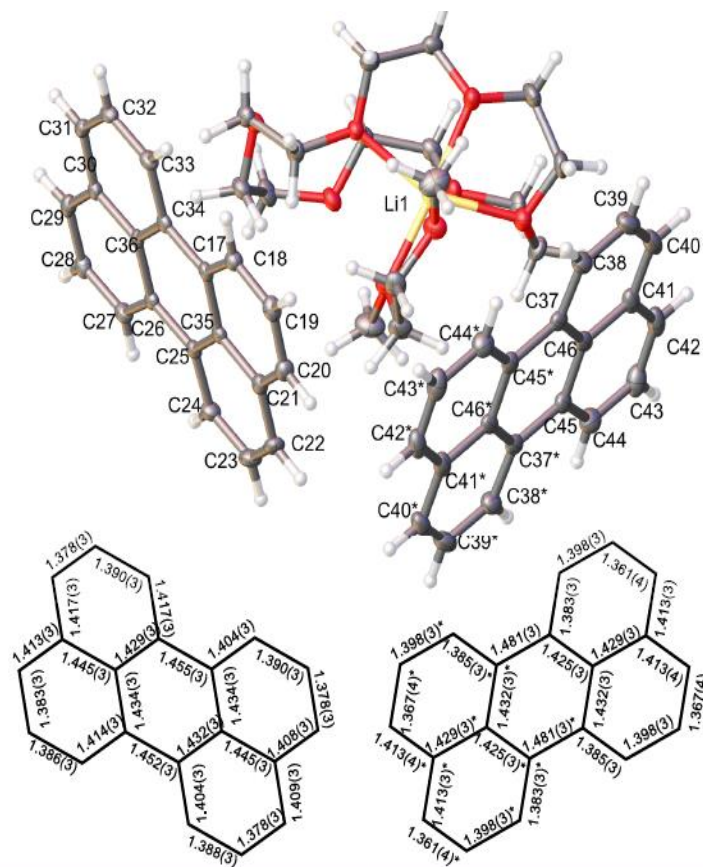


**Figure 1.3** Solid-state molecular structure of **10** with 50% probability ellipsoids and respective bond length (Å) diagram. Asterisks denote symmetry generated atoms and bond lengths.

With the exception of a few structures, chelation mode of the crown ether involves a  $\kappa^6$ -interaction, independent of the size of the alkali metal. In **4**, with the aid of two molecules of THF, a  $\kappa^3$ -interaction between 18-crown-6 and lithium is observed (Figure 1.2). Comparatively in **10**, a  $\kappa^3$ -interaction of lithium with the crown ether is accompanied with a  $\kappa^2$  interaction with a molecule of DME (Figure 1.3). All of the potassium salts, with the exception of **3**, involve an equatorial  $\kappa^6$  interaction with the crown ether and two axial THF molecules in the coordination sphere of the metal. The sodium salts' chelation always shows a  $\kappa^2$  interaction with a molecule of DME, with **5** being the exception showing the same coordination sphere as the potassium analog. (Figure 1.4)

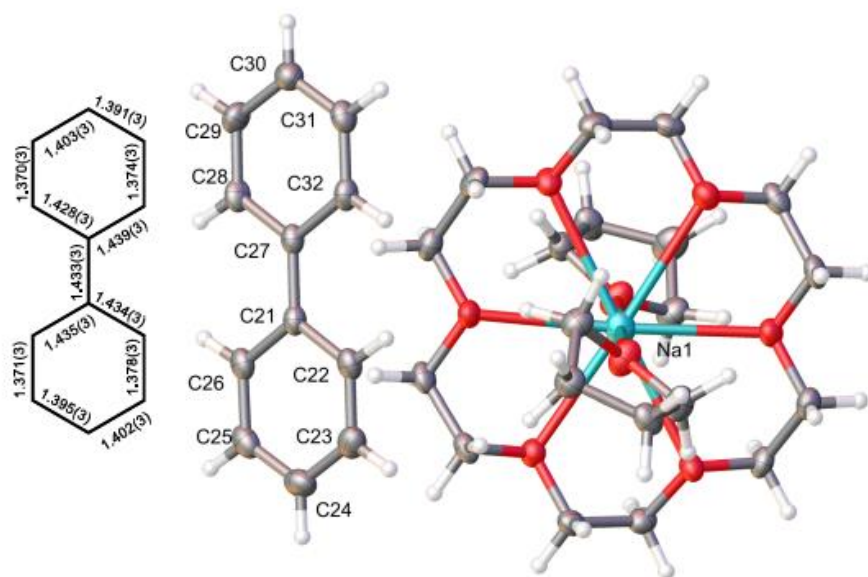


**Figure 1.4** Solid-state molecular structure of **5** with 50% probability ellipsoids and respective bond length (Å) diagram.

### 1.5.3 Electrochemistry

By having the additional component of 18-crown-6 in our reductant composition, we demonstrate that the reductive properties of our twelve arenides was not affected. This was done by performing cyclic voltammetry studies on each of our complexes. In all cases, chemically reversible redox waves ( $i_{pc}/i_{pa} \approx 1$ ) are observed, all in agreement with the known  $E_{1/2}$  values and reduction potentials (Appendix Figures S16-S26 and Tables S1-S12).<sup>4,15</sup> It has been suggested that the identity of the alkali metal in the reductant salt should have a detectable effect in the potential values.<sup>15</sup> However, we do not see any effects on changing between Li, Na, or K in the same arene under our conditions (Appendix Figure S12-15). As expected, the reducing trend of our alkali arenides follows  $C_{20}H_{12}^{\bullet-} < C_{14}H_{10}^{\bullet-} < C_{10}H_8^{\bullet-} < C_{12}H_{10}^{\bullet-}$  (Table 1.1). At last, considering that our arenides may have chemically accessible dianionic forms, we saw only perylene in **10-12** displayed a second redox event in the CV under our conditions (Figure 1.5).

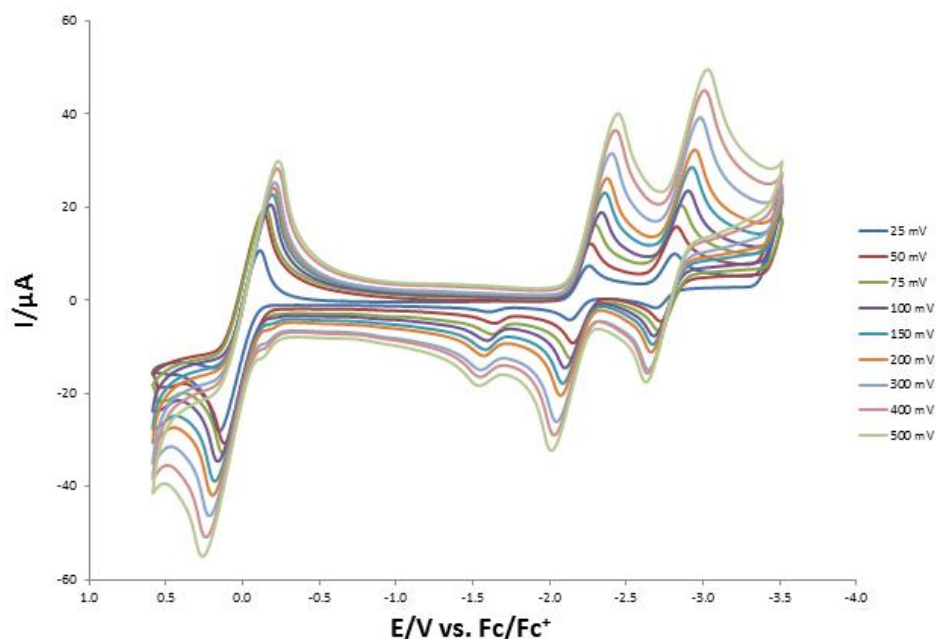


**Figure 1.5** Room temperature cyclic voltammogram of **12** in DME

#### 1.5.4 UV-vis/NIR absorption spectroscopy

Because each of the four classes of radical anions are known to have specific electronic absorption features,<sup>4,23</sup> UV-vis/NIR absorption spectroscopy was performed on **1-12** (Table 1.1). We found that, within the same arene class, the spectra are qualitatively the same; however, the features observed in the spectra appear to be cation dependent with no systematic trend (Figure 1.6 and Appendix Figures S9-S11). To the best of our knowledge, there is no other reported example regarding the cation-dependent spectra among these arenes. These observations are contrary to their respective CV data, in which they show no cation dependence. However, we attribute this to the excess amount of supporting electrolyte in our electrochemical cells, which may interfere with the pairing effects between arenides and cations.

### 1.6 CONCLUSION

We have developed a straight-forward synthesis and isolation procedure of highly crystalline well-defined alkali arenide reductants **1-12**. We demonstrated that 18-crown-6 is a suitable crown ether to stabilize the coordination sphere of alkali cations upon solvent removal and that the described reductants are easily isolated from concentrated solutions of THF or DME. These reductants offer a

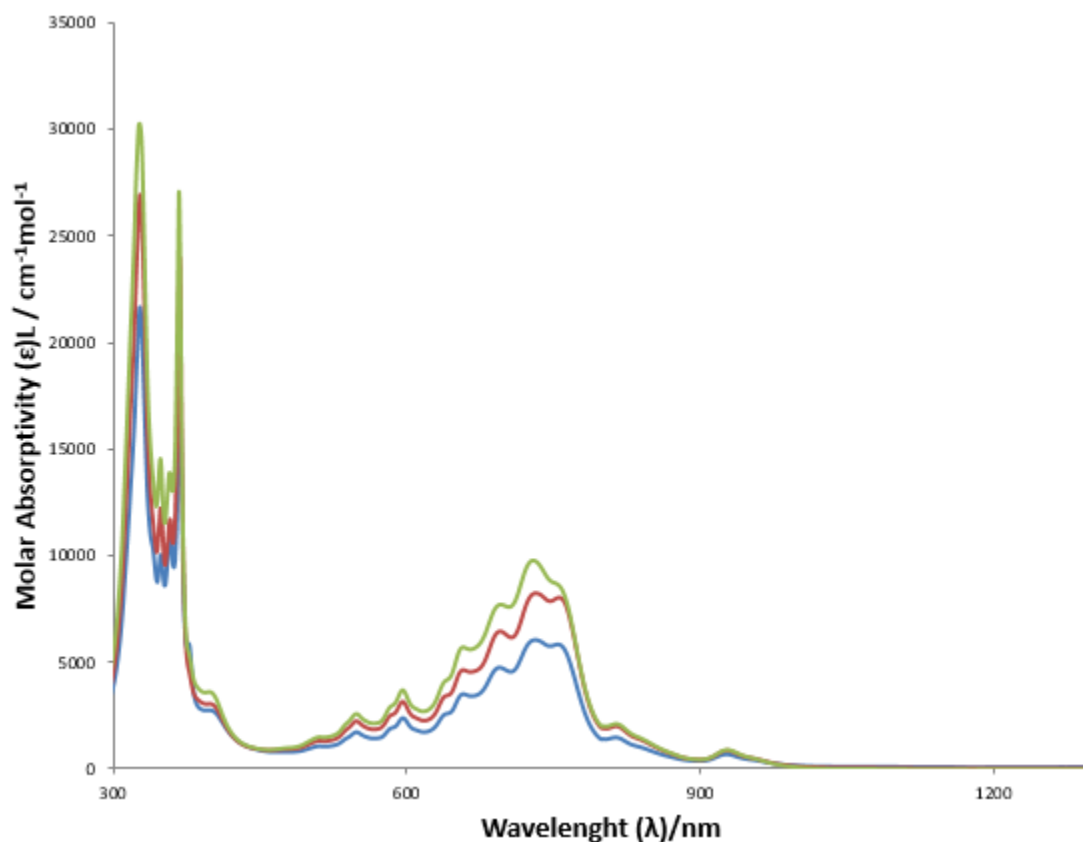


**Figure 1.6** Room temperature UV/vis-NIR absorption spectra for **7** (THF, 0.105 mM), **8** (THF, 0.115 mM), and **9** (THF, 0.116 mM).

specific molecular weight, being gravimetrically quantifiable reducing agents with a wide potential range (-2.2 to -3.2 V vs.  $\text{Fc}^{0/+}$ ). Moreover, we have found these very reactive species to be stable at -30 °C under dinitrogen atmosphere for an indefinite amount of time (at least 2 years) as opposed to the reductant solutions used for the past century.

## REFERENCES

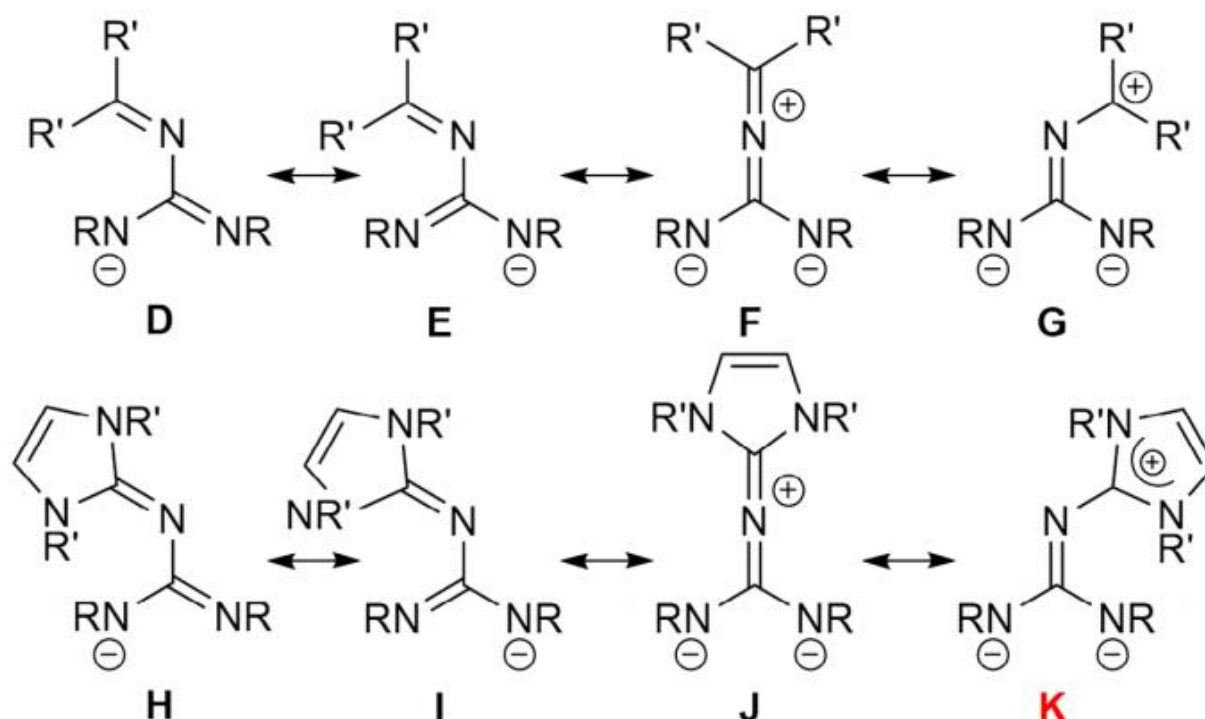
- (1) M. Castillo, A. J. Metta-Magana and S. Fortier, *New J. Chem.*, **2016**, 40, 1923
- (2) W. Schlenk, J. Appenrodt, A. Michael and A. Thal, *Ber. Dtsch. Chem. Ges.*, **1914**, 47, 473–490.
- (3) N. D. Scott, J. F. Walker and V. L. Hansley, *J. Am. Chem. Soc.*, **1936**, 58, 2442–2444.
- (4) N. L. Holy, *Chem. Rev.*, **1974**, 74, 243–277.
- (5) A. Soncini and P. W. Fowler, *Chem. Phys. Lett.*, **2008**, 450, 431–436.
- (6) S. V. Rosokha and J. K. Kochi, *J. Org. Chem.*, **2006**, 71, 9357–9365.
- (7) T. A. Scott, B. A. Ooro, D. J. Collins, M. Shatruk, A. Yakovenko, K. R. Dunbar and H. C. Zhou, *Chem. Commun.*, **2009**, 65–67.
- (8) H. Bock, K. Gharagozloo-Hubmann, M. Sievert, T. Prisner and Z. Havlas, *Nature*, **2000**, 404, 267–269.
- (9) C. Melero, A. Guijarro and M. Yus, *Dalton Trans.*, **2009**, 1286–1289.
- (10) E. de Boer, A. A. K. Klaassen, J. J. Mooij and J. H. Noordik, *Pure Appl. Chem.*, **1979**, 51, 73.
- (11) D. Baskaran and A. H. E. Müller, in *Controlled and Living Polymerizations*, Wiley-VCH Verlag GmbH & Co. KGaA, **2010**, pp. 1–56.
- (12) M. Kowalczyk, P. Kurcok, W. Glowkowski and Z. Jedlinski, *J. Org. Chem.*, **1992**, 57, 389–391.
- (13) A. V. Zabula, A. S. Filatov, S. N. Spisak, A. Y. Rogachev and M. A. Petrukhina, *Science*, **2011**, 333, 1008–1011.
- (14) S. Kriek, R. Kretschmer, H. Gorls and M. Westerhausen, *J. Am. Chem. Soc.*, **2011**, 133, 6960–6963.
- (15) N. G. Connelly and W. E. Geiger, *Chem. Rev.*, **1996**, 96, 877–910.
- (16) A. Rainis and M. Szwarc, *J. Am. Chem. Soc.*, **1974**, 96, 3008–3010.
- (17) E. Grovenstein, in *Inorganic Reactions and Methods*, John Wiley & Sons, Inc., **2007**, pp. 160–164.
- (18) P. B. Hitchcock, M. F. Lappert and A. V. Protchenko, *J. Am. Chem. Soc.*, **2001**, 123, 189–190.
- (19) C. Näther, H. Bock, Z. Havlas and T. Hauck, *Organometallics*, **1998**, 17, 4707–4715.

- (20) H. Bock, C. Nather, Z. Havlas, A. John and C. Arad, *Ang. Chem. Int. Ed.*, **1994**, 33, 875–878.
- (21) H. Bock, C. Arad, C. Nather and Z. Havlas, *J. Chem. Soc., Chem. Commun.*, **1995**, 2393–2394.
- (22) C. Loh, S. Seupel, H. Görls, S. Krieck and M. Westerhausen, *Organometallics*, **2014**, 33, 1480–1491.
- (23) P. Balk, G. J. Hoijtink and J. W. H. Schreurs, *Recl. Trav. Chim.*, **1957**, 76, 813–823.
- (24) J.A. Soderquist, I. Rivera. *Tetrahedron Lett*, **1988**, 29, 3195.
- (25) SMART Apex II. Bruker AXS Inc., Madison, WI (**2005**).
- (26) O.V. Dolomanov, L.J. Bourhis, R.J. Gildea, J.A.K. Howard, H. Puschmann. *J. Appl. Crystallogr.*, **2009**, 42, 339.

## Chapter 2: Synthesis of a strong electron-donating guanidinate containing an imidazolin-2-iminato backbone and its properties on iron.<sup>1</sup>

### 2.1 INTRODUCTION

In our laboratory, we are interested in tuning the electron donating properties of guanidines, a very popular kind of ligand due to their unique resonance behavior.<sup>28, 29</sup> We have recently described our efforts to augment the electron donating ability of a guanidinate by incorporating a ketimine ( $R_2C=N^-$ ) backbone, considering that these functional groups can display both  $\sigma$ - and  $\pi$ -donation through the imine



**Scheme 2.1** Possible resonance structures of ketimine and  $Im^R N$  functionalized guanidines, D–G, and H–K, respectively.

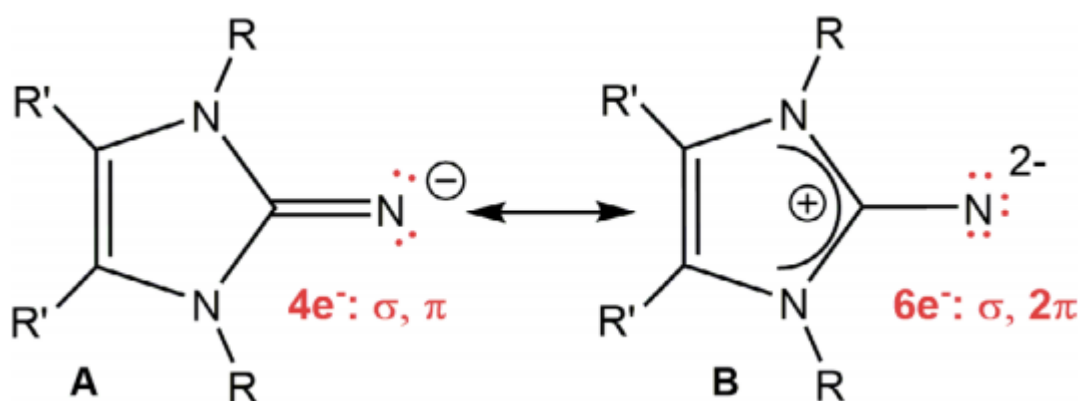
nitrogen. One can access very electron rich polarized resonance forms through conjugation because of the favoring iminium-diamido or carbonium-diamido ylidic forms (scheme 2.1, F and G, respectively),

<sup>1</sup> This chapter previously appeared as an article in the Journal of Coordination Chemistry. The original citation is as follows: Castillo, M.; Barreda, O.; Maity, A.; Barraza, B.; Lu, J.; Metta-Magana, A. J.; Fortier, S.; Advances in guanidine ligand design: synthesis of a strongly electron-donating, imidazolin-2-iminato functionalized guanidinate and its properties on iron. J. Coord. Chem., **2016**, DOI:10.1080/00958972.2016.1167198



potentially increasing the relative electron-richness of the coordinating guanidinate N-atoms.<sup>5, 6</sup> Even though these ketimine-guanidinate ligands show interesting steric, structure and reactivity features when chelated to iron, there was almost no electronic benefit attributed to the ketimine backbone. Since then we have directed our attention towards examining the chemistry of guanidines with imidazolin-2-iminato backbones, used in place of a ketimine, in an attempt to deeply understand the donor properties of imidazolin-2-imines.

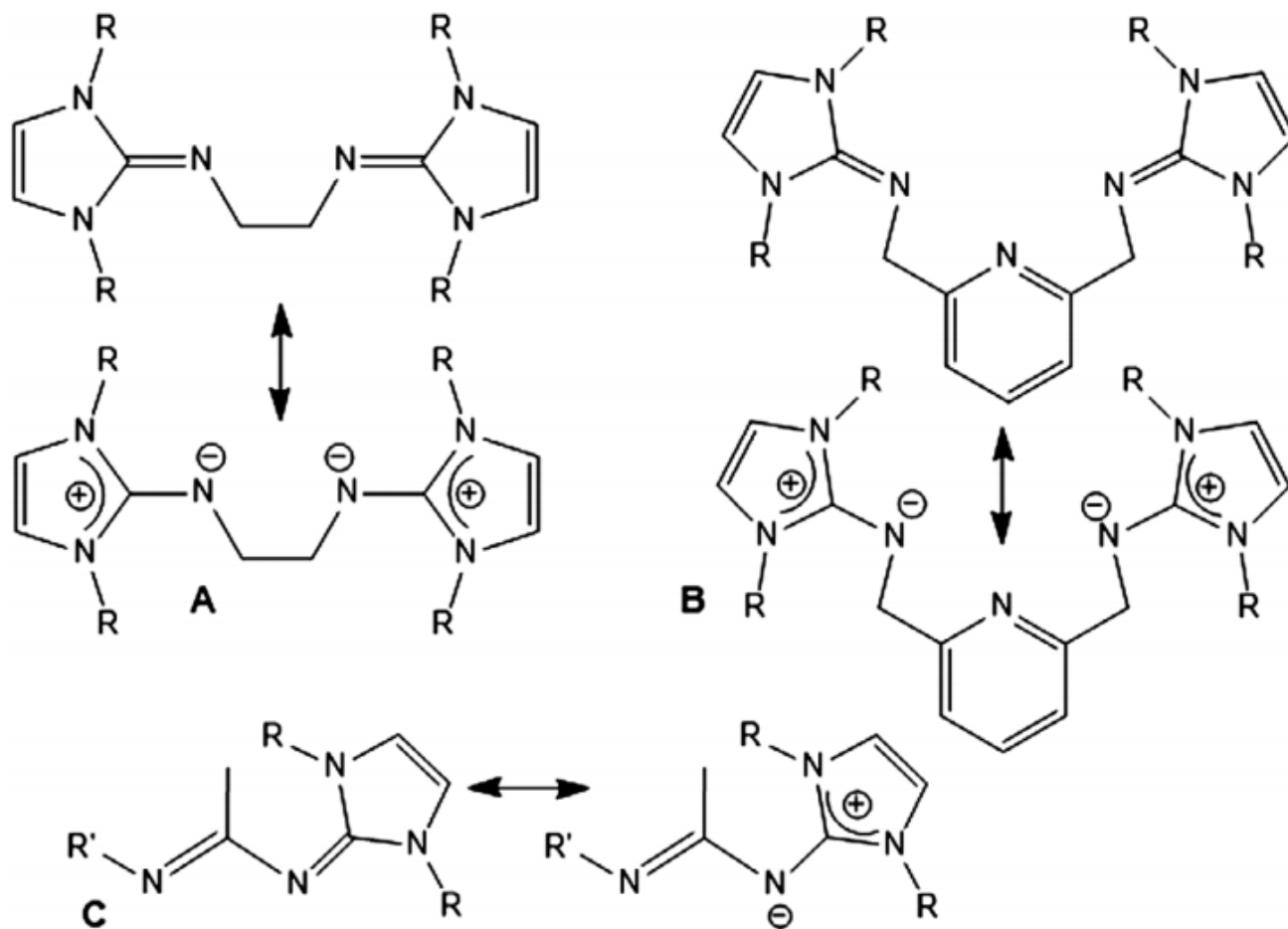
The imidazolin-2-iminato ( $\text{Im}^{\text{R}}\text{N}^-$ ) ligand class popularity, largely pioneered by Tamm,<sup>2-13</sup> has increased substantially over recent years due to the high modularity of NHCs precursors while exhibiting unique electronic features.<sup>2, 14, 15</sup> These kind of ligands can be easily synthesized by treating N-heterocyclic carbenes (NHCs) with  $\text{Me}_3\text{SiN}_3$  to afford silylimines that, upon desilylation with  $\text{MeOH}$ , give imidazolin-2-imines ( $\text{Im}^{\text{R}}\text{NH}$ ), containing themselves a guanidine type motif.<sup>2</sup> Even though the exocyclic nitrogen of these imidazolin-2-imines is known to be highly basic,<sup>2, 16</sup> it can be easily deprotonated using strong alkyl lithium bases like  $\text{MeLi}$  to give the monoanionic imidazolin-2-iminato lithium salts, synthons for the ligands  $\text{Im}^{\text{R}}\text{N}^-$ .<sup>40</sup> These anions are impressive electron donors as their NHC core allows the stabilization of an ylidic positive charge in the guanidine carbon while the exocyclic nitrogen adopts imido-like character (Scheme 2.2, B).<sup>2, 6, 9-12, 14, 15</sup> Impressively, X-ray structural analyses have shown through bond metric analyses that in this resonating form, the nitrogen can contribute to a total of 2  $\sigma$ - and 4  $\pi$ - electrons both in presence and absence of coordinated metals, being isoelectronic with the well-studied and vastly used cyclopentadienyl anion.<sup>2, 7, 9-11</sup> These features have been exploited to enhance the electron-donating abilities and basicity of common neutral ligand types featuring  $\text{Im}^{\text{R}}\text{N}$  in the scaffold including bidentate 1,4-diazabutadienes, NNN pincers, and others



**Scheme 2.2** Resonance forms of the  $\text{Im}^{\text{R}}\text{N}^-$  ligand.

(scheme 2.3).<sup>16, 18–27</sup>

As would be anticipated for a ketimine (scheme 2.1, top), when incorporated into a guanidinate system, the  $\text{Im}^{\text{R}}\text{N}^-$  group allows us to access four different resonances (scheme 2.1, **H–K**) in which the zwitterionic **K** should be favored owing to the readily accessible form **B** of the  $\text{Im}^{\text{R}}\text{N}^-$  group (Scheme 2.2). Herein, we describe the synthesis and characterization of  $\text{Im}^{\text{tBu}}\text{N}$ -guanidine  $[(\text{Im}^{\text{tBu}}\text{N}) \text{C}(\text{N}^{\text{dipp}})_2]^-$  (dipp = 2,6-diisopropylphenyl) system, the first guanidinate incorporating a very sterically hindered and electron rich  $\text{Im}^{\text{tBu}}\text{N}^-$  moiety as a backbone. The structural features of this ligand and X-ray crystallography analyses were performed when coordinated to lithium and iron and the details are fully discussed. To evaluate the relative electron-donating properties, its electronic effects on iron have been



**Scheme 2.3** Examples of neutral ligands incorporating the  $\text{Im}^{\text{R}}\text{N}^-$  functionality and their limiting resonance forms.

examined by UV–vis spectroscopy and cyclic voltammetry, the results of which are compared to closely related guanidinate and ketimine-guanidinate systems of iron previously reported by our group.<sup>29</sup>

## 2.2 EXPERIMENTAL CONSIDERATIONS

All air- and moisture-sensitive operations were performed in a M. Braun drybox under an atmosphere of purified nitrogen or using high-vacuum standard Schlenk techniques. Diethyl ether, hexanes, toluene, and THF were dried using a Pure Process Technology Solvent Purification System and subsequently stored under a dinitrogen atmosphere over activated 4 Å molecular sieves. All deuterated solvents were purchased from Cambridge Isotope Laboratories Inc, degassed by three freeze–pump–thaw cycles, and dried over activated 4 Å molecular sieves for 24 h prior to use. Celite and 4 Å molecular sieves were heated to 150 °C for at least 24 h and then cooled under vacuum. KH was activated<sup>31</sup> and (dippN)<sub>2</sub>C<sup>32</sup> and [Li(Et<sub>2</sub>O)][Im<sup>tBu</sup>N]<sup>17</sup> were prepared following literature procedures; all other reagents were purchased from commercial suppliers and used as received. NMR spectra were recorded on a JEOL ECA 600 MHz or a Bruker AVANCE III 400 MHz. <sup>1</sup>H and <sup>13</sup>C NMR spectra are referenced to SiMe<sub>4</sub> using the residual <sup>1</sup>H solvent peaks as internal standards or the characteristic <sup>13</sup>C resonances of the solvent. <sup>7</sup>Li{<sup>1</sup>H} spectrum for **13** (Appendix Figure S40) was referenced to external LiCl in D<sub>2</sub>O. Resonance assignments in the <sup>13</sup>C NMR spectra of **13–15** were based upon <sup>1</sup>H–<sup>13</sup>C HSQC 2-D correlation spectra. <sup>1</sup>H NMR Spectra of **13–16** can be found in Appendix Figures S38, S42, S46 and S49, respectively. <sup>13</sup>C NMR Spectra of **13–15** can be found in Appendix Figures S39, S43 and S47. IR data were collected using a Thermo Scientific Nicolet iS5 spectrometer. Spectra for **13–16** can be found in Appendix Figures 41, 45, 48 and 50. The intensities are reported relative to the most intense peak and are given in parentheses. Mass spectrometry (MS) analyses were conducted using a JEOL AccuTOF JMS-T100LC. UV–vis spectra were recorded on a Shimadzu UV-3101PC UV–vis/NIR scanning spectrophotometer.

## 2.3 SYNTHETIC DETAILS

### 2.3.1 Synthesis of [Li(THF)<sub>2</sub>][(Im<sup>tBu</sup>N)C(Ndipp)<sub>2</sub>] (**13**)

To a thawing solution of (dippN)<sub>2</sub>C (2.2 g, 6.13 mmol) in THF (12 mL), [Li(Et<sub>2</sub>O)][Im<sup>tBu</sup>N] (1.7 g, 6.13 mmol) was added forming a pale yellow solution. The reaction mixture was subsequently

allowed to slowly warm to room temperature over several hours. After 12 h, the volatiles were removed under reduced pressure to give a tacky, pale yellow oil. The material was triturated with hexanes (4 mL) and the solvent subsequently removed in vacuo. Addition of hexanes (4 mL) followed by stirring for 30 min resulted in formation of a solid, white powder. The suspension was filtered over a medium porosity glass frit, and the collected solid was washed with hexanes (3 mL) giving **13** as a white powder. Yield: 1.7 g, 40%.  $^1\text{H}$  NMR (25 °C, 400 MHz,  $\text{C}_6\text{D}_6$ ):  $\delta$  1.12 (br s, 8H, THF), 1.25 (d, 12H,  $J_{\text{HH}} = 8$  Hz,  $\text{CHMe}_2$ ), 1.48 (d, 12H,  $J_{\text{HH}} = 8$  Hz,  $\text{CHMe}_2$ ), 1.67 (s, 18H,  $\text{CCH}_3$ ), 3.13 (br s, 8H, THF), 4.05 (sept, 4H,  $J_{\text{HH}} = 8$  Hz,  $\text{CHMe}_2$ ), 6.22 (s, 2H, *ImidH*), 6.99 (t, 2H,  $J_{\text{HH}} = 8$  Hz, *ArH*), 7.27 (d, 4H,  $J_{\text{HH}} = 8$  Hz, *ArH*).  $^{13}\text{C}\{^1\text{H}\}$  NMR (25 °C, 100.58 MHz,  $\text{C}_6\text{H}_6$ ):  $\delta$  24.5 ( $\text{CHMe}_2$ ), 24.6 ( $\text{CHMe}_2$ ), 25.2 (THF), 27.9 ( $\text{CHMe}_2$ ), 29.5 ( $\text{CMe}_3$ ), 57.2 ( $\text{CMe}_3$ ), 67.9 (THF), 109.9 (*ImidH*), 119.9 (*aryl*), 123.4 (*aryl*), 143.3 (*aryl*), 148.1 (tBuCN<sub>3</sub>), 159.8 (dippCN<sub>3</sub>), one aryl resonance not observed.  $^7\text{Li}\{^1\text{H}\}$  NMR (25 °C, 155 MHz,  $\text{C}_6\text{D}_6$ ):  $\delta$  -0.8 (s). IR (KBr pellet): 3393 (w), 3196 (w), 3161 (w), 3140 (w), 3108 (w), 3046 (m), 3008 (m), 2978 (s), 2957 (s), 2934 (s), 2883 (m), 2863 (s), 2810 (w), 2744 (w), 2700 (w), 2484 (w), 2444 (w), 2398 (w), 2355 (w), 2295 (w), 2158 (w), 2051 (w), 1922 (w), 1897 (w), 1849 (w), 1877 (w), 1785 (w), 1755 (w), 1598 (m), 1589 (m), 1561 (s), 1537 (s), 1480 (s), 1453 (s), 1431 (s), 1424 (s), 1391 (s), 1363 (s), 1349 (s), 1324 (s), 1291 (s), 1240 (s), 1228 (s), 1193 (s), 1159 (m), 1139 (m), 1110 (m), 1087 (m), 1085 (m), 1039 (m), 996 (m), 960 (m), 934 (m), 915 (m), 898 (m), 859 (m), 826 (m), 809 (m), 797 (m), 793 (m), 757 (m), 722 (m), 715 (m), 701 (m), 649 (m), 617 (w), 609 (m), 585 (m), 576 (w), 567 (m), 556 (m), 547 (m), 525 (w), 496 (m), 482 (m), 465 (m), 441 (m), 431 (m), 414 (m), 405 (w).

### 2.3.2 Synthesis of (**Im**<sup>tBu</sup>N)C(Ndipp)(NHdipp) (**14**)

To a 20 mL scintillation vial equipped with a small magnetic stir bar, **13** (405 mg, 0.728 mmol) and Et<sub>2</sub>O (10 mL) were added. To the stirring solution were added six drops of deionized H<sub>2</sub>O and the mixture was vigorously stirred for 30 min. The colorless solution was dried over MgSO<sub>4</sub> and subsequently filtered through a medium porosity glass frit. The filter cake was washed with Et<sub>2</sub>O (2 mL) and the filtrate was dried under vacuum to give a white solid. Yield: 389 mg, 96% yield.  $^1\text{H}$  NMR (25 °C, 400 MHz,  $\text{C}_6\text{D}_6$ ):  $\delta$  1.02 (d, 6H,  $J_{\text{HH}} = 8$  Hz,  $\text{CHMe}_2$ ), 1.33 (d, 6H,  $J_{\text{HH}} = 8$  Hz,  $\text{CHMe}_2$ ), 1.39 (d, 6H,  $\text{CHMe}_2$ , overlaps with  $\text{CMe}_3$  resonance), 1.42 (s, 18H,  $J_{\text{HH}} = 8$  Hz,  $\text{CMe}_3$ ), 3.64 (sept, 2H,

$J_{\text{HH}} = 8 \text{ Hz}$ ,  $\text{CHMe}_2$ ), 3.89 (sept, 2H,  $J_{\text{HH}} = 4 \text{ Hz}$ ,  $\text{CHMe}_2$ ), 5.69 (s, 1H,  $\text{NH}$ ), 6.15 (s, 2H,  $\text{ImidH}$ ), 7.16–7.19 (m, 4H, *aryl*), 7.34 (d, 2H  $J_{\text{HH}} = 8 \text{ Hz}$ , *aryl*).  $^{13}\text{C}\{^1\text{H}\}$  NMR (25 °C, 100.58 MHz,  $\text{C}_6\text{H}_6$ ):  $\delta$  22.24 ( $\text{CHMe}_2$ ), 22.94 ( $\text{CHMe}_2$ ), 25.34 ( $\text{CHMe}_2$ ), 25.48 ( $\text{CHMe}_2$ ), 28.79 ( $\text{CHMe}_2$ ), 28.82 ( $\text{CHMe}_2$ ), 28.92 ( $\text{CMe}_3$ ), 58.06 ( $\text{CMe}_3$ ), 111.29 ( $\text{ImidH}$ ), 121.94 (*aryl*), 122.83 (*aryl*), 123.52 (*aryl*), 125.63 (*aryl*), 137.85 (*aryl*), 142.12 (*aryl*), 145.77 (*aryl*), 147.01, 150.24, 150.36. IR (KBr pellet): 3395 (w,  $\nu$   $\text{NH}$ ), 3164 (w), 3067 (w), 3053 (m), 3019 (m), 2976 (s), 2954 (s), 2922 (s), 2886 (m), 2865 (s), 2744 (w), 2711 (w), 2649 (w), 2615 (w), 2597 (w), 2401 (w), 2348 (w), 2295 (w), 1998 (w), 1887 (w), 1854 (w), 1846 (w), 1790 (w), 1724 (w), 1695 (w), 1650 (w), 1601 (s), 1564 (s), 1527 (s), 1477 (s), 1462 (s), 1453 (s), 1428 (s), 1422 (s), 1402 (s), 1383 (s), 1364 (s), 1331 (s), 1318 (s), 1280 (m), 1248 (s), 1232 (s), 1208 (s), 1198 (s), 1177 (m), 1166 (m), 1143 (w), 1112 (s), 1098 (m), 1058 (w), 1045 (w), 1038 (w), 993 (w), 969 (w), 956 (w), 935 (w), 892 (w), 883 (w), 863 (m), 827 (w), 810 (w), 796 (w), 775 (w), 755 (s), 725 (w), 712 (m), 668 (s), 641 (w), 627 (w), 612 (w), 568 (w), 553 (w), 534 (w), 514 (w), 492 (w), 466 (w), 447 (w), 429 (w). ESI-MS:  $m/z$  558.463 ( $[\text{M}+\text{H}]^+$ ; Calcd  $m/z$  558.453).

### 2.3.3 Synthesis of $[\text{K}(\text{THF})][(\text{Im}^{\text{tBu}}\text{NC}(\text{Ndipp})_2]$ (**15**)

To a stirring solution of **14** (225 mg, 0.403 mmol) in THF (6 mL) activated KH was added (81 mg, 2.02 mmol). While stirring, evolution of  $\text{H}_2$  was observed and the reaction was allowed to stir for 12 h. The mixture was filtered through celite supported on glass wool to remove excess KH affording a pale yellow solution. Removal of the volatiles in vacuo produced an off-white semi-solid that upon trituration with hexanes (3 mL) gave a white powder. Yield: 200 mg, 83%.  $^1\text{H}$  NMR (25 °C, 600 MHz,  $\text{C}_6\text{D}_6$ ):  $\delta$  1.16 (br d, 12H,  $\text{CHMe}_2$ ), 1.39 (d, 4H, THF), 1.46 (d, 12H,  $J_{\text{HH}} = 6 \text{ Hz}$ ,  $\text{CHMe}_2$ ), 1.68 (s, 18H,  $\text{CMe}_3$ ), 3.52 (t, 4H, THF), 3.99 (br s, 4H,  $\text{CHMe}_2$ ), 6.22 (s, 2H,  $\text{ImidH}$ ), 6.82 (br s, 2H, *aryl*), 7.11–7.16 (d, 4H,  $J_{\text{HH}} = 12 \text{ Hz}$ , *aryl*).  $^{13}\text{C}\{^1\text{H}\}$  NMR (25 °C, 100.58 MHz,  $\text{C}_6\text{H}_6$ ):  $\delta$  24.33 ( $\text{CHMe}_2$ ), 25.92 ( $\text{CHMe}_2$ ), 27.73 ( $\text{CHMe}_2$ ), 29.06 (THF), 29.87 ( $\text{CMe}_3$ ), 59.17 ( $\text{CMe}_3$ ), 67.95 (THF), 109.81 ( $\text{ImidH}$ ), 122.67 (*aryl*), 147.53 ( $^{\text{tBu}}\text{CN}_3$ ), 157.86 ( $^{\text{dipp}}\text{CN}_3$ ), three aryl resonances not observed. IR (KBr pellet): 3389 (w), 3153 (w), 3040 (w), 2954 (s), 2921 (m), 2862 (m), 2346 (w), 1327 (w), 1596 (m), 1549 (s), 1538 (s), 1473 (m), 1450 (s), 1416 (s), 1373 (s), 1366 (s), 1348 (s), 1327 (m), 1311 (m), 1295 (m), 1240 (m), 1231 (s), 1189 (m), 1155 (w), 1138 (w), 1098 (w), 1094 (w), 1880 (w), 1045 (w),

1025 (w), 989 (w), 954 (w), 932 (w), 885 (w), 871 (w), 853 (w), 817 (w), 801 (w), 794 (w), 765 (w), 755 (w), 714 (w), 704 (w), 661 (w), 553 (w), 438 (w), 411 (w).

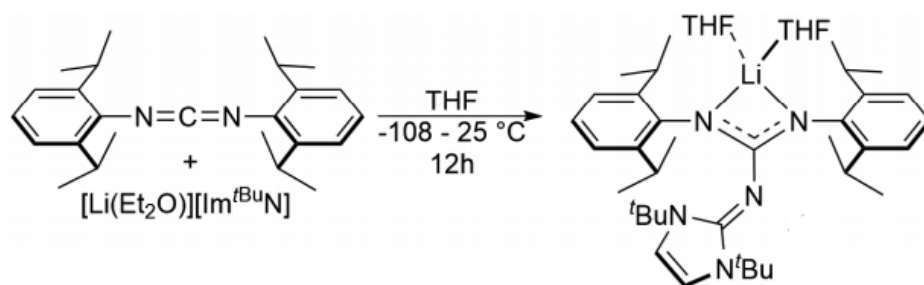
### 2.3.4 Synthesis of $\{[(\text{Im}^{\text{tBu}}\text{N})\text{C}(\text{Ndipp})_2]\text{FeBr}\}_2$ (**16**)

To a 20 mL scintillation vial equipped with a small stir bar,  $\text{FeBr}_2$  (90 mg, 0.312 mmol) and THF (3 mL) were added and the suspension was stirred for 20 min to ensure complete dissolution of the  $\text{FeBr}_2$  to give a brown solution. To this, a THF (3 mL) solution of **15** (207 mg, 0.347 mmol) was added dropwise with stirring. Upon addition, the formation of a brown-gray suspension with insoluble gray particulate was observed. The reaction mixture was stirred for 20 h and subsequently filtered through celite supported on glass wool to afford a yellow solution. Removal of the solvent under reduced pressure afforded a bright yellow semi-solid. The solid was triturated with hexanes (2 mL) three times with removal of the solvent under reduced pressure each time, eventually producing **16** as a bright yellow powder. Storage of a toluene (1 mL) and hexane (3 mL) solution at  $-20\text{ }^\circ\text{C}$  for 12 h afforded **16** as a yellow crystalline material. Yield: 132 mg (61% yield).  $^1\text{H}$  NMR (25  $^\circ\text{C}$ , 400 MHz,  $\text{C}_6\text{D}_6$ ):  $\delta$  -23.48 (s, 2H), -14.82 (s, 4H), -10.24 (s, 12H,  $\text{CHMe}_2$ ), 1.09 (s, 12H,  $\text{CHMe}_2$ ), 6.88 (br s, 18H,  $\text{CMe}_3$ , overlaps with NMR solvent resonance), 14.64 (s, 2H), 23.46 (s, 4H). IR (KBr pellet): 3397 (w), 3204 (w), 3166 (w), 3054 (m), 2963 (w), 2929 (m), 2869 (m), 2810 (w), 2758 (w), 2715 (w), 2596 (w), 2281 (w), 2241 (w), 2165 (w), 1914 (w), 1658 (w), 1598 (s), 1563 (s), 1463 (s), 1431 (s), 1419 (m), 1378 (m), 1368 (m), 1323 (s), 1231 (m), 1199 (m), 1164 (w), 1147 (w), 1108 (w), 1085 (w), 1058 (w), 1027 (w), 999 (w), 958 (w), 937 (w), 922 (w), 883 (w), 861 (w), 824 (w), 796 (w), 768 (w), 756 (w), 724 (w), 707 (w), 673 (w), 663 (w), 624 (w), 588 (w), 569 (w), 548 (w), 535 (w), 526 (w), 518 (w), 475 (w), 410 (w), 400 (w). UV-vis (toluene, 0.10 mM, 25  $^\circ\text{C}$ ,  $\text{L mol}^{-1}\text{ cm}^{-1}$ ): 406 ( $\epsilon = 1897$ ).

## 2.4 RESULTS AND DISCUSSION

### 2.4.1 Ligand synthesis and characterization

A clear colorless solution of  $(\text{dippN})_2\text{C}$  slowly turns into a pale yellow faint solution upon addition of  $[\text{Li}(\text{Et}_2\text{O})][\text{Im}^{\text{tBu}}\text{N}]$  in THF. Reaction was done in thawing temperature in an attempt to minimize the decomposition of  $[\text{Li}(\text{Et}_2\text{O})][\text{Im}^{\text{tBu}}\text{N}]$  in THF, observed before by the formation of an orange solution of intractable composition after hours. We overcome this by allowing the solution to



**Scheme 2.4** Synthesis of  $[\text{Li}(\text{THF})_2][(\text{Im}^{\text{tBu}}\text{N})\text{C}(\text{Ndipp})_2]$  (**13**)

warm up for a period of 12 h followed by the removal of THF and addition of hexanes to precipitate  $\text{Li}(\text{THF})_2[(\text{Im}^{\text{tBu}}\text{N})\text{C}(\text{Ndipp})_2]$  (**13**) as a white powder.  $^1\text{H}$  NMR spectroscopy of the crude material revealed incomplete consumption of  $(\text{dippN})_2\text{C}$  in approximate 4:1 ratio of product to carbodiimide. Fortunately, the carbodiimide is very soluble in non-polar solvents, and thus is easily removed by hexane washing to afford **13** in a 40% yield. Crystalline material can be afforded by layering a concentrated solution of THF with hexanes (1:5) and storing it at  $-25\text{ }^\circ\text{C}$ .

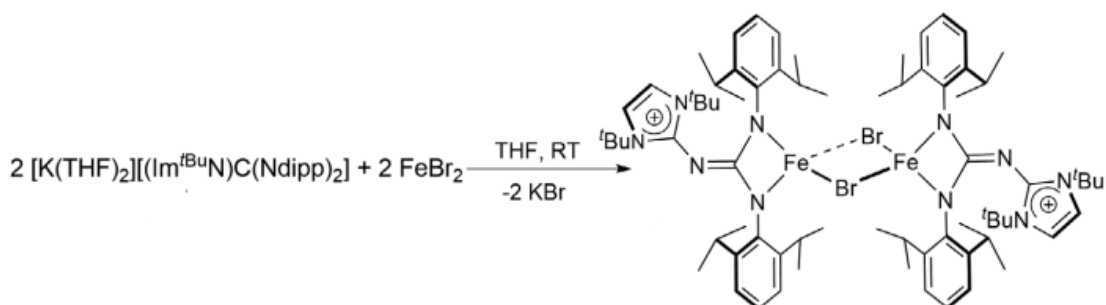
The  $^1\text{H}$  NMR spectra of **13** in  $\text{C}_6\text{D}_6$  is very well resolved at room temperature allowing for easy characterization, as opposed to compounds discussed in chapter 1. A characteristic peak for the tert-butyl protons in the backbone is observed at 1.67 ppm. The equivalent pendant isopropyl protons in the dipp moieties give rise to two doublets at 1.25 and 1.48 ppm corresponding to the methyl groups accompanied by a septet at 4.05 ppm characteristic of the methine protons. We observe two peaks at 1.12 and 3.13 ppm which account for two molecules of THF by integration, coordinated to the lithium cation, which is supported by the XRD structure (Figure 2.1). **13** exhibits a pseudo  $\text{C}_{2v}$  symmetry in solution, indicating the free rotation of the  $\text{Im}^{\text{tBu}}\text{N}$  group at the back of the guanidinate.

Treating of **13** with excess water in  $\text{Et}_2\text{O}$  affords the protonated species  $(\text{Im}^{\text{tBu}}\text{N})\text{C}(\text{Ndipp})(\text{NHdipp})$  **14** in nearly quantitative yield. The  $^1\text{H}$  NMR spectrum reveals sharp well-defined peaks indicative of only one conformation in solution. This observation is contrary to the expected complicated broad set of peaks typically seen in guanidines and ketimine-guanidines due to the conformational and tautomeric fluxionality they can exhibit.<sup>28, 29, 38</sup> The IR spectrum displays a characteristic band corresponding to the N-H vibrational frequency at  $3395\text{ cm}^{-1}$ .

Addition of excess activated KH to a stirring solution of **14** in THF for several hours affords  $[K(THF)][(Im^{tBu}NC(Ndipp)_2)]$  (**15**) in an 83% yield as a hexane-insoluble white solid.  $^1H$  NMR spectroscopy shows one set of signals qualitatively similar to those in **13**, but displays significant more peak broadening. For instance, the methyl protons of the isopropyl groups appear as a broad singlet and a slightly sharper doublet at 1.16 and 1.46 ppm, respectively. We attribute this broadening to potential fluxional behavior experienced by **15** in solution.

#### 2.4.2 Synthesis of an Iron $Im^{tBu}N$ -guanidinate

In an attempt to compare the structural and electronic features of our new ligand scaffold that includes an  $Im^{tBu}N$ -guanidinate and the electronic contributions of the  $Im^{tBu}N$  group, we metalated our ligand with iron to make direct comparisons to the well-defined iron guanidinate and ketimine-guanidinate complexes  $\{[(X)C(Ndipp)_2]FeBr\}_2$  ( $X = tBu_2C=N$  (**5a**);  $N(tPr)_2$  (**6a**)) differing only in the backbone, molecules previously reported by us.<sup>29</sup> Using an adapted procedure for the synthesis of **5a**, we found that  $\{[(Im^{tBu}N)C(Ndipp)_2]FeBr\}_2$  (**16**) can be synthesized by salt metathesis of  $FeBr_2$  with **15** in THF



**Scheme 2.5** Synthesis of  $\{[(Im^{tBu}N)C(Ndipp)_2]FeBr\}_2$  (**16**)

(Scheme 2.5). Previous attempts to synthesize **16** from salt metathesis of the metal bromide with **13** resulted in a complicated mixture of products containing LiBr, **16** and other intractable paramagnetic materials very hard to isolate. Complex **16** is very soluble in THF, partially soluble in aromatic solvents and slightly soluble in non-polar solvents. Storing a concentrated toluene solution at -25 °C affords pale-yellow crystalline material in a 61% yield. The  $^1H$  NMR spectrum of **16** in  $C_6D_6$  exhibits paramagnetic broadening from -23.5 to 23.5 ppm approximately with seven well resolved peaks with the ratio of 2 : 4



**Table 2.1** X-ray crystallographic data for **13** and **16**.

	<b>13</b>	<b>16</b> ·C <sub>7</sub> H <sub>8</sub>
Empirical formula	C <sub>44</sub> H <sub>64</sub> LiN <sub>5</sub> O <sub>2</sub>	C <sub>72</sub> H <sub>108</sub> Br <sub>2</sub> Fe <sub>2</sub> N <sub>10</sub> ·C <sub>7</sub> H <sub>8</sub>
Crystal habit, color	Plate, colorless	Plate, light brown
Crystal size (mm)	0.23 × 0.19 × 0.08	0.32 × 0.24 × 0.12
Crystal system	Monoclinic	Monoclinic
Space group	<i>P</i> 2 <sub>1</sub> / <i>c</i>	<i>P</i> 2 <sub>1</sub> / <i>c</i>
Volume (Å <sup>3</sup> )	4161.0(7)	7766.0(6)
<i>a</i>	21.230(2)	19.9200(9)
<i>b</i>	10.9407(11)	19.3080(9)
<i>c</i>	19.1462(19)	21.4082(10)
$\alpha$	90	90
$\beta$	110.663(2)	109.408(1)
$\gamma$	90	90
<i>Z</i>	4	4
<i>F<sub>w</sub></i> (g/mol)	702.05	1477.33
Density (Calcd) (Mg/m <sup>3</sup> )	1.140	1.264
Abs. coeff. (mm <sup>-1</sup> )	0.069	1.450
<i>F<sub>000</sub></i>	1560.0	3128.0
Total no. of reflns.	10205	21829
Unique reflns.	5960	12243
Final <i>R</i> indices [ <i>I</i> > 2σ( <i>I</i> )]	<i>R</i> <sub>1</sub> = 0.0822, <i>wR</i> <sub>2</sub> = 0.2085	<i>R</i> <sub>1</sub> = 0.0505, <i>wR</i> <sub>2</sub> = 0.1024
Largest diff. peak and hole (e/Å <sup>3</sup> )	0.65 and -0.66	0.45 and -0.52
GOF	1.041	0.982

: 12 : 12 : 18 : 2 : 4 confined in this range. The peak pattern suggests a C<sub>2</sub> symmetry in solution which indicates a symmetric κ<sup>2</sup>-chelation from the N<sub>dipp</sub> nitrogen into iron. In addition, a dynamic Im<sup>tBu</sup>N backbone is observed as opposed as the one noted in **13** or in the ketimine-guanidinate counterpart **5a**.<sup>29</sup>

### 2.4.3 Structural analyses and comparison

Analyses of structures **13** and **16** were performed through single-crystal X-Ray diffractometry at 100K to better elucidate the effect of the Im<sup>tBu</sup>N backbone in the ligand scaffold. We expected resonance contributions from the imine nitrogen in the backbone (Scheme 2.1, bottom) to the CN<sub>3</sub> ligand core to be observed through XRD analyses when comparing the metric parameters of **16** to the known structures of **5a** and **6a**. More specifically, if resonance form **K** (Scheme 2.1) is present in the ligand architecture of **13** and **16**, then a shorter N<sub>Im</sub>-CN<sub>3</sub> bond alongside with a longer CN<sub>3</sub>-N<sub>dipp</sub> is expected due to increasing anionic character in both N<sub>dipp</sub> nitrogens.

Figure 2.1 shows the solid-state structure of **13** and **16**. Both molecules crystallize in the monoclinic space group *P*2<sub>1</sub>/*c* as full molecules in the asymmetric unit. In the case of **16**, we are

discussing the parameters of only one half of the bimetallic unit, as both iron centers are crystallographically independent. (Table 2.1)

Inspection of the average  $C_{N3}-N_{dipp}$  bond between **13**, **16**, **5a** and **6a** follows the order of **16** (1.372 Å) > **6a** (1.355 Å)  $\approx$  **13** (1.352 Å) > **5a** (1.345 Å), with the average Fe- $N_{dipp}$  bond of **16** (2.008 Å)

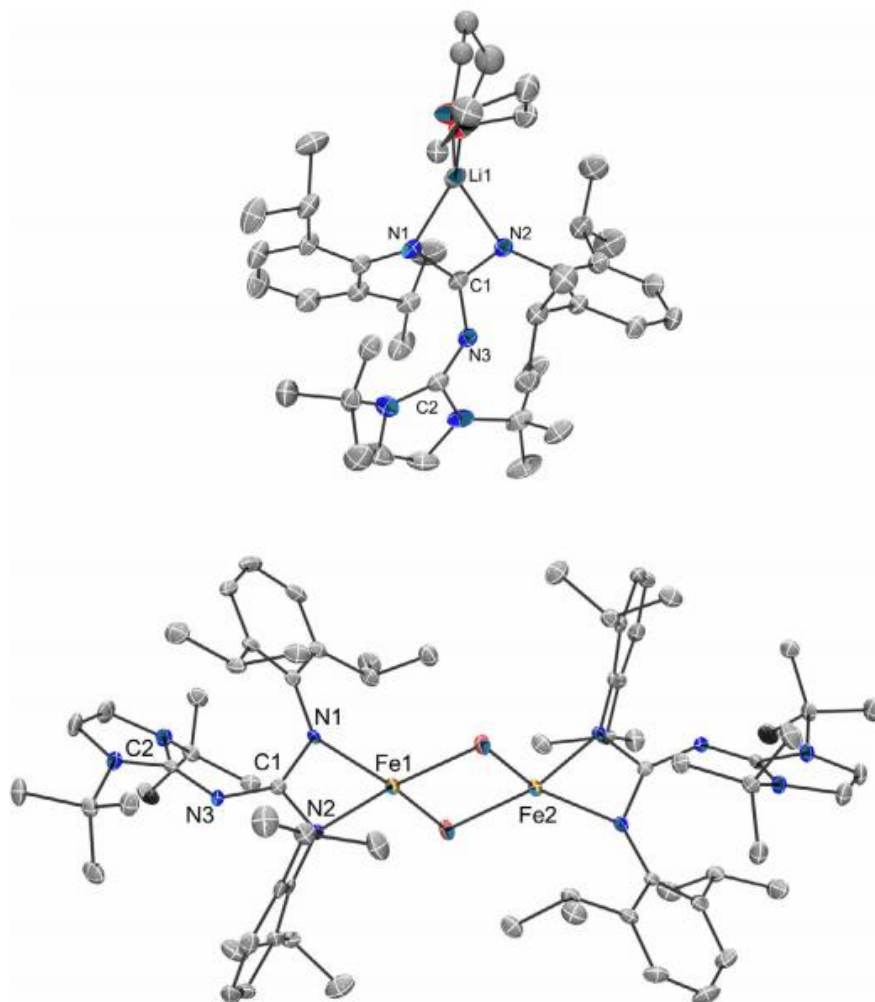
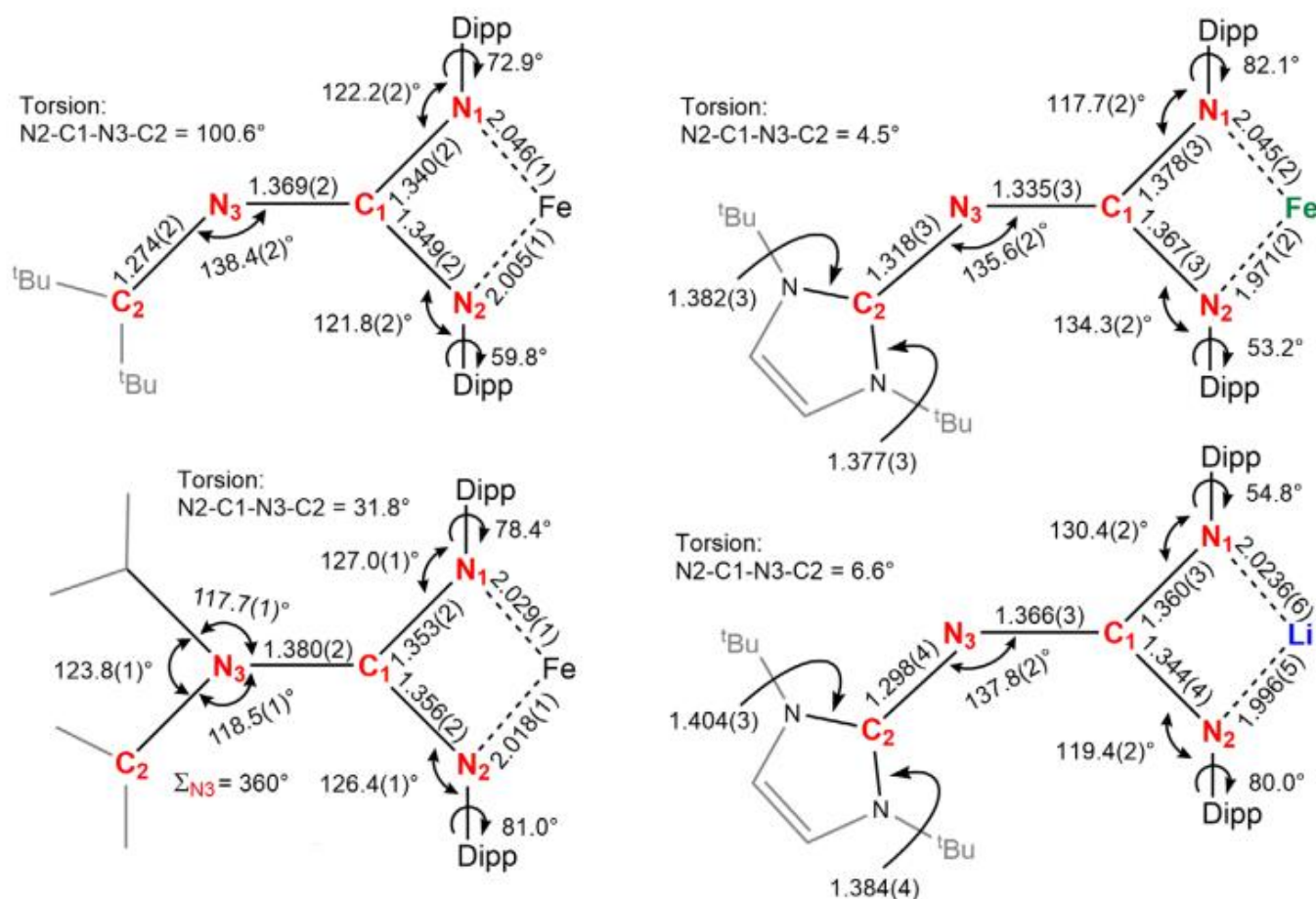


**Figure 2.1** ORTEP diagram of **13** (top) and **16**·C<sub>7</sub>H<sub>8</sub> (bottom). Hydrogens and the co-crystallized molecule of toluene omitted for clarity.

< **6a** (2.024 Å)  $\approx$  **5a** (2.026 Å). Because some bond metrics fall outside the  $3\sigma$  criterion, quantitative differences must be compared with care. However, qualitative assessment can be made because the general trend shows longer  $C_{N3}-N_{dipp}$  bonds and shorter Fe- $N_{dipp}$  bonds in **16**, suggesting that some



**Scheme 2.6** Comparison of selected bond distances (Å) and angles (°) in **13** and **16** vs. **5a** and **6a**.

ligand diamido resonance character **K** (Scheme 2.1) may be present in **16** as opposed as in **13**. This is further supported by comparing the  $C_{N3}-N_{Im}$  bonds found between **16** ( $N3-C1 = 1.335(3)$  Å) **13** ( $N3-C1 = 1.366(3)$  Å) and **5a** ( $N3-C1 = 1.369(2)$  Å) (Scheme 2.6). This shortening is consistent with increased  $C_{N3}-N_{Im}$  double bond character. In addition, the  $N3-C1$  bond in **16** is shorter than the 1.376 Å expected for a common  $C(sp^2)-N(sp^2)$  single bond<sup>39</sup> but longer than the 1.28(2) Å found in the  $C(sp^2)=N(sp^2)$  bond of the dianionic guanidinate ligand in  $[(CyN=C(NCy)_2]Ta(NMe_2)_3$  (Cy = cyclohexyl).<sup>40</sup> Moreover, the  $C_{Im}-N_{Im}$  bond of **16** ( $N3-C2 = 1.318(3)$  Å) is elongated when compared to that of **13** ( $N3-C2 = 1.298(4)$  Å) or **5a** (1.274(2) Å). Complimentary, the torsional angle in **16** ( $N2-C1-N3-C2 = 4.5^\circ$ ) is close to zero as is expected for a  $C_{N3}-N_{Im}$  double bond. These metric parameters show the electronic structure of **16** contains a considerable imidazolium-diamido resonance

contribution (Scheme 3, **K**). The differences between the ligand electronics from **13** and **16** clearly demonstrate an electronically flexible guanidinate ligand manifold confining a  $\text{Im}^{\text{tBu}}\text{N}$  backbone.

#### 2.4.4 Electronic absorption spectroscopy comparison

If electronic differences among **16**, **5a** and **6a** exist, they should be easily observed through electronic absorption spectroscopy. In fact, we previously reported the UV-vis absorption spectra for iron ketimine-guanidates, e.g. **5a**, and found that they are more related to amidinates than guanidates, e.g. **6a**, despite the  $\text{CN}_3$  ligand core found in both.<sup>29</sup> Because the N-amine lone pair on the backbone of guanidates can conjugate into the  $\text{CN}_3$  core, a canonical iminium-diamido form, like that on **6a**, can be observed. It can be expected that the electronic absorption spectrum of **16** might be similar to **6a** because of its solid-state imidazolium-diamido resonance. Unexpectedly, the UV-vis absorption maximum of **16** ( $\lambda_{\text{max}} = 400 \text{ nm}$ ) is not significantly different when compared to **5a** ( $\lambda_{\text{max}} = 402 \text{ nm}$ ),

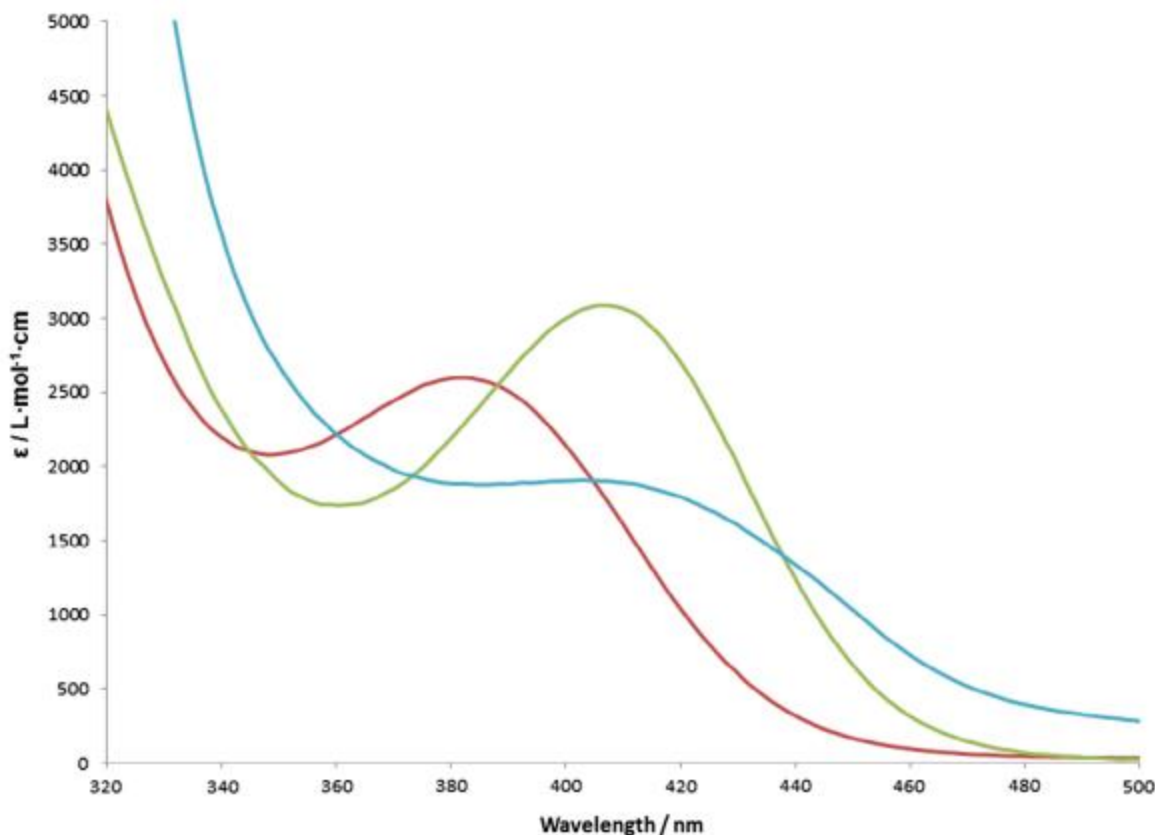


**Figure 2.2** Room temperature electronic absorption spectra for **16** (0.10 mM; blue), **5a** (0.09 mM; green), and **6a** (0.15 mM; red) in THF.

both being red-shifted from **6a** ( $\lambda_{\text{max}} = 383 \text{ nm}$ ) (Figure 2.2). A possible explanation is that, in solution, there is potentially less imidazolium-diamido resonance character in the former than in the solid-state.

In addition to this, further comparisons of electronic properties of **16**, **5a**, and **6a** through their magnetic susceptibilities were made. However, measuring room-temperature solution-phase magnetic moment of **16** by Evans' method was impeded by the limited solubility of crystalline samples of **16** in  $\text{C}_6\text{D}_6$ .

### 2.4.5 Electrochemistry

In our previous studies of **5a** and **6a**,<sup>29</sup> electrochemical analyses revealed that ketimine-guanidines are inferior electron donors when compared to guanidines when ligated to iron. In order to evaluate the effect of incorporating an  $\text{Im}^{\text{tBu}}\text{N}$  backbone in a guanidinate scaffold we examined the solution-phase redox properties of **16** by cyclic voltammetry. The cyclic voltammetry (CV) of **16** was done in THF with  $[\text{NBu}_4][\text{PF}_6]$  as the supporting electrolyte and using  $[\text{Cp}_2\text{Fe}]^{0/+}$  as the internal

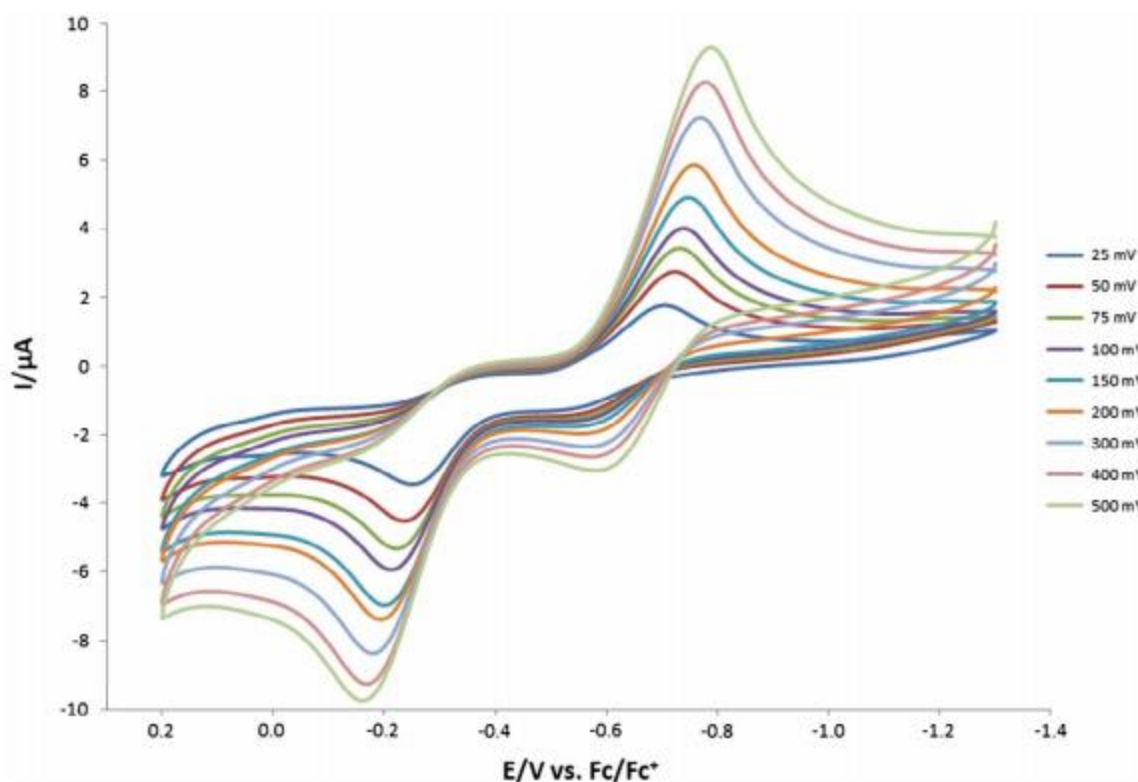


**Figure 2.3** Cyclic voltammogram of **16** in THF with  $[\text{NBu}_4][\text{PF}_6]$  as supporting electrolyte (vs  $[\text{Cp}_2\text{Fe}]^{0/+}$ )

reference, as shown in Figure 3. Qualitatively, the CV of **16** is very similar to that of both **5a** and **6a**,<sup>29</sup> as it shows the same electrochemical features including an irreversible oxidation wave at around  $E_{1/2} = -0.2$  V and a Fe(II)/Fe(III) redox couple at  $E_{1/2} = -0.67$  V (Appendix Figure S51). Notably, this peak is cathodically shifted by greater than 200 mV from the oxidation potentials of **5a** ( $E_{1/2} = -0.42$  V) and **6a** ( $E_{1/2} = -0.45$  V). Additionally, the oxidation wave in **16** is also shifted by the same potential from the comparable feature in **5a** and **6a**.

Through this comparison, the iron in **16** is clearly more electron rich than that of the iron centers in both **5a** and **6a**, giving evidence of a more electron donating ligand. This points out that having an Im<sup>tBu</sup>N group appended to a guanidinate gives a more electron rich system than that of a ketimine guanidinate. Indeed, in this case, the Im<sup>tBu</sup>N- group shows to be a better electron contributor to a guanidinate than the <sup>i</sup>Pr<sub>2</sub>N- group in **6a**. This observation does not correlate with the differences observed in the electronic absorption spectra (vide supra), meaning that potential inductive effects cannot be discounted.

## 2.5 CONCLUSION

In our efforts to build and design a strong electron-donating guanidinate, we have attached an Im<sup>tBu</sup>N- group to the backbone of a guanidinate. This was chosen because of the known ylidic imidazolium-imido resonances that Im<sup>tBu</sup>N- possesses, making it suitable for a  $\pi$ -conjugation into a CN<sub>3</sub> guanidinate core, expected to increase the ligand donor strength. The Im<sup>R</sup>N-guanidinate [Li(THF)<sub>2</sub>][(Im<sup>tBu</sup>N)C(Ndipp)<sub>2</sub>] (**13**) can be readily synthesized in a single step from known starting materials and subsequent reactions afford the Fe(II) complex {[(Im<sup>tBu</sup>N)C(Ndipp)<sub>2</sub>]FeBr}<sub>2</sub> (**16**). Comparing this iron complex via crystallographic bond metrics, electronic absorption spectroscopy and cyclic voltammetry with previously reported Fe(II) guanidinate complexes {[(X)C(Ndipp)<sub>2</sub>]FeBr}<sub>2</sub> (X = <sup>t</sup>Bu<sub>2</sub>C=N (**5a**); N(<sup>i</sup>Pr)<sub>2</sub> (**6a**)) clearly shows that the Im<sup>tBu</sup>N- group provides an electronically flexible guanidinate backbone, as well as unique and superior electron donating properties. The dominant resonance structure in **16** is found to be **K** (scheme 2.1). With this new Im<sup>tBu</sup>N- guanidinate ligand, we will explore its reduction chemistry on iron as well as other 3d-metals.

## REFERENCES

- (1) M. Castillo, O. Barreda, A. Maity, B. Barraza, J. Lu, A. J. Metta-Magana and S. Fortier, *J. Coord. Chem.*, **2016**, DOI:10.1080/00958972.2016.1167198
- (2) M. Tamm, D. Petrovic, S. Randoll, S. Beer, T. Bannenberg, P.G. Jones. *Org. Biomol. Chem.*, **2007**, 5, 523.
- (3) M. Tamm, S. Randoll, T. Bannenberg, E. Herdtweck. *Chem. Commun.*, **2004**, 876.
- (4) M. Tamm, S. Randoll, E. Herdtweck, N. Kleigrew, G. Kehr, G. Erker, B. Rieger. *Dalton Trans.*, **2006**, 459.
- (5) I.S.R. Karmel, M. Botoshansky, M. Tamm, M.S. Eisen. *Inorg. Chem.*, **2014**, 53, 694.
- (6) I.S.R. Karmel, N. Fridman, M. Tamm, M.S. Eisen. *J. Am. Chem. Soc.*, **2014**, 136, 17180.
- (7) K. Nomura, B.K. Bahuleyan, S. Zhang, P.M. Veerasha Sharma, S. Katao, A. Igarashi, A. Inagaki, M. Tamm. *Inorg. Chem.*, **2014**, 53, 607.
- (8) D. Shoken, M. Sharma, M. Botoshansky, M. Tamm, M.S. Eisen. *J. Am. Chem. Soc.*, **2013**, 135, 12592..
- (9) A.G. Trambitas, D. Melcher, L. Hartenstein, P.W. Roesky, C. Daniliuc, P.G. Jones, M. Tamm. *Inorg. Chem.*, **2012**, 51, 6753.
- (10) A.G. Trambitas, T.K. Panda, J. Jenter, P.W. Roesky, C. Daniliuc, C.G. Hrib, P.G. Jones, M. Tamm. *Inorg. Chem.*, **2010**, 49, 2435.
- (11) A.G. Trambitas, J. Yang, D. Melcher, C.G. Daniliuc, P.G. Jones, Z. Xie, M. Tamm. *Organometallics*, **2011**, 30, 1122.
- (12) T.K. Panda, A.G. Trambitas, T. Bannenberg, C.G. Hrib, S. Randoll, P.G. Jones, M. Tamm. *Inorg. Chem.*, **2009**, 48, 5462.
- (13) A. Glöckner, T. Bannenberg, C.G. Daniliuc, P.G. Jones, M. Tamm. *Inorg. Chem.*, **2012**, 51, 4368.
- (14) G. Frison, A. Sevin. *J. Chem. Soc.*, **2002**, Perkin Trans. 2, 1692.

- (15) N. Kuhn, M. Göhner, M. Grathwohl, J. Wiethoff, G. Frenking, Y. Chen. *Z. Anorg. Allg. Chem.*, **2003**, 629, 793.
- (16) V. Raab, K. Harms, J. Sundermeyer, B. Kovačević, Z.B. Maksić. *J. Org. Chem.*, **2003**, 68, 8790.
- (17) S. Beer, C.G. Hrib, P.G. Jones, K. Brandhorst, J. Grunenberg, M. Tamm. *Angew. Chem. Int. Ed.*, **2007**, 46, 8890.
- (18) D. Petrovic, T. Bannenberg, S. Randoll, P.G. Jones, M. Tamm. *Dalton Trans.*, **2007**, 2812.
- (19) D. Petrovic, T. Glöge, T. Bannenberg, C.G. Hrib, S. Randoll, P.G. Jones, M. Tamm. *Eur. J. Inorg. Chem.*, **2007**, 3472.
- (20) T.K. Panda, D. Petrovic, T. Bannenberg, C.G. Hrib, P.G. Jones, M. Tamm. *Inorg. Chim. Acta*, 361, **2008**, 2236.
- (21) J. Börner, S. Herres-Pawlis, U. Flörke, K. Huber. *Eur. J. Inorg. Chem.*, **2007**, 5645.
- (22) D. Petrovic, C.G. Hrib, S. Randoll, P.G. Jones, M. Tamm. *Organometallics*, **2008**, 27, 778.
- (23) A. Hoffmann, J. Börner, U. Flörke, S. Herres-Pawlis. *Inorg. Chim. Acta*, **2009**, 362, 1185.
- (24) T. Glöge, D. Petrovic, C. Hrib, P.G. Jones, M. Tamm. *Eur. J. Inorg. Chem.*, **2009**, 4538.
- (25) T. Glöge, D. Petrovic, C.G. Hrib, C. Daniliuc, E. Herdtweck, P.G. Jones, M. Tamm. *Z. Anorg. Allg. Chem.*, **2010**, 636, 2303.
- (26) S. Dastgir, G.G. Lavoie. *Dalton Trans.*, **2012**, 41, 9651.
- (27) S. Dastgir, G.G. Lavoie. *Dalton Trans.*, **2010**, 39, 6943.
- (28) A.K. Maity, S. Fortier, L. Griego, A.J. Metta-Magaña. *Inorg. Chem.*, **2014**, 53, 8155.
- (29) A.K. Maity, A.J. Metta-Magaña, S. Fortier. *Inorg. Chem.*, **2015**, 54, 10030.
- (30) P.L. Damon, C.J. Liss, R.A. Lewis, S. Morochnik, D.E. Szpunar, J. Telser, T.W. Hayton. *Inorg. Chem.*, **2015**, 54, 10081.
- (31) J.A. Soderquist, I. Rivera. *Tetrahedron Lett*, **1988**, 29, 3195.
- (32) M. Findlater, N.J. Hill, A.H. Cowley. *Dalton Trans.*, **2008**, 4419.



- (33) SMART Apex II. Bruker AXS Inc., Madison, WI (**2005**).
- (34) SAINT Software User's Guide. Bruker AXS Inc., Madison, WI (**2005**).
- (35) R. Blessing. *Acta Crystallogr. A*, **1995**, 51, 33.
- (36) G.M. Sheldrick. SHELXTL, Bruker Analytical X-Ray Systems Inc., Madison, WI (**2001**).
- (37) O.V. Dolomanov, L.J. Bourhis, R.J. Gildea, J.A.K. Howard, H. Puschmann. *J. Appl. Crystallogr.*, **2009**, 42, 339.
- (38) M.P. Coles. *Dalton Trans.*, **2006**, 985.
- (39) F.H. Allen, O. Kennard, D.G. Watson, L. Brammer, A.G. Orpen, R. Taylor. *J. Chem. Soc.*, **1987**, Perkin Trans. 2, S1.
- (40) M.K.T. Tin, G.P.A. Yap, D.S. Richeson. *Inorg. Chem.*, **1998**, 37, 6728.
- (41) Gokel, G. W.; Cram, D. J.; Liotta, C. L.; Harris, H. P.; Cook, F. L. *J. Org.Chem.* **1974**, 39, 2445.

## Appendix

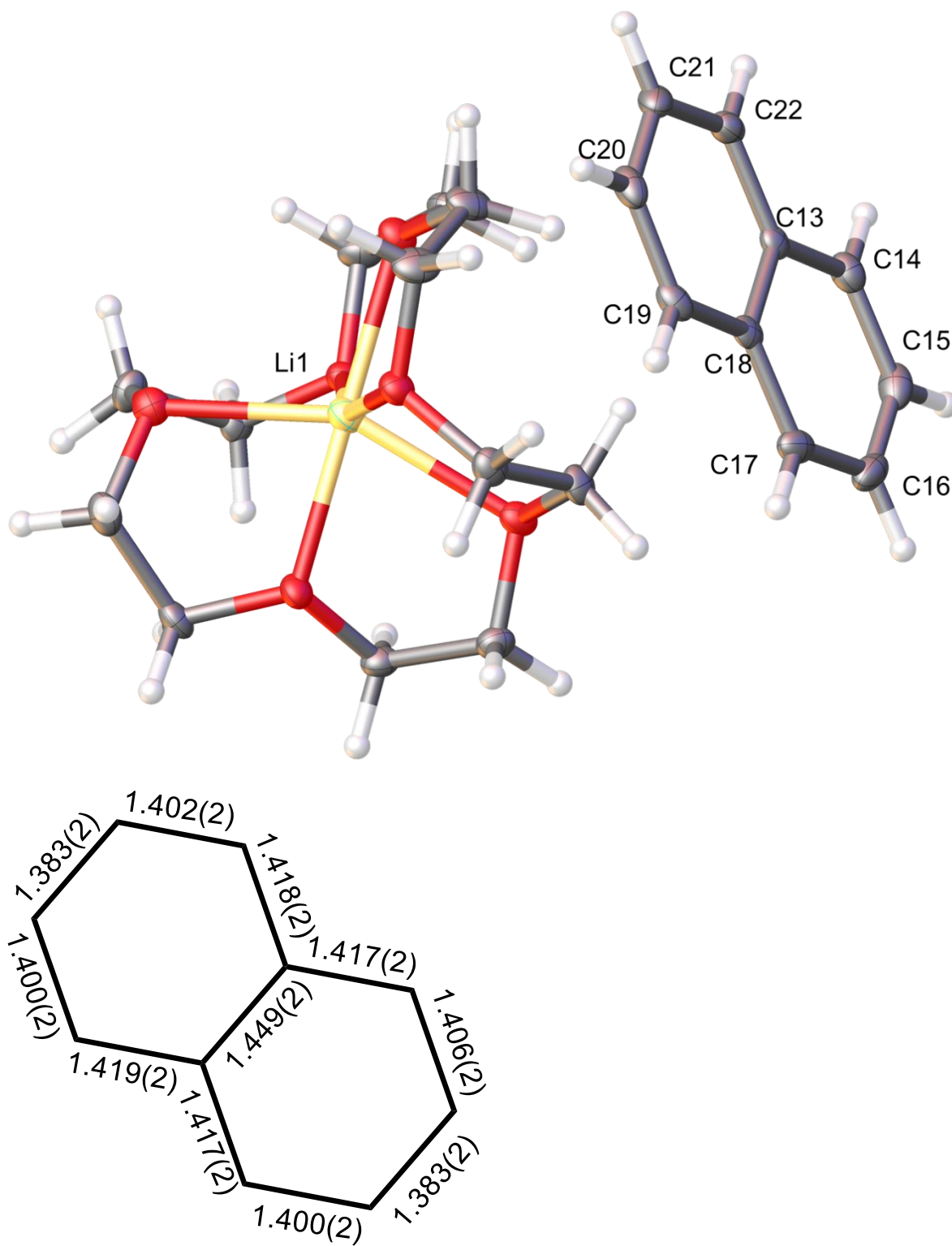


**Figure S1.** Solid-state molecular structure of **1** with 50% probability ellipsoids and respective bond length diagram.

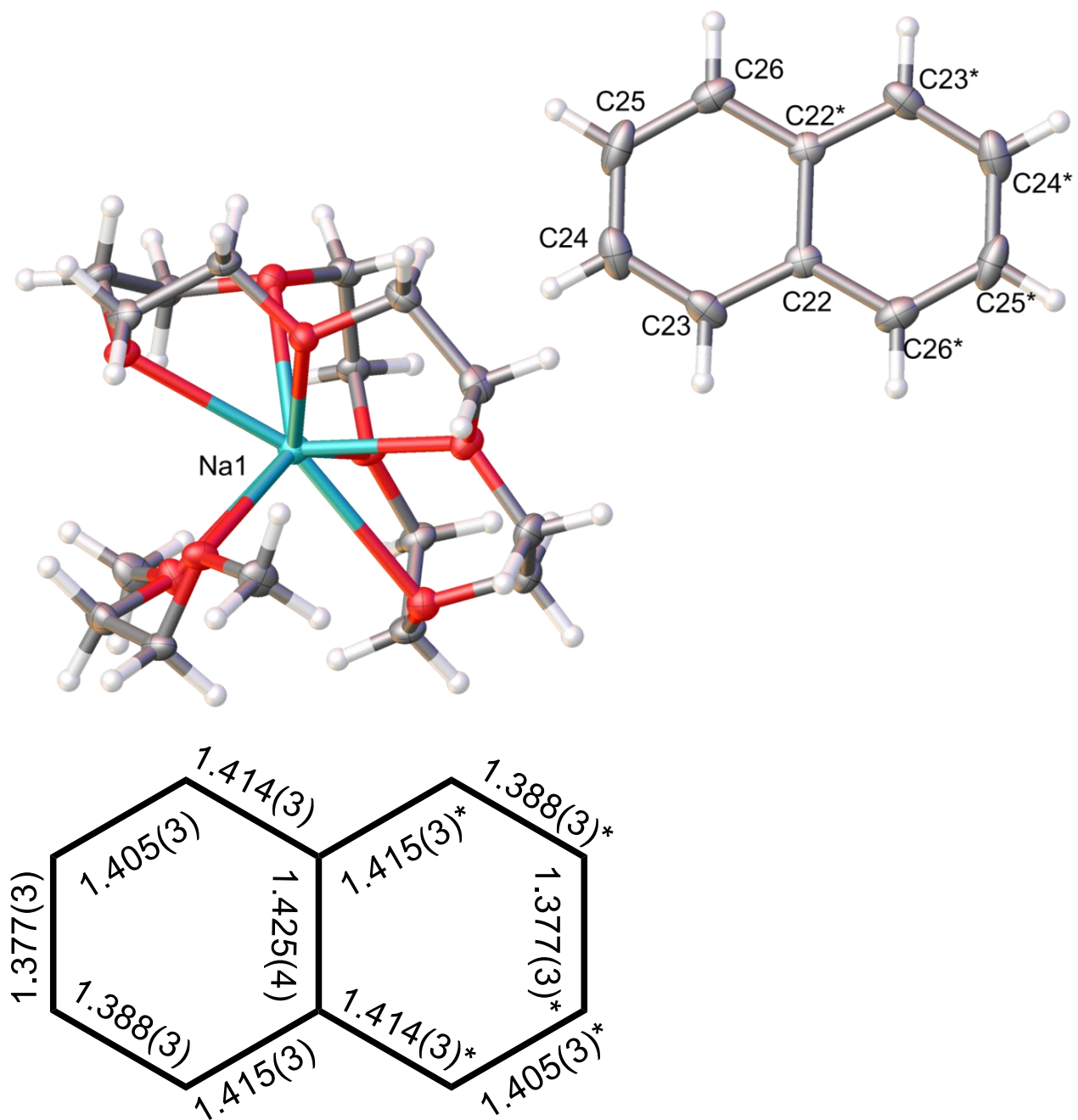


**Figure S2.** Solid-state molecular structure of 2 with 50% probability ellipsoids and respective bond length diagram. Asterisks denote symmetry generated atoms and bond lengths.

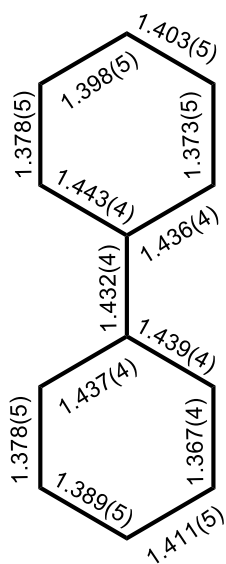
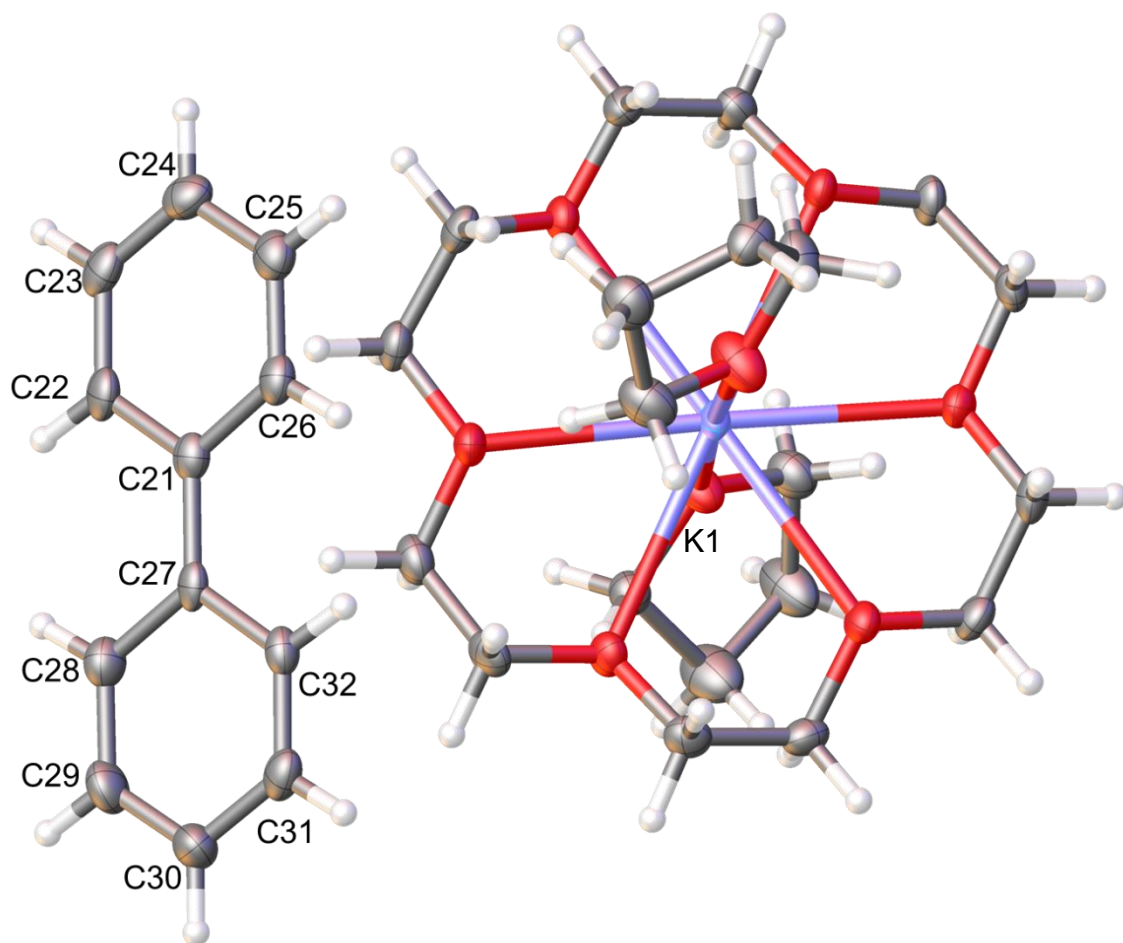


**Figure S3.** Solid-state molecular structure of **6** with 50% probability ellipsoids and respective bond length diagram.

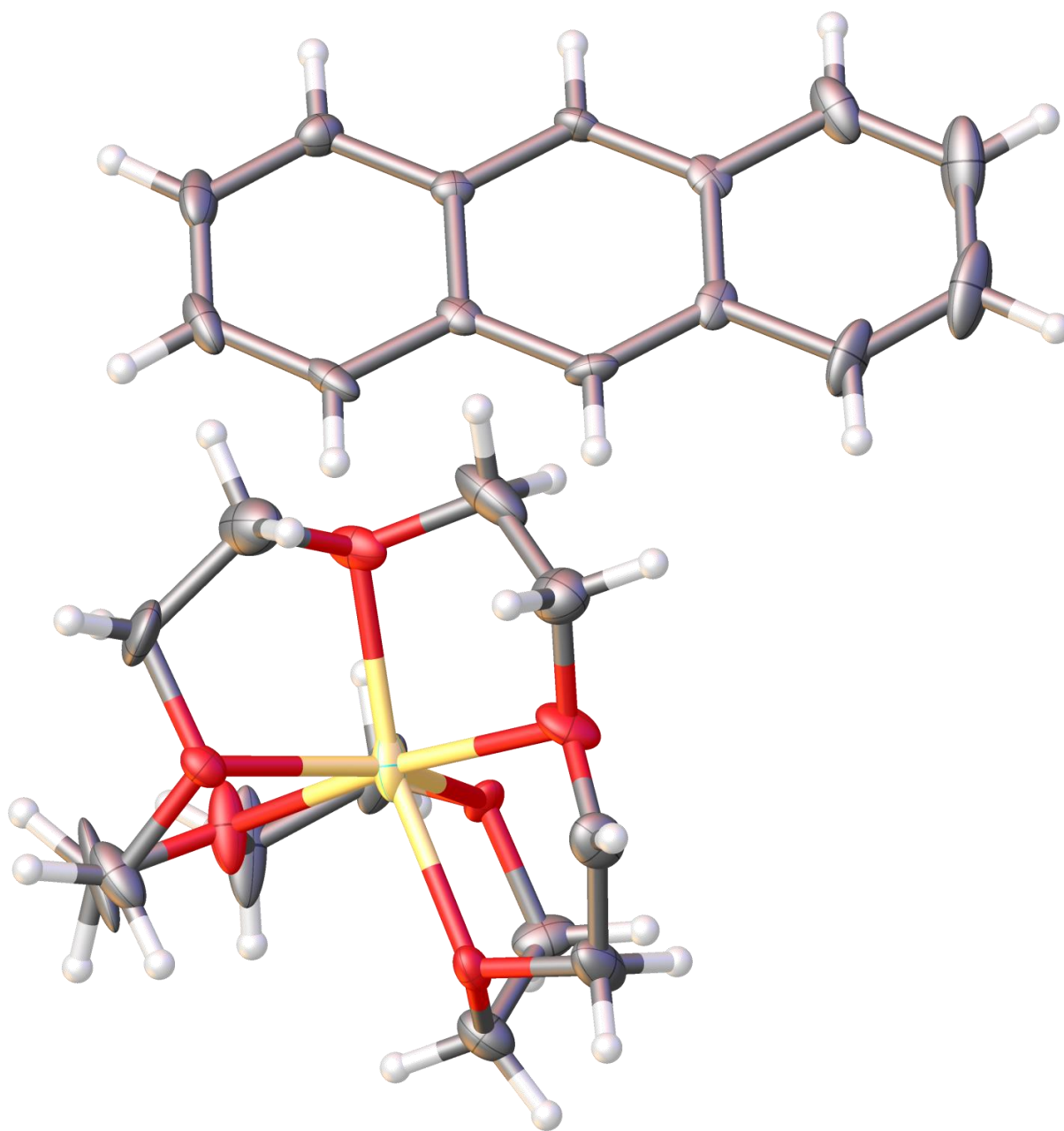


**Figure S4.** Diagram of the incompletely refined molecular structure of **7** presented to demonstrate connectivity only.

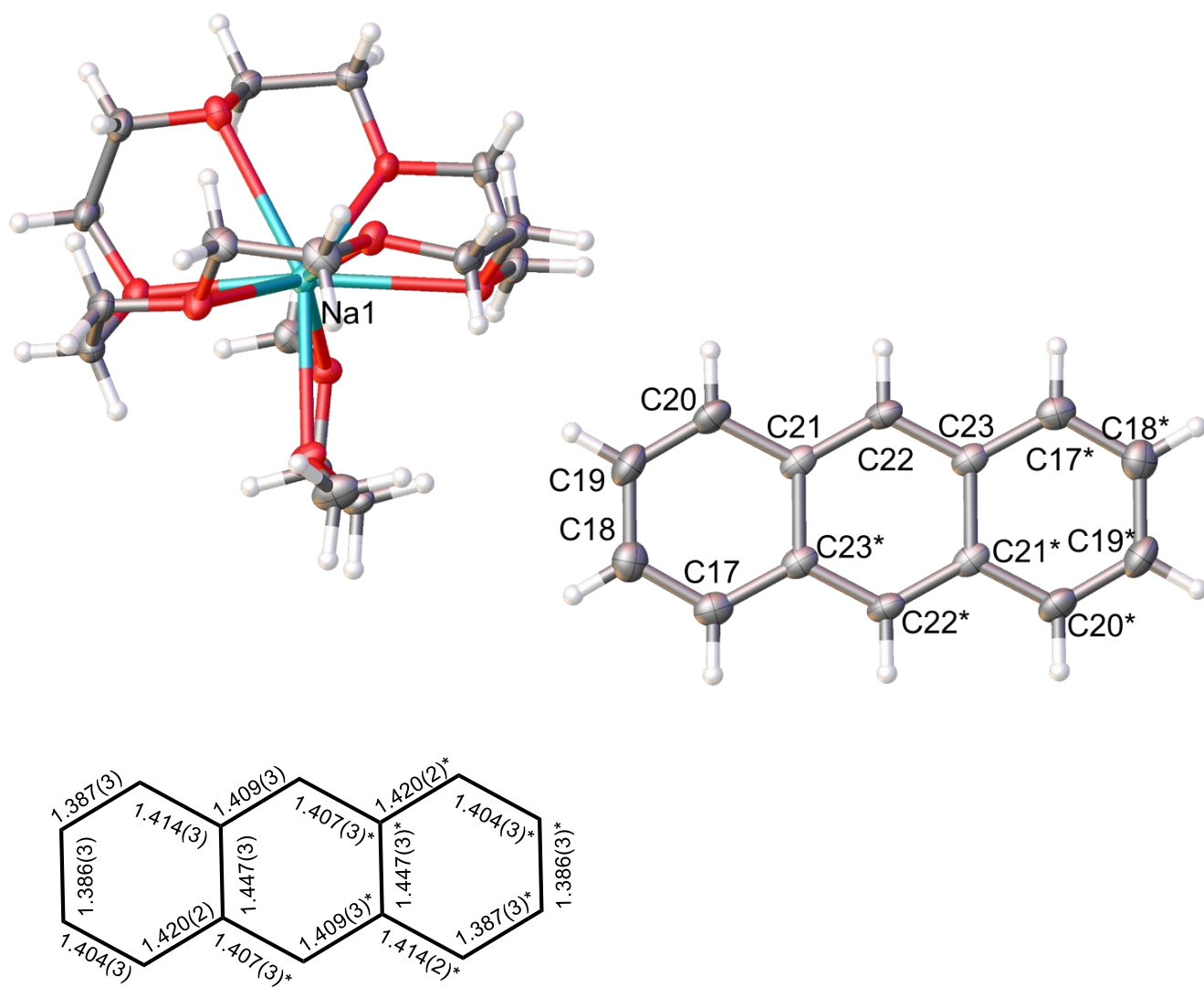


**Figure S5.** Solid-state molecular structure of **8** with 50% probability ellipsoids and respective bond length diagram. Asterisks denote symmetry generated atoms and bond lengths.

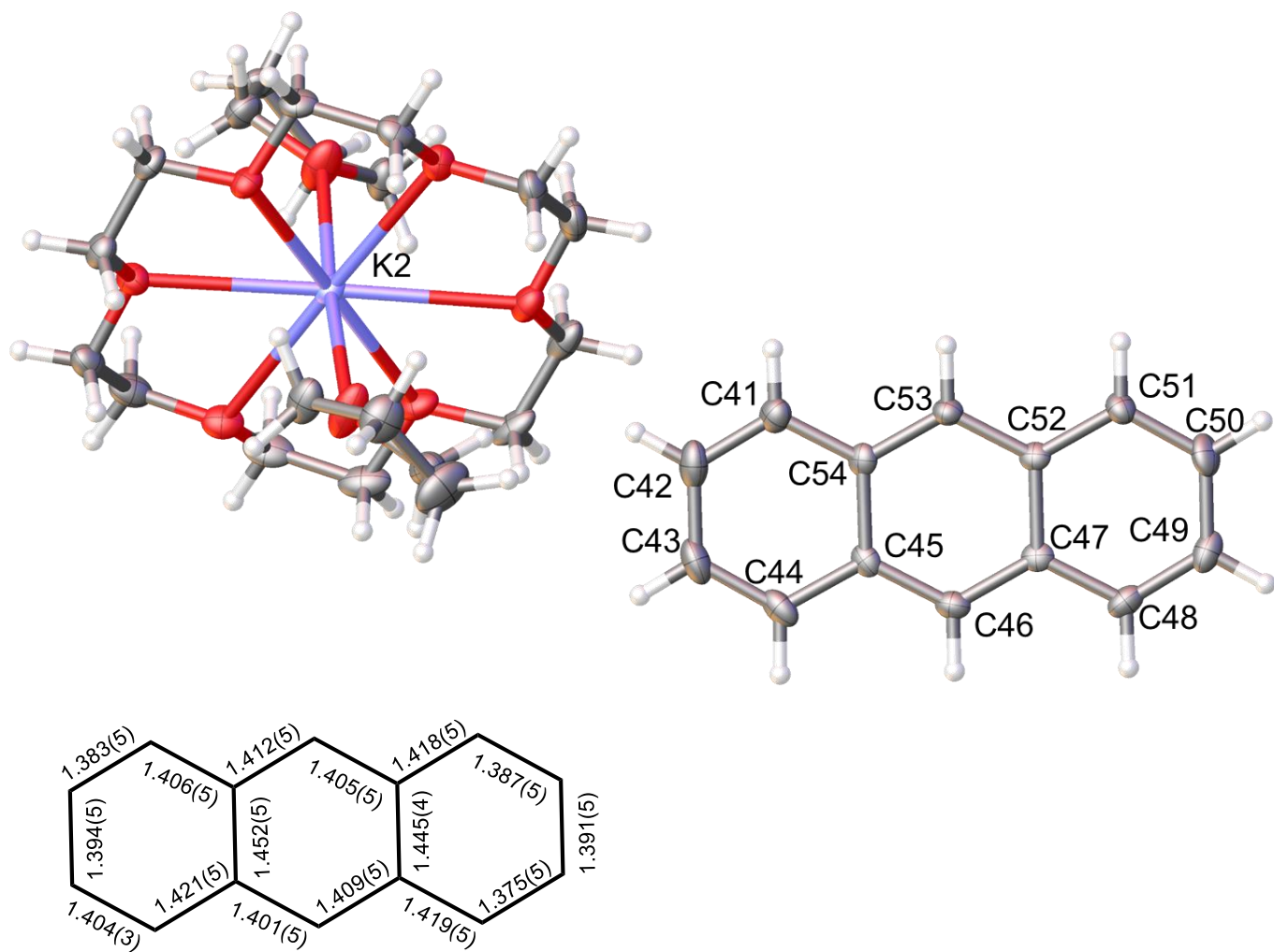


**Figure S6.** Solid-state molecular structure of **9** with 50% probability ellipsoids and respective bond length diagram.

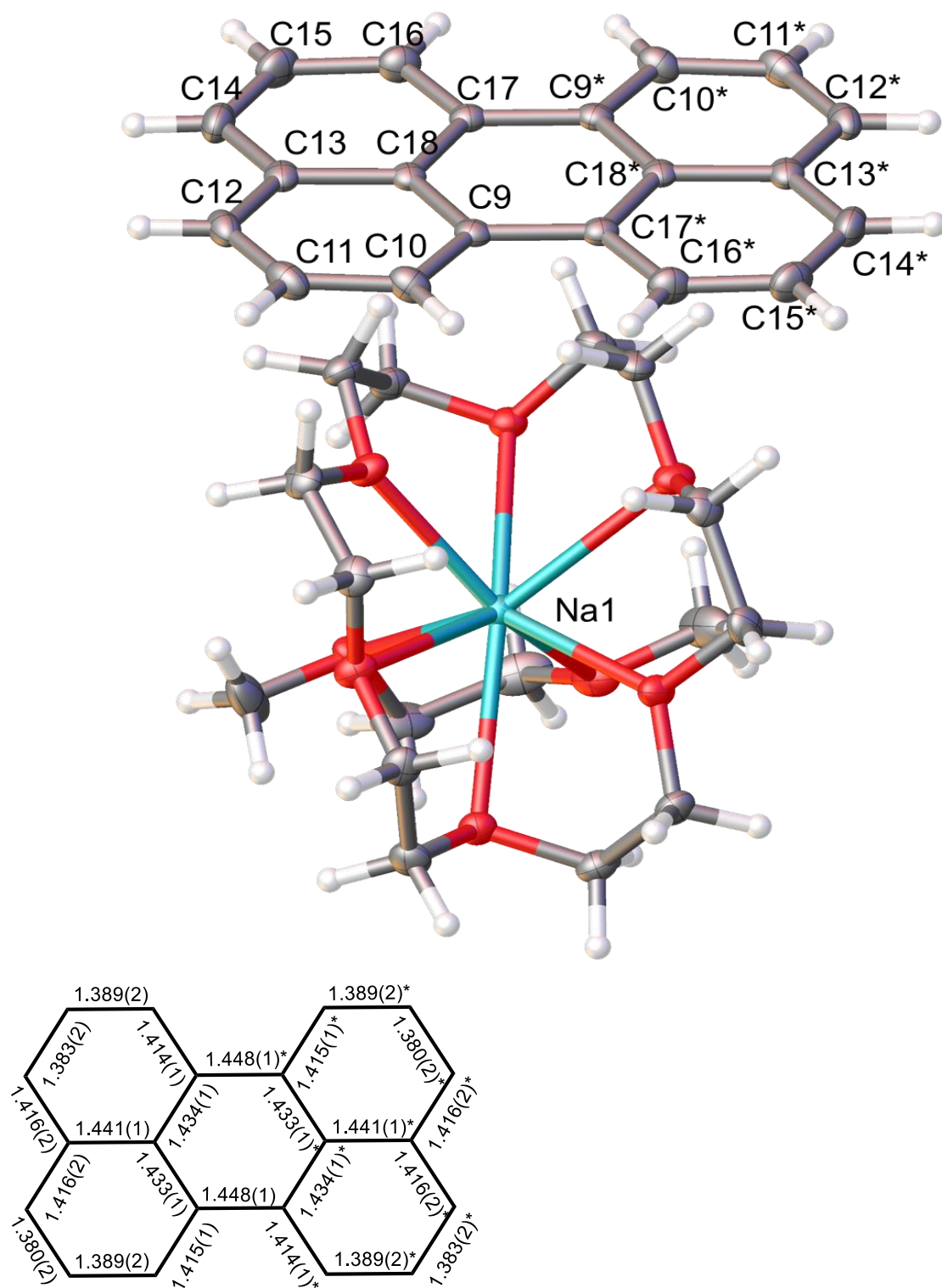


**Figure S7.** Solid-state molecular structure of **11** with 50% probability ellipsoids and respective bond length diagram. Asterisks denote symmetry generated atoms and bond lengths.



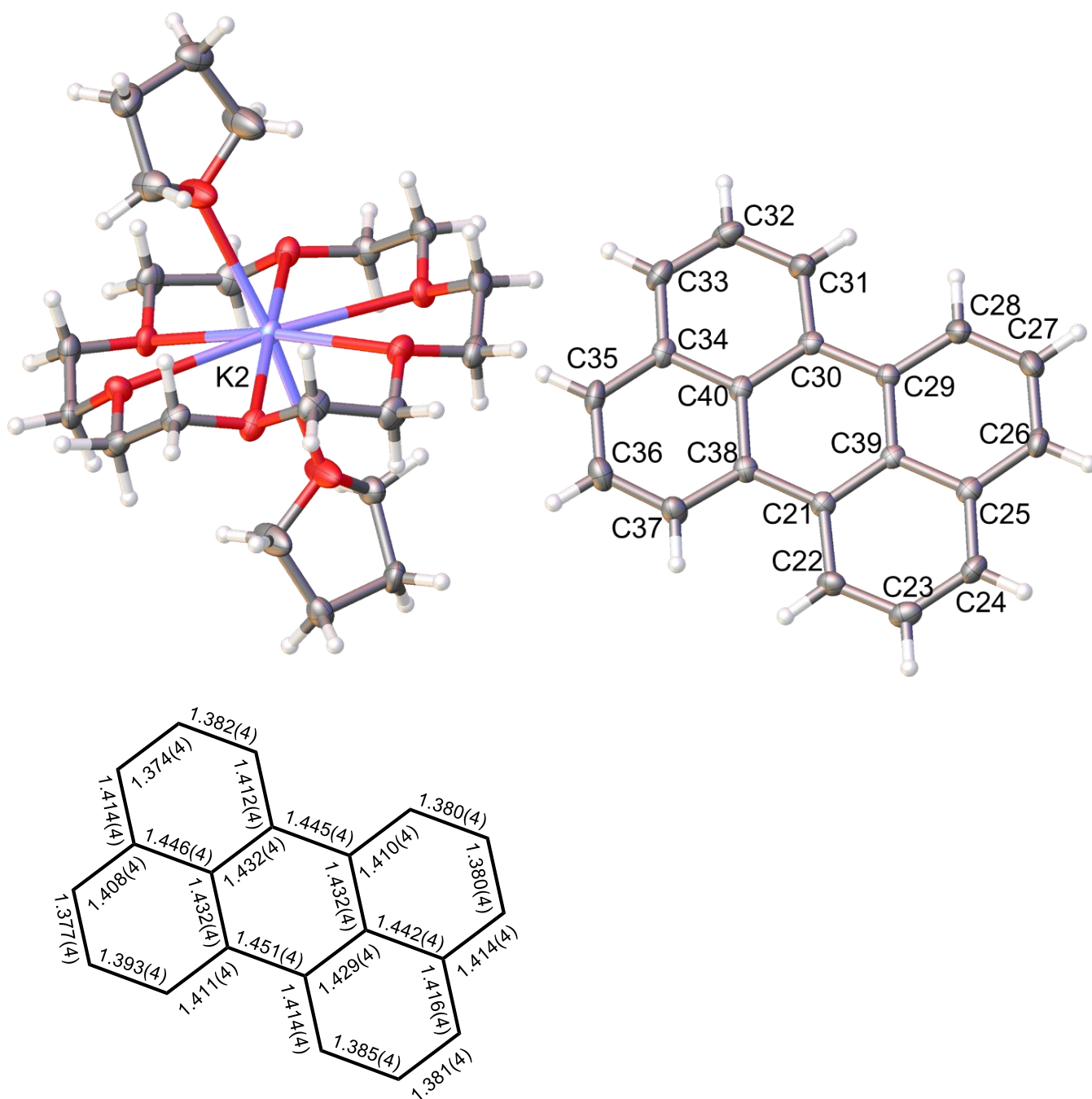


**Figure S8.** Solid-state molecular structure of **12** with 50% probability ellipsoids and respective bond length diagram.

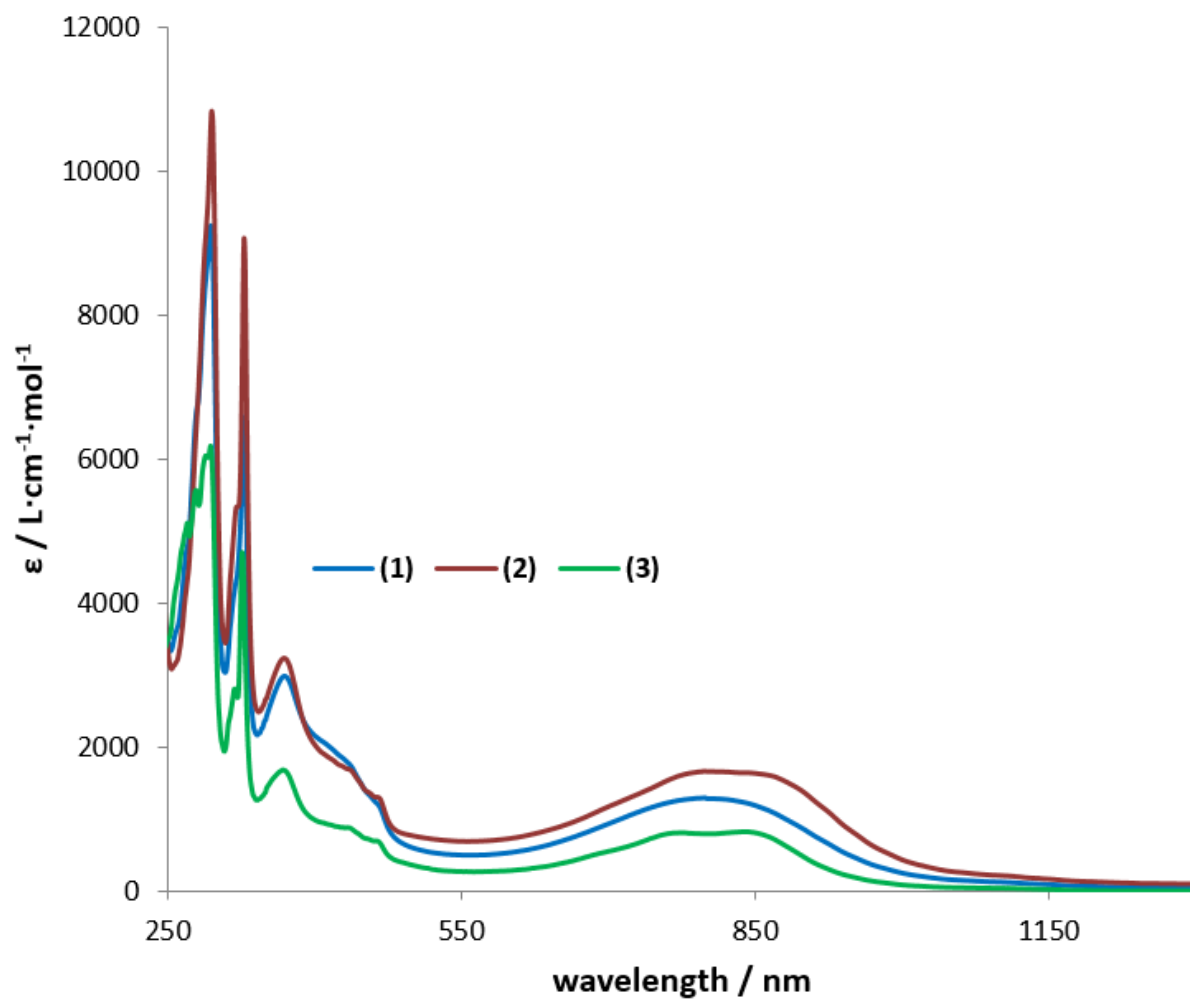


**Figure S9.** Room temperature UV/vis-NIR absorption spectra for **1** (THF, 0.106 mM), **2** (THF, 0.139 mM), and **3** (THF, 0.114 mM).

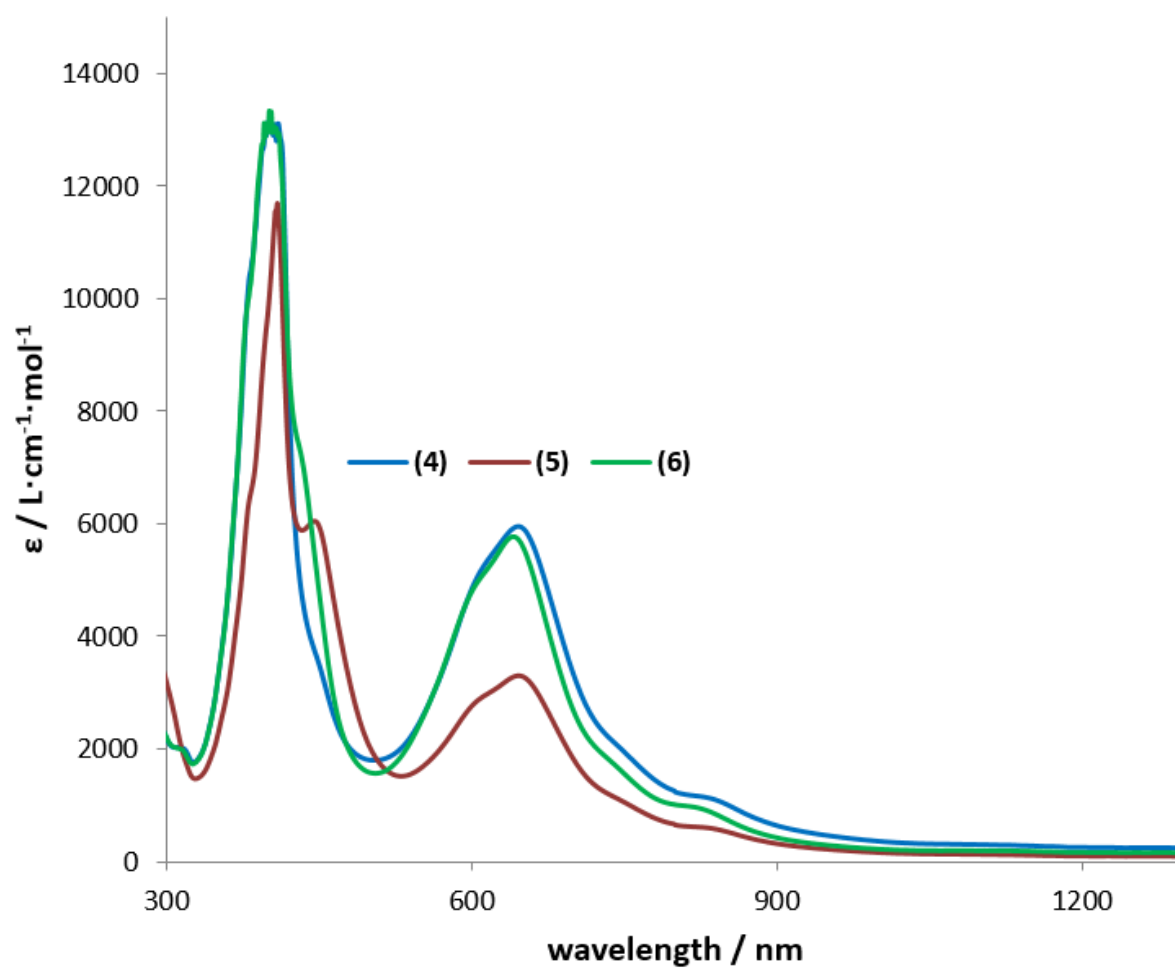


**Figure S10.** Room temperature UV/vis-NIR absorption spectra for **4** (THF, 0.284 mM), **5** (THF, 0.284 mM), and **6** (THF, 0.284 mM).

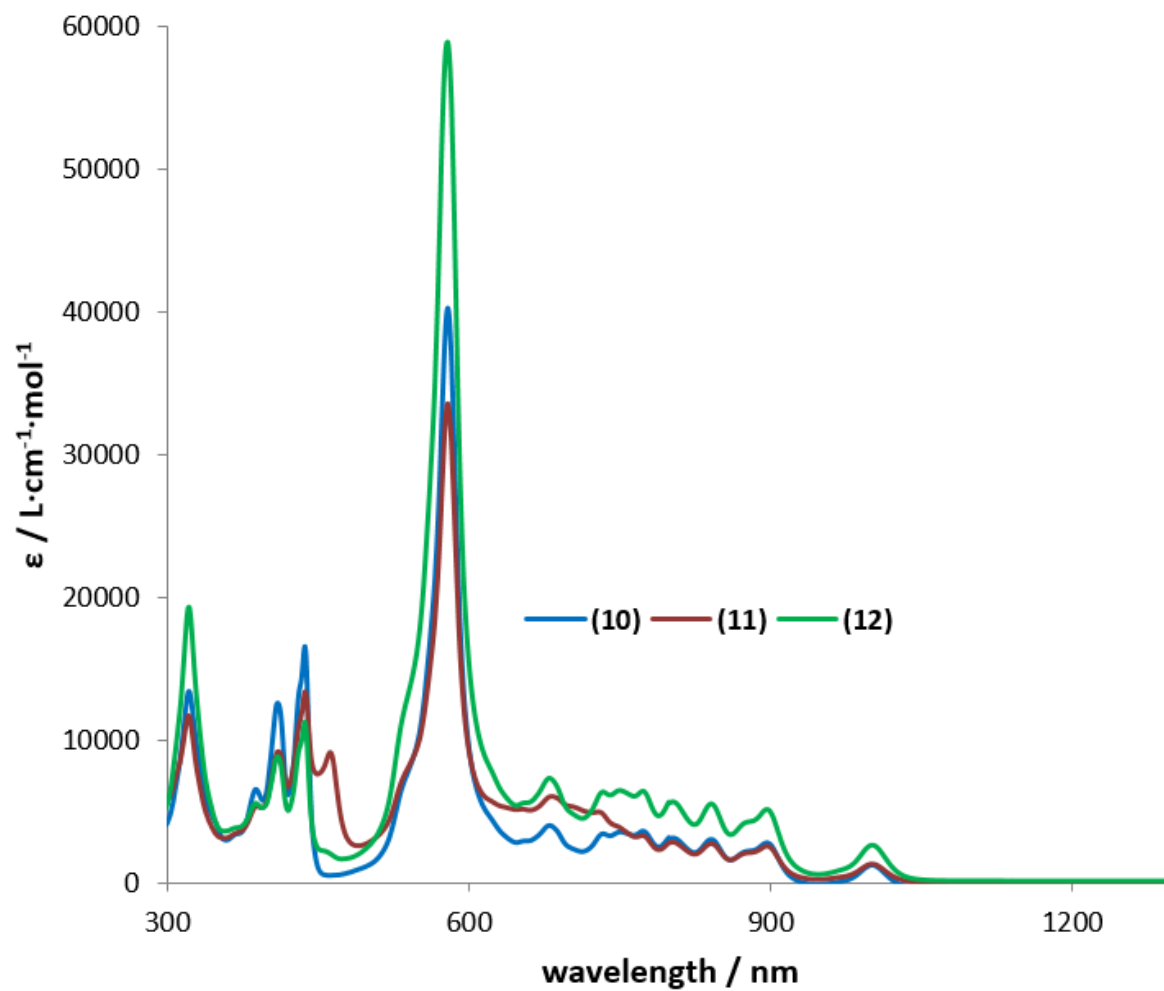


**Figure S11.** Room temperature UV/vis-NIR absorption spectra for **10** (THF, 0.036 mM), **11** (THF, 0.052 mM), and **12** (THF, 0.054 mM).

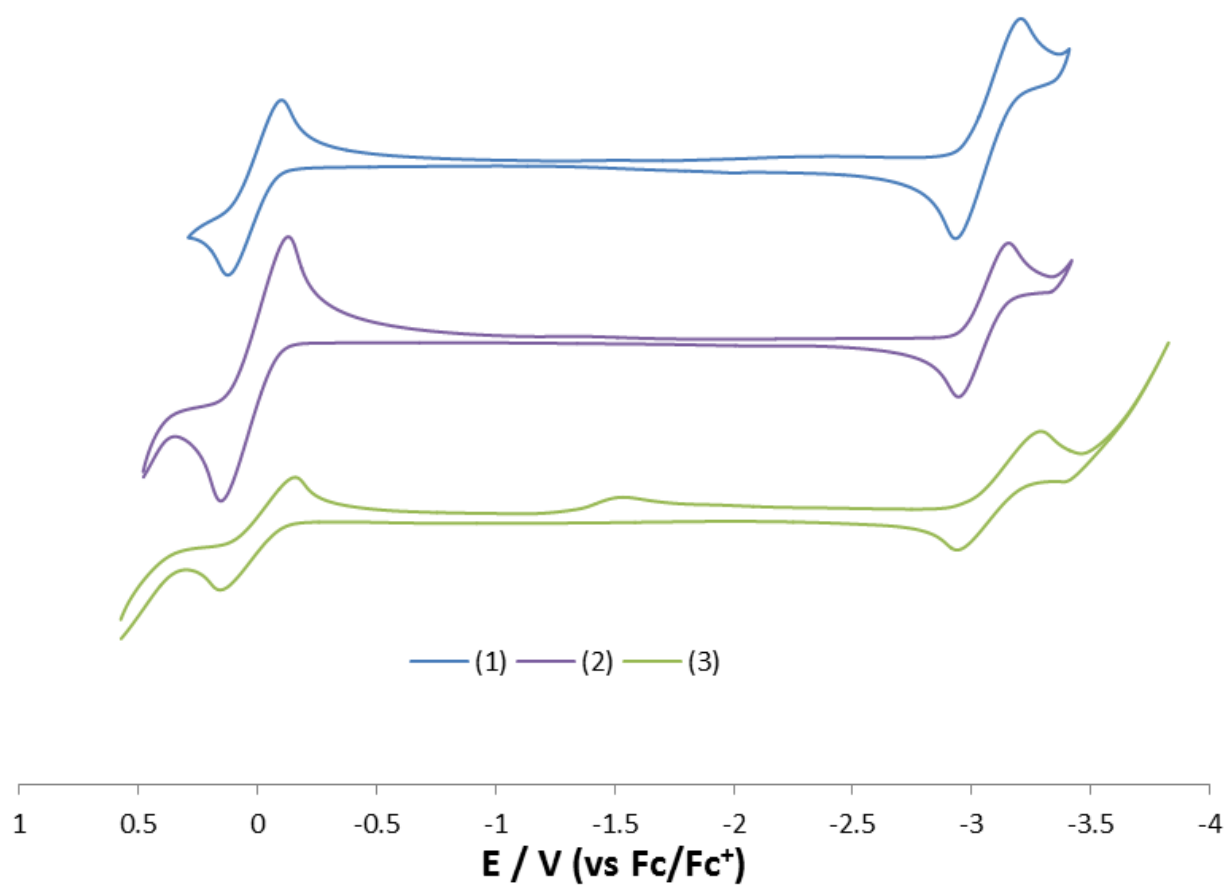


**Figure S12.** Room temperature cyclic voltammogram of **1**, **2** and **3** in DME (50mV/s scan rate) vs.  $[Cp_2Fe]^{0/+}$ . (0.1M  $[NBu_4][PF_6]$  as supporting electrolyte).

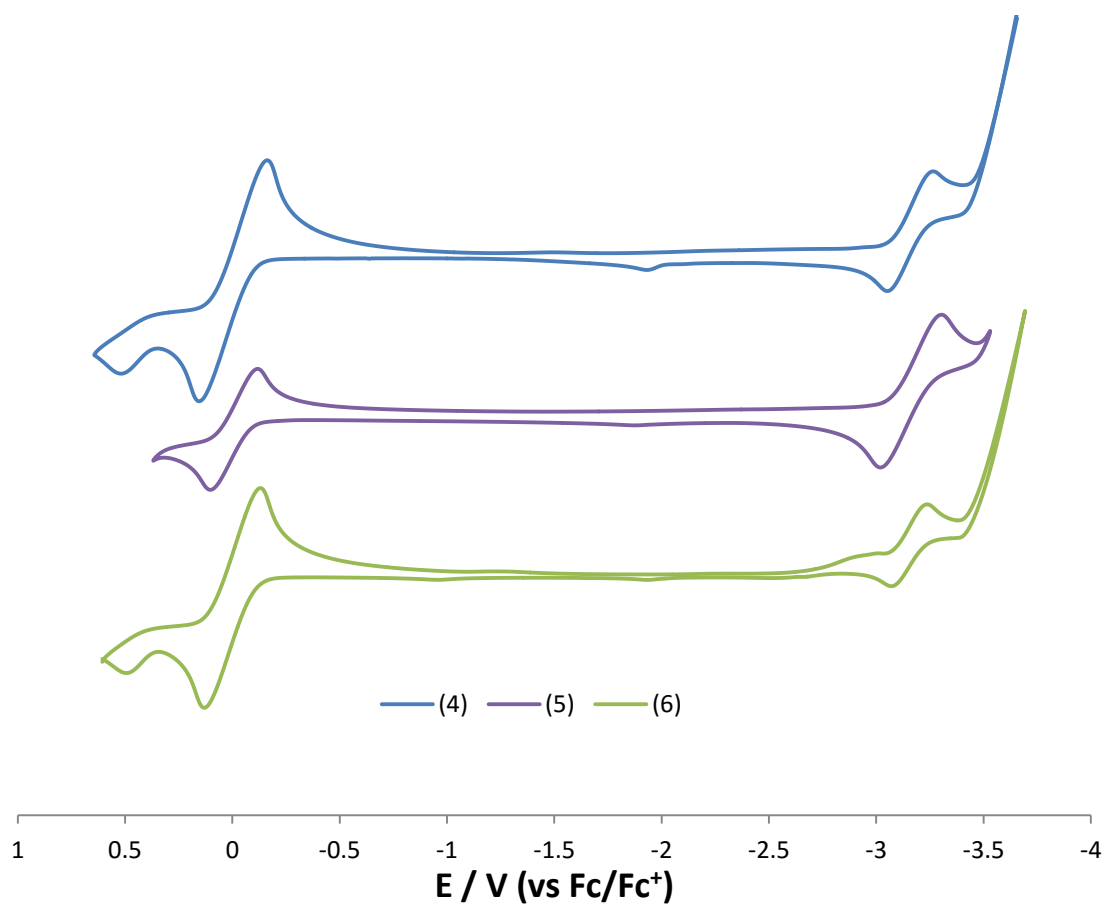


**Figure S13.** Room temperature cyclic voltammogram of **4** (50mV/s scan rate), **5** (200mV/s scan rate) and **6** (50mV/s scan rate) in DME vs  $[Cp_2Fe]^{0/+}$ . (0.1M  $[NBu_4][PF_6]$  as supporting electrolyte).

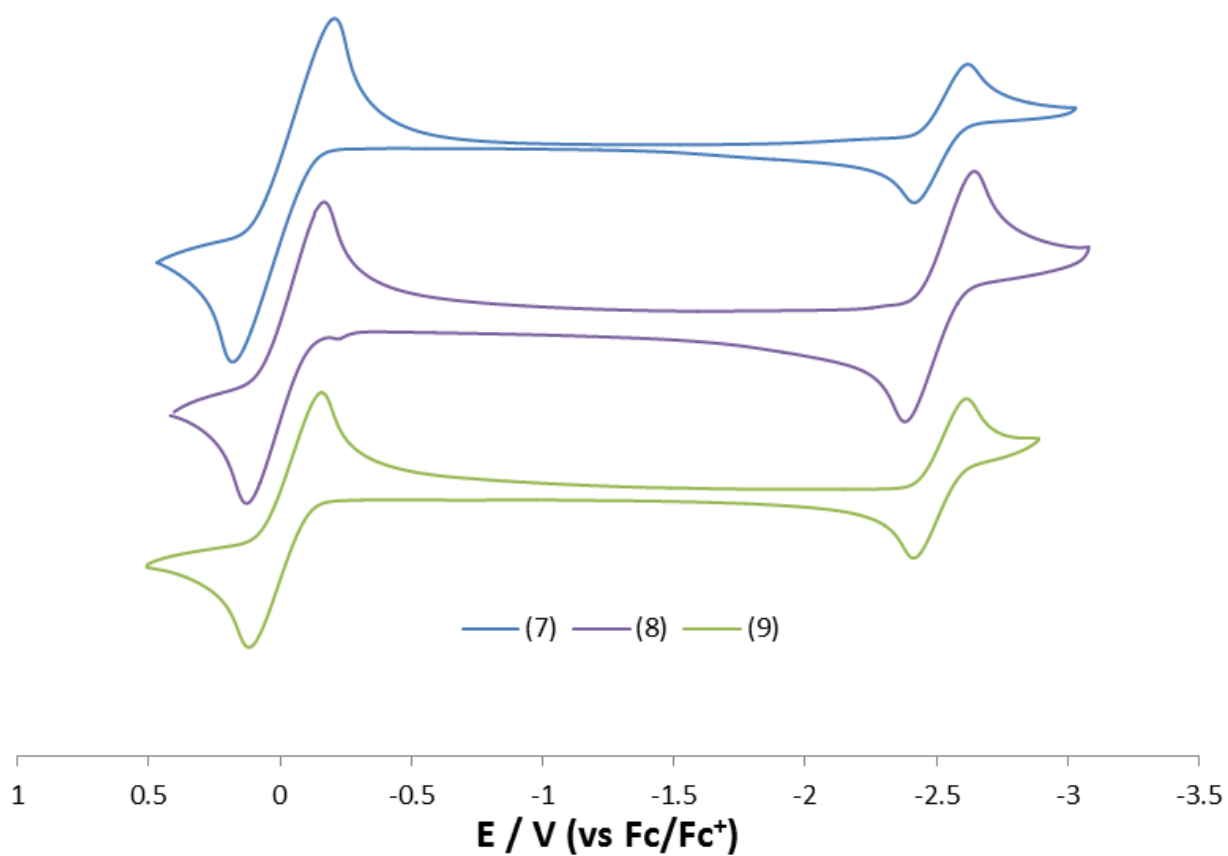


**Figure S14.** Room temperature cyclic voltammogram of **7** (50mV/s scan rate), **8** (300mV/s scan rate) and **9** (200mV/s scan rate) in DME vs  $[Cp_2Fe]^{0/+}$ . (0.1M  $[NBu_4][PF_6]$  as supporting electrolyte).

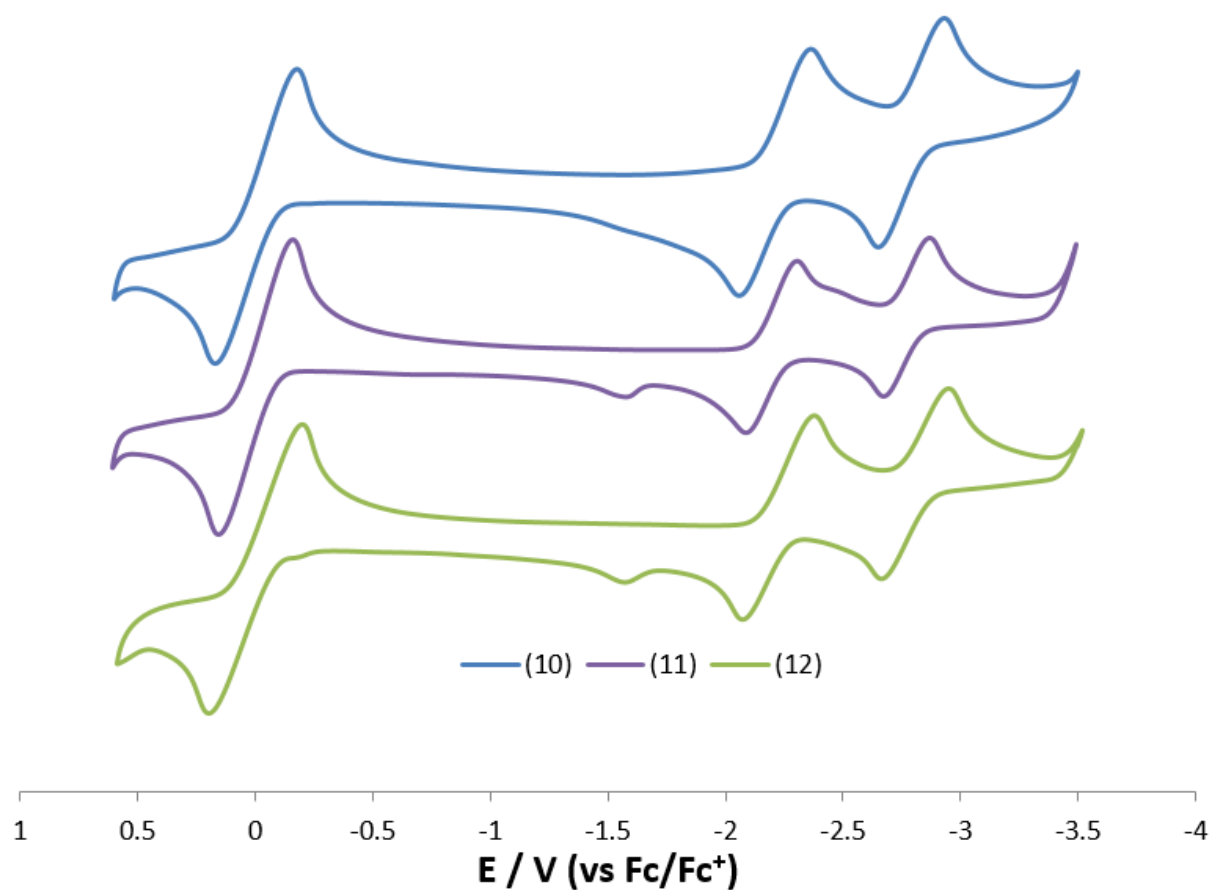


**Figure S15.** Room temperature cyclic voltammogram of **10**, **11** and **12** in DME (200mV/s scan rate) vs  $[Cp_2Fe]^{0/+}$ . (0.1M  $[NBu_4][PF_6]$  as supporting electrolyte).



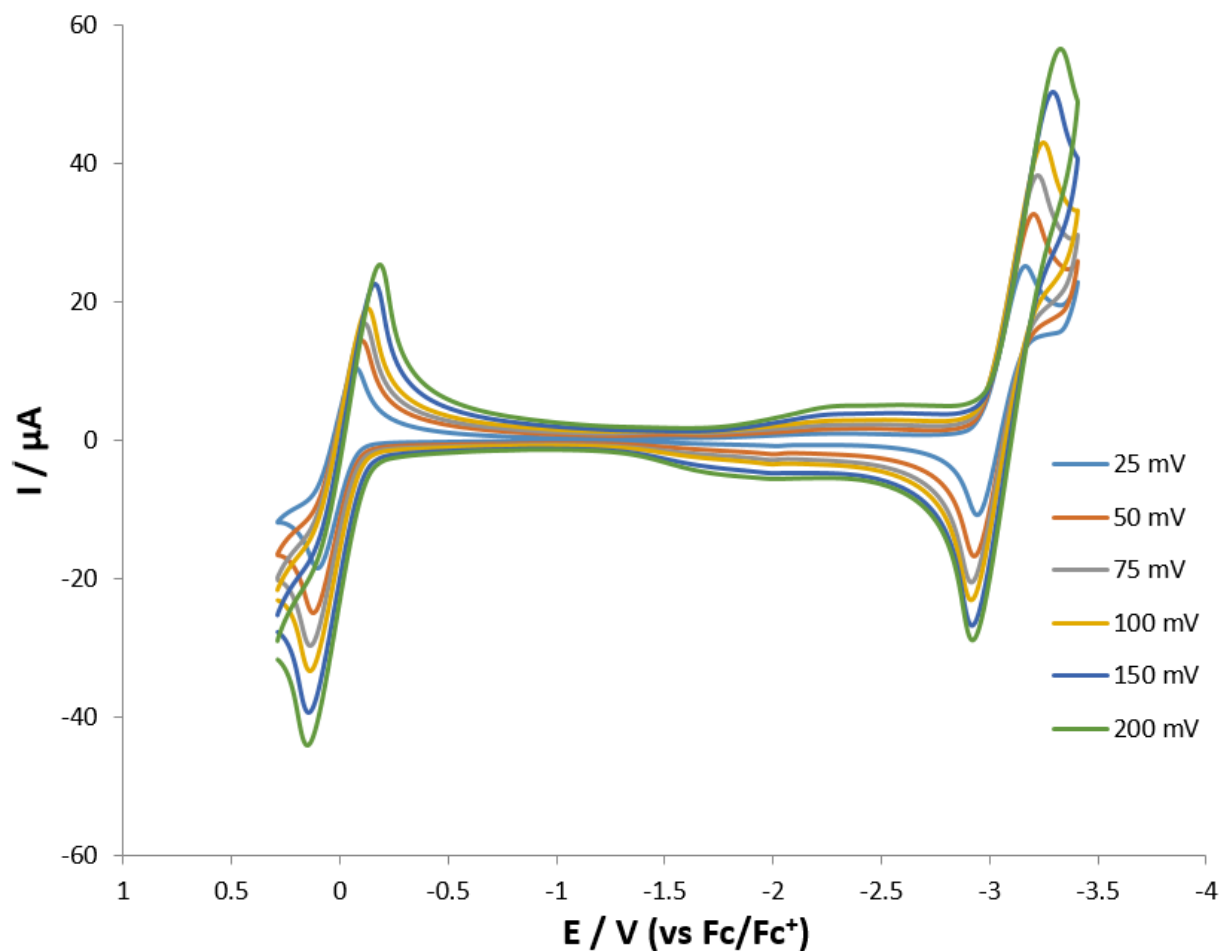


**Figure S16.** Room temperature cyclic voltammogram of **1** in DME (vs  $[\text{Cp}_2\text{Fe}]^{0/+}$ ). (0.1M  $[\text{NBu}_4][\text{PF}_6]$  as supporting electrolyte).

**Table S1.** Electrochemical data for **1** in DME (vs.  $[\text{Cp}_2\text{Fe}]^{0/+}$ ).

Feature (1)	Scan rate, V/s	$E_{p,c}$ , V	$E_{p,a}$ , V	$\Delta E_p$ , V	$i_{p,c}/i_{p,a}$
	0.025	-3.17	-2.945	0.223	-0.90
	0.050	-3.21	-2.932	0.274	-1.01
	0.075	-3.23	-2.919	0.307	-1.08
	0.100	-3.25	-2.918	0.333	-1.13
	0.150	-3.30	-2.921	0.375	-1.42
	0.200	-3.33	-2.924	0.407	-1.92

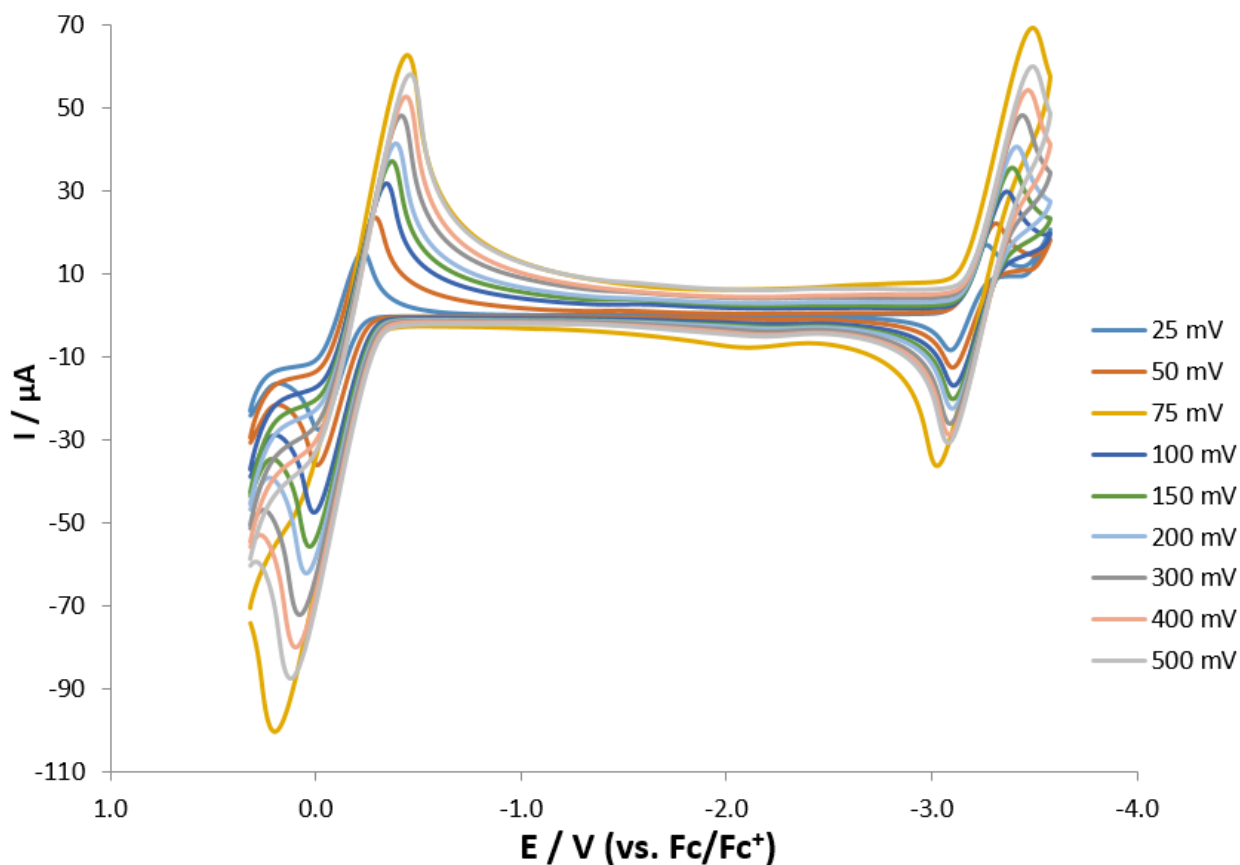


**Figure S17.** Room temperature cyclic voltammogram of **2** in DME (vs  $[\text{Cp}_2\text{Fe}]^{0/+}$ ). (0.1M  $[\text{NBu}_4][\text{PF}_6]$  as supporting electrolyte).

**Table S2.** Electrochemical data for **2** in DME (vs.  $[\text{Cp}_2\text{Fe}]^{0/+}$ ).

Feature ( <b>2</b> )	Scan rate, V/s	$E_{p,c}$ , V	$E_{p,a}$ , V	$\Delta E_p$ , V	$i_{p,c}/i_{p,a}$
	0.025	-3.109	-2.934	0.175	0.95
	0.050	-3.155	-2.944	0.211	0.99
	0.075	-3.335	-2.868	0.467	2.08
	0.100	-3.208	-2.95	0.258	1.10
	0.150	-3.235	-2.946	0.289	1.15
	0.200	-3.257	-2.942	0.315	1.20
	0.300	-3.284	-2.931	0.353	1.33
	0.400	-3.312	-2.928	0.384	1.57
	0.500	-3.334	-2.922	0.412	1.96

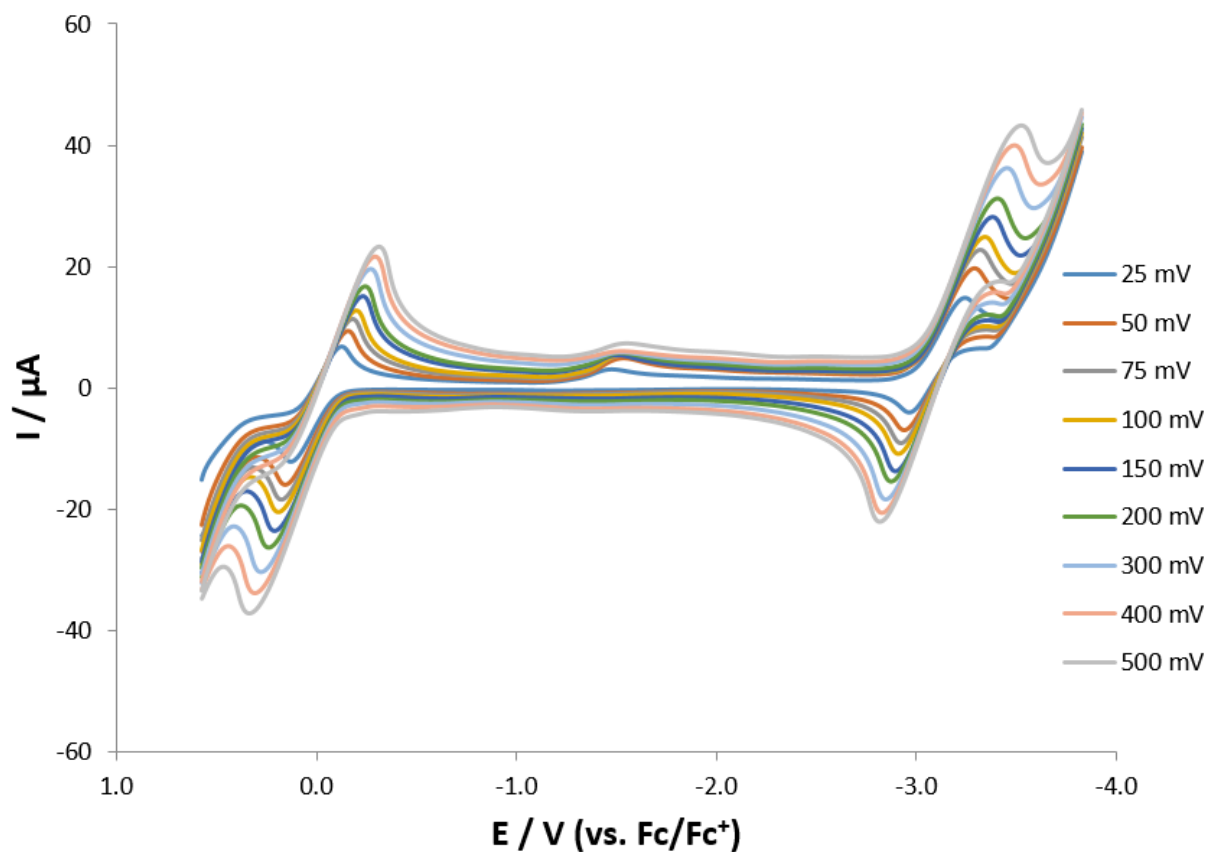


**Figure S18.** Room temperature cyclic voltammogram of **3** in DME (vs  $[\text{Cp}_2\text{Fe}]^{0/+}$ ). (0.1M  $[\text{NBu}_4][\text{PF}_6]$  as supporting electrolyte).

**Table S3.** Electrochemical data for **3** in DME (vs.  $[\text{Cp}_2\text{Fe}]^{0/+}$ ).

Feature (3)	Scan rate, V/s	$E_{p,c}$ , V	$E_{p,a}$ , V	$\Delta E_p$ , V	$i_{p,c}/i_{p,a}$
	0.025	-3.246	-2.967	0.279	0.94
	0.050	-3.294	-2.942	0.352	0.85
	0.075	-3.323	-2.925	0.398	0.82
	0.100	-3.246	-2.913	0.333	0.83
	0.150	-3.384	-2.898	0.486	0.85
	0.200	-3.409	-2.877	0.532	0.81
	0.300	-3.457	-2.85	0.607	0.84
	0.400	-3.493	-2.831	0.662	0.81
	0.500	-3.53	-2.821	0.709	1.01

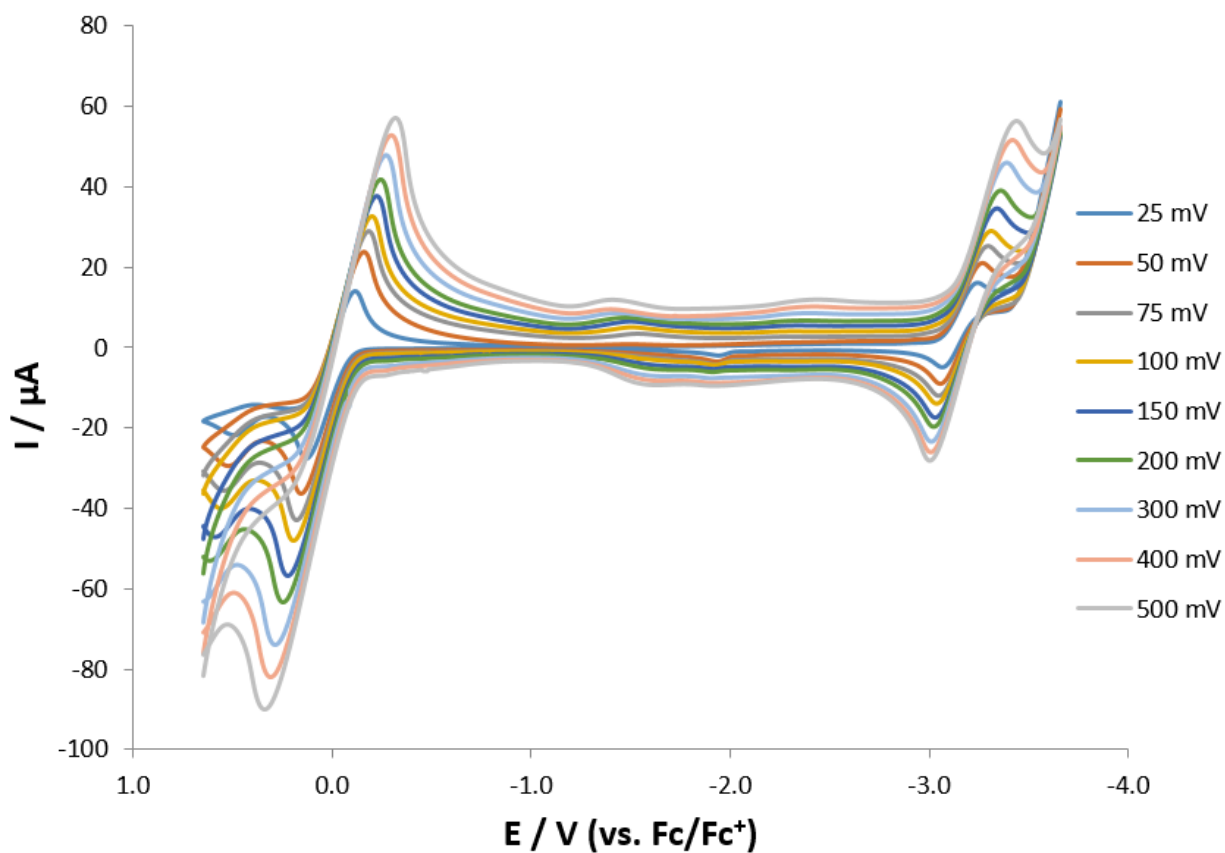


**Figure S19.** Room temperature cyclic voltammogram of **4** in DME (vs  $[\text{Cp}_2\text{Fe}]^{0/+}$ ). (0.1M  $[\text{NBu}_4][\text{PF}_6]$  as supporting electrolyte).

**Table S4** Electrochemical data for **4** in DME (vs.  $[\text{Cp}_2\text{Fe}]^{0/+}$ ).

Feature ( <b>4</b> )	Scan rate, V/s	$E_{p,c}$ , V	$E_{p,a}$ , V	$\Delta E_p$ , V	$i_{p,c}/i_{p,a}$
	0.025	-3.245	-3.067	0.178	1.09
	0.050	-3.269	-3.057	0.212	1.15
	0.075	-3.297	-3.049	0.248	1.05
	0.100	-3.313	-3.039	0.274	1.02
	0.150	-3.342	-3.032	0.31	1.08
	0.200	-3.36	-3.024	0.336	1.14
	0.300	-3.391	-3.012	0.379	1.20
	0.400	-3.42	-3.009	0.411	1.26
	0.500	-3.44	-3.005	0.435	1.28

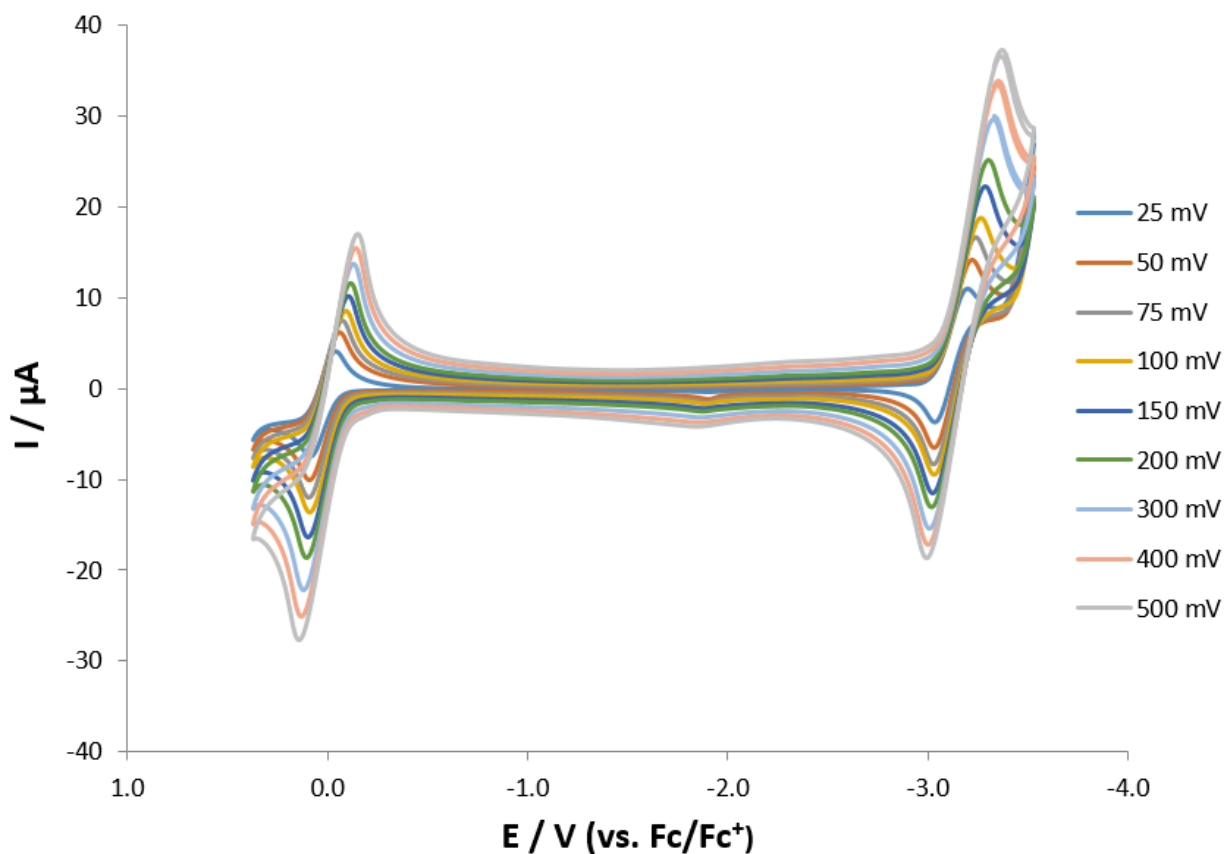


**Figure S20.** Room temperature cyclic voltammogram of **5** in DME (vs  $[\text{Cp}_2\text{Fe}]^{0/+}$ ). (0.1M  $[\text{NBu}_4][\text{PF}_6]$  as supporting electrolyte).

**Table S5** Electrochemical data for **5** in DME (vs.  $[\text{Cp}_2\text{Fe}]^{0/+}$ ).

Feature ( <b>5</b> )	Scan rate, V/s	$E_{p,c}$ , V	$E_{p,a}$ , V	$\Delta E_p$ , V	$i_{p,c}/i_{p,a}$
	0.025	-3.199	-3.035	0.164	0.69
	0.050	-3.221	-3.031	0.19	0.77
	0.075	-3.239	-3.028	0.211	0.85
	0.100	-3.265	-3.031	0.234	0.99
	0.150	-3.287	-3.024	0.263	1.19
	0.200	-3.303	-3.018	0.285	1.33
	0.300	-3.328	-3.008	0.32	1.18
	0.400	-3.348	-3.001	0.347	0.98
	0.500	-3.366	-2.994	0.372	1.04

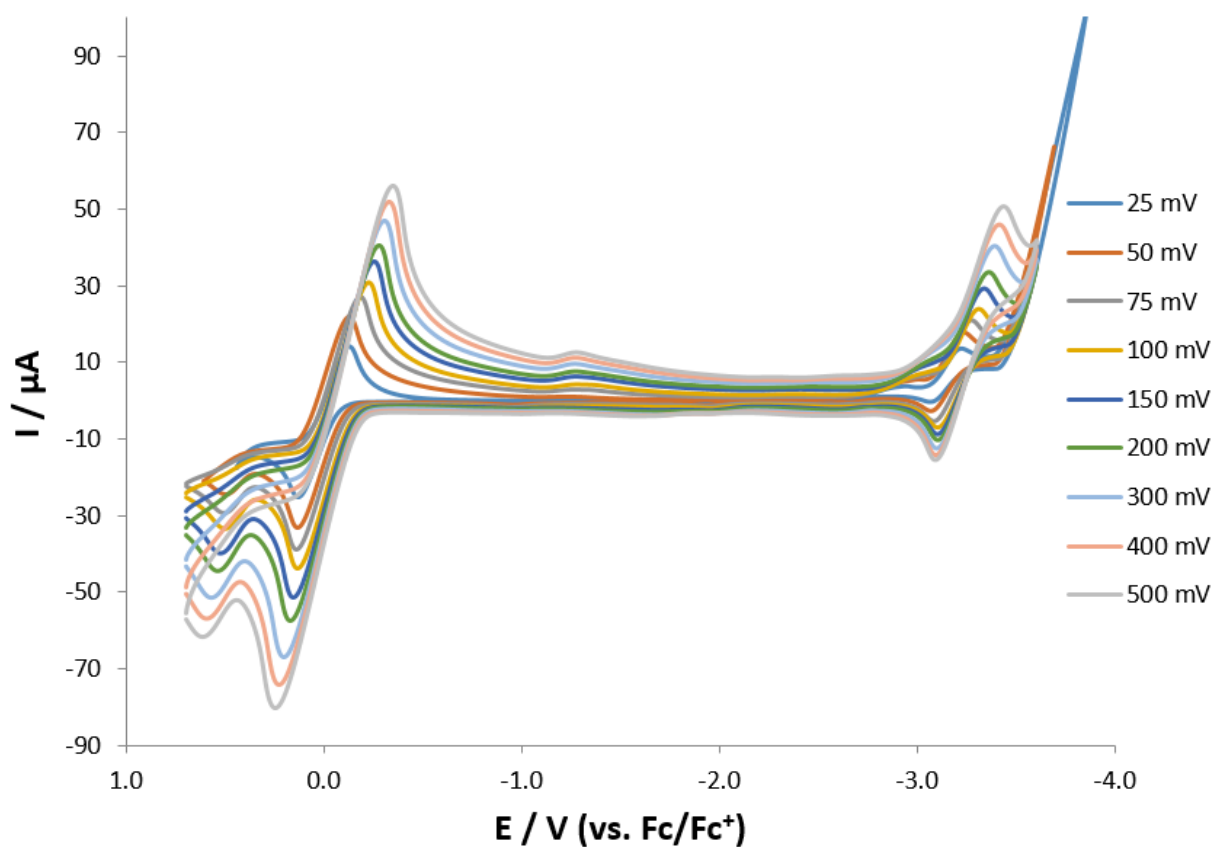


**Figure S21.** Room temperature cyclic voltammogram of **6** in DME (vs  $[\text{Cp}_2\text{Fe}]^{0/+}$ ). (0.1M  $[\text{NBu}_4][\text{PF}_6]$  as supporting electrolyte).

**Table S6** Electrochemical data for **6** in DME (vs.  $[\text{Cp}_2\text{Fe}]^{0/+}$ ).

Feature ( <b>6</b> )	Scan rate, V/s	$E_{p,c}$ , V	$E_{p,a}$ , V	$\Delta E_p$ , V	$i_{p,c}/i_{p,a}$
	0.025	-2.973	-2.814	0.159	1.34
	0.050	-3.153	-2.987	0.166	1.11
	0.075	-3.28	-3.09	0.19	0.85
	0.100	-3.318	-3.109	0.209	0.82
	0.150	-3.344	-3.108	0.236	0.78
	0.200	-3.369	-3.11	0.259	0.72
	0.300	-3.398	-3.104	0.294	0.69
	0.400	-3.421	-3.1	0.321	0.75
	0.500	-3.443	-3.098	0.345	0.87

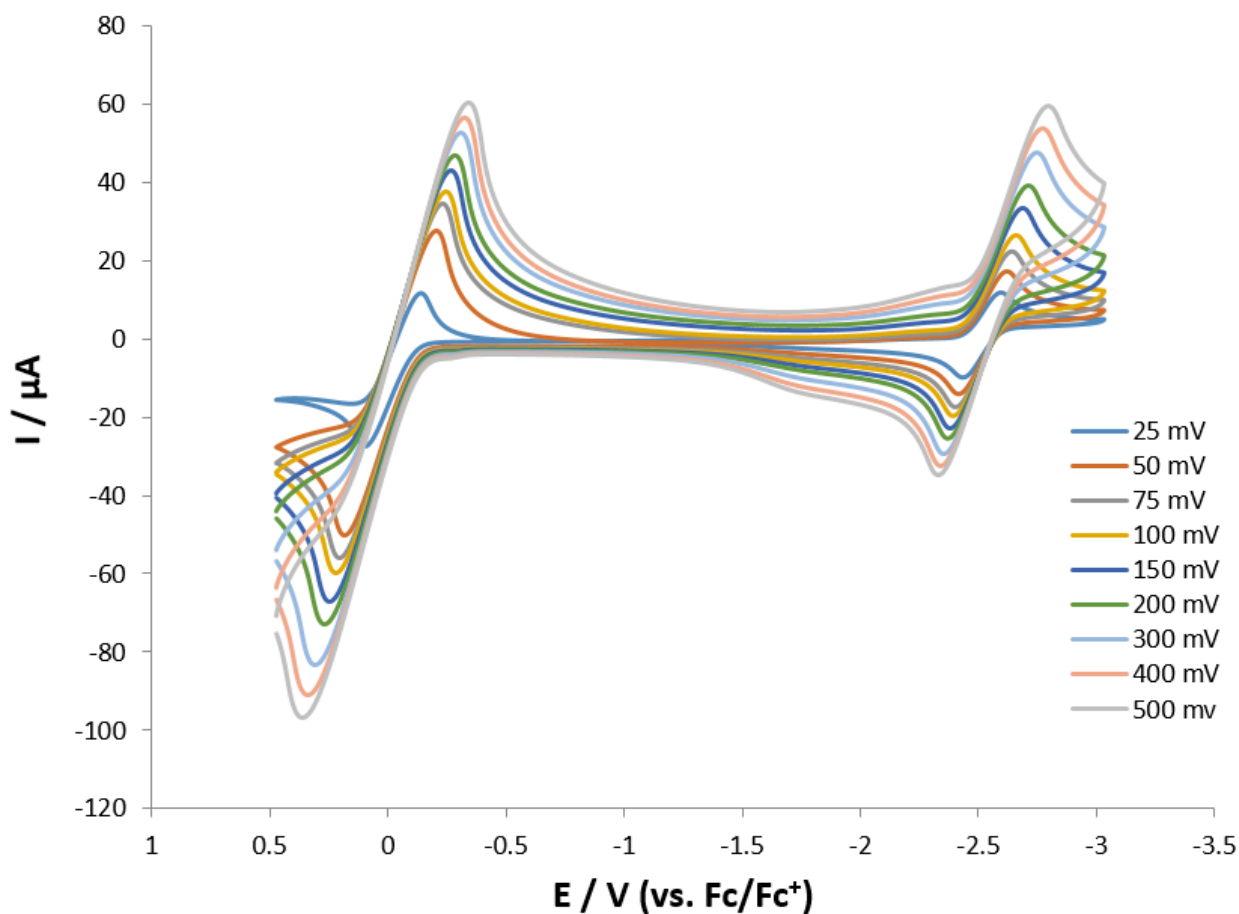


**Figure S22.** Room temperature cyclic voltammogram of **7** in DME (vs  $[\text{Cp}_2\text{Fe}]^{0/+}$ ). (0.1M  $[\text{NBu}_4][\text{PF}_6]$  as supporting electrolyte).

**Table S7** Electrochemical data for **7** in DME (vs.  $[\text{Cp}_2\text{Fe}]^{0/+}$ ).

Feature ( <b>7</b> )	Scan rate, V/s	$E_{p,c}$ , V	$E_{p,a}$ , V	$\Delta E_p$ , V	$i_{p,c}/i_{p,a}$
	0.025	-2.584	-2.423	0.161	0.94
	0.050	-2.609	-2.404	0.205	0.94
	0.075	-2.63	-2.391	0.239	0.96
	0.100	-2.648	-2.381	0.267	0.97
	0.150	-2.676	-2.368	0.308	0.99
	0.200	-2.7	-2.359	0.341	0.99
	0.300	-2.735	-2.342	0.393	1.00
	0.400	-2.76	-2.328	0.432	1.01
	0.500	-2.784	-2.319	0.465	1.02

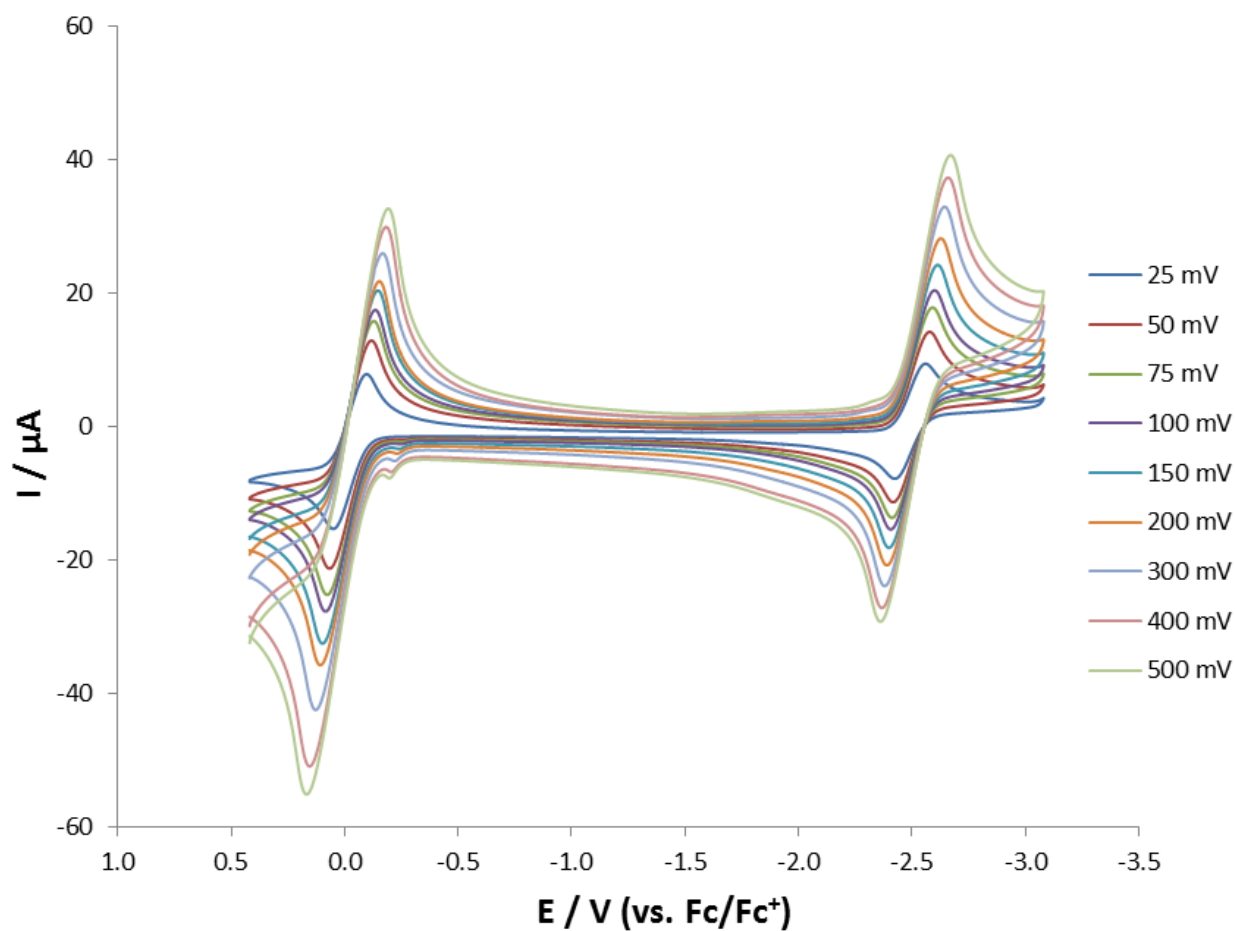


**Figure S23.** Room temperature cyclic voltammogram of **8** in DME (vs  $[\text{Cp}_2\text{Fe}]^{0/+}$ ). (0.1M  $[\text{NBu}_4][\text{PF}_6]$  as supporting electrolyte).

**Table S8.** Electrochemical data for **8** in DME (vs.  $[\text{Cp}_2\text{Fe}]^{0/+}$ ).

Feature ( <b>8</b> )	Scan rate, V/s	$E_{p,c}$ , V	$E_{p,a}$ , V	$\Delta E_p$ , V	$i_{p,c}/i_{p,a}$
	0.025	-2.53	-2.394	0.136	1.08
	0.050	-2.548	-2.386	0.162	1.03
	0.075	-2.56	-2.381	0.179	1.03
	0.100	-2.569	-2.376	0.193	1.02
	0.150	-2.583	-2.368	0.215	1.04
	0.200	-2.597	-2.359	0.238	1.05
	0.300	-2.614	-2.349	0.265	1.38
	0.400	-2.629	-2.337	0.292	1.06
	0.500	-2.64	-2.33	0.31	1.38



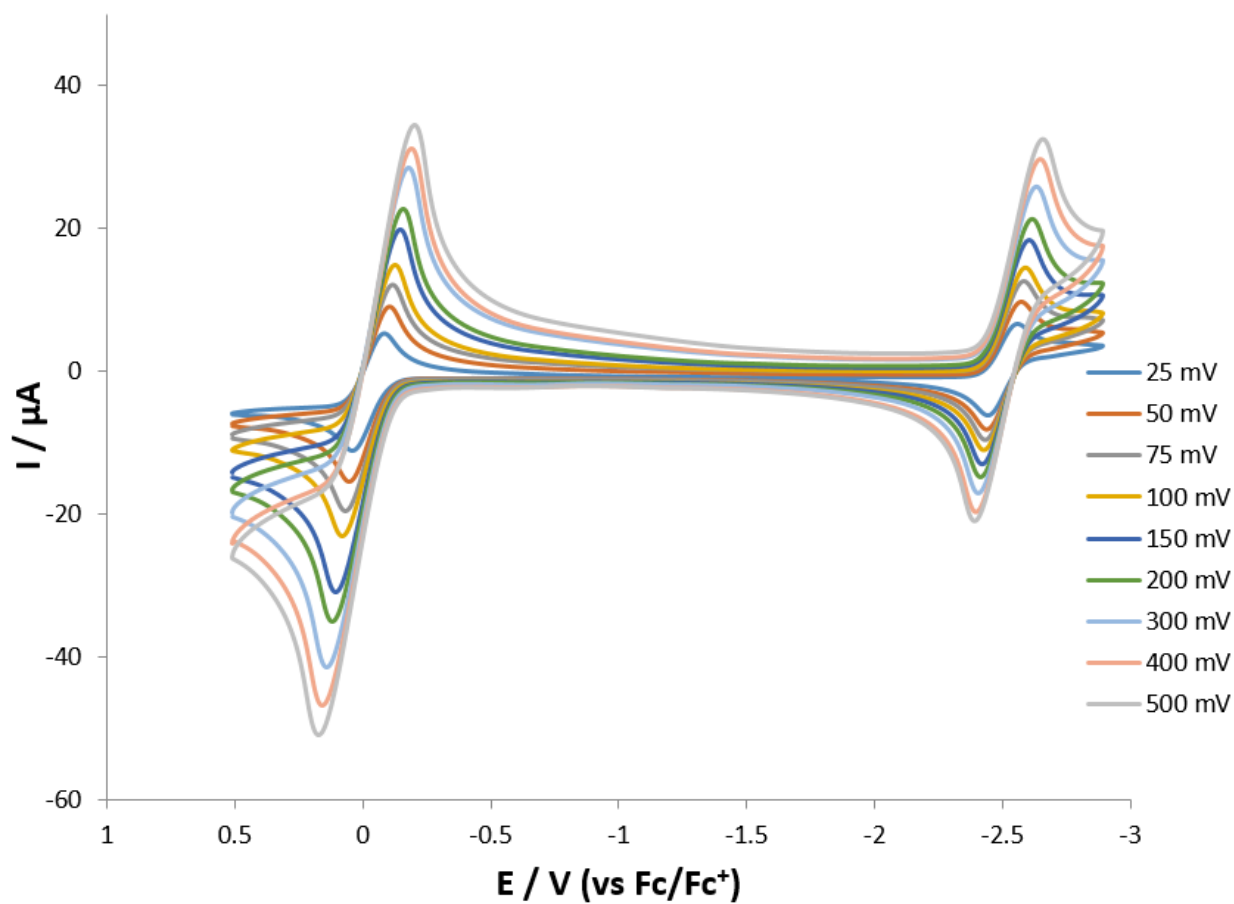


**Figure S24.** Room temperature cyclic voltammogram of **9** in DME (vs  $[\text{Cp}_2\text{Fe}]^{0/+}$ ). (0.1M  $[\text{NBu}_4][\text{PF}_6]$  as supporting electrolyte).

**Table S9.** Electrochemical data for **9** in DME (vs.  $[\text{Cp}_2\text{Fe}]^{0/+}$ ).

Feature ( <b>9</b> )	Scan rate, V/s	$E_{p,c}$ , V	$E_{p,a}$ , V	$\Delta E_p$ , V	$i_{p,c}/i_{p,a}$
	0.025	-2.537	-2.421	0.116	1.02
	0.050	-2.551	-2.416	0.135	1.05
	0.075	-2.561	-2.41	0.151	1.07
	0.100	-2.568	-2.405	0.163	1.08
	0.150	-2.582	-2.398	0.184	1.08
	0.200	-2.594	-2.392	0.202	1.08
	0.300	-2.611	-2.383	0.228	1.09
	0.400	-2.626	-2.374	0.252	1.10
	0.500	-2.636	-2.369	0.267	1.10

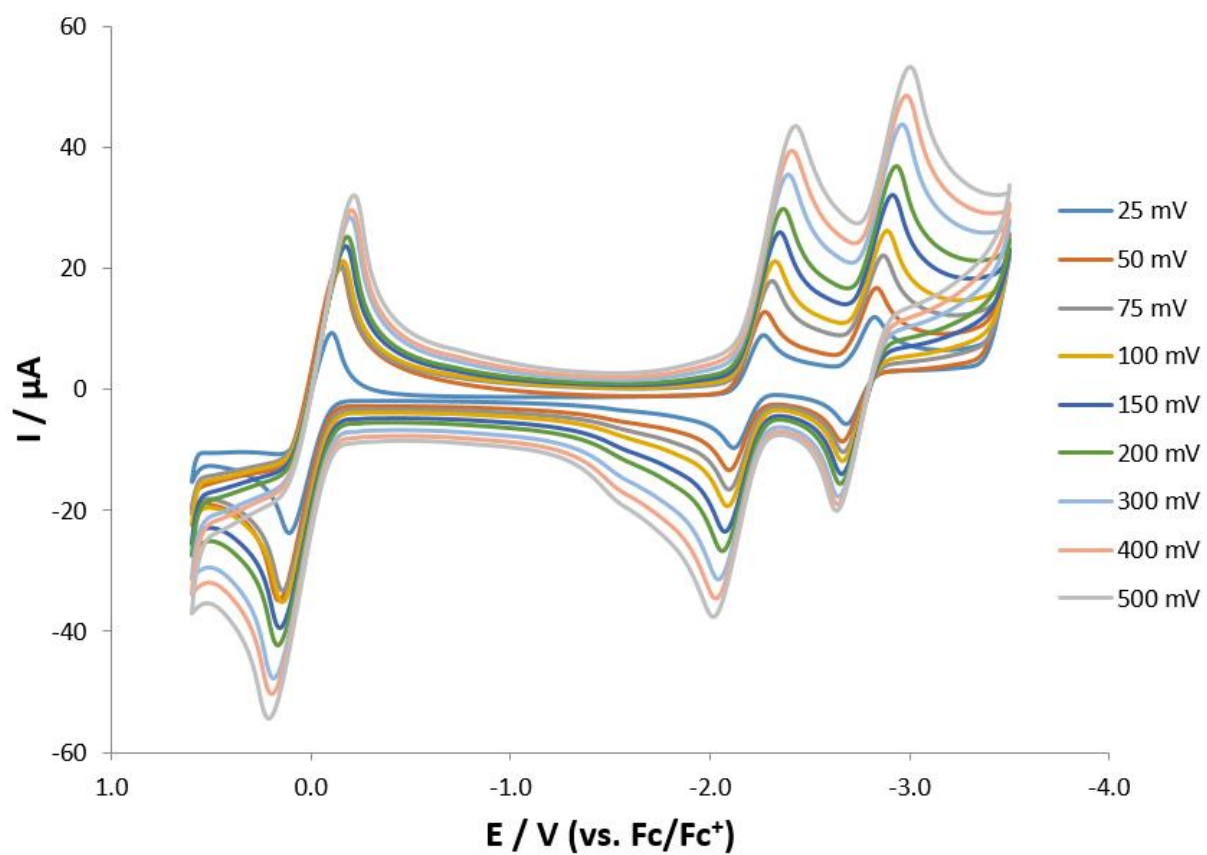


**Figure S25.** Room temperature cyclic voltammogram of **10** in DME (vs [Cp<sub>2</sub>Fe]<sup>0/+</sup>). (0.1M [NBu<sub>4</sub>][PF<sub>6</sub>] as supporting electrolyte).

**Table S10.** Electrochemical data for **10** in DME (vs. [Cp<sub>2</sub>Fe]<sup>0/+</sup>).

Feature 1 (10)	Scan rate, V/s	E <sub>p,c</sub> , V	E <sub>p,a</sub> , V	ΔE <sub>p</sub> , V	<i>i</i> <sub>p,c</sub> / <i>i</i> <sub>p,a</sub>
	0.025	-2.801	-2.657	0.144	1.03
	0.050	-2.838	-2.66	0.178	1.00
	0.075	-2.868	-2.666	0.202	0.97
	0.100	-2.886	-2.662	0.224	0.98
	0.150	-2.914	-2.658	0.256	0.99
	0.200	-2.933	-2.651	0.282	0.96
	0.300	-2.962	-2.642	0.32	0.94
	0.400	-2.982	-2.637	0.345	0.93
	0.500	-3.001	-2.632	0.369	0.92
Feature 2 (10)	Scan rate, V/s	E <sub>p,c</sub> , V	E <sub>p,a</sub> , V	ΔE <sub>p</sub> , V	<i>i</i> <sub>p,c</sub> / <i>i</i> <sub>p,a</sub>
	0.025	-2.244	-2.094	0.15	1.10
	0.050	-2.275	-2.094	0.181	1.18
	0.075	-2.309	-2.093	0.216	1.14
	0.100	-2.325	-2.085	0.24	0.72
	0.150	-2.348	-2.072	0.276	1.02
	0.200	-2.365	-2.059	0.306	1.05
	0.300	-2.391	-2.04	0.351	1.05
	0.400	-2.409	-2.027	0.382	0.97
	0.500	-2.427	-2.014	0.413	0.94

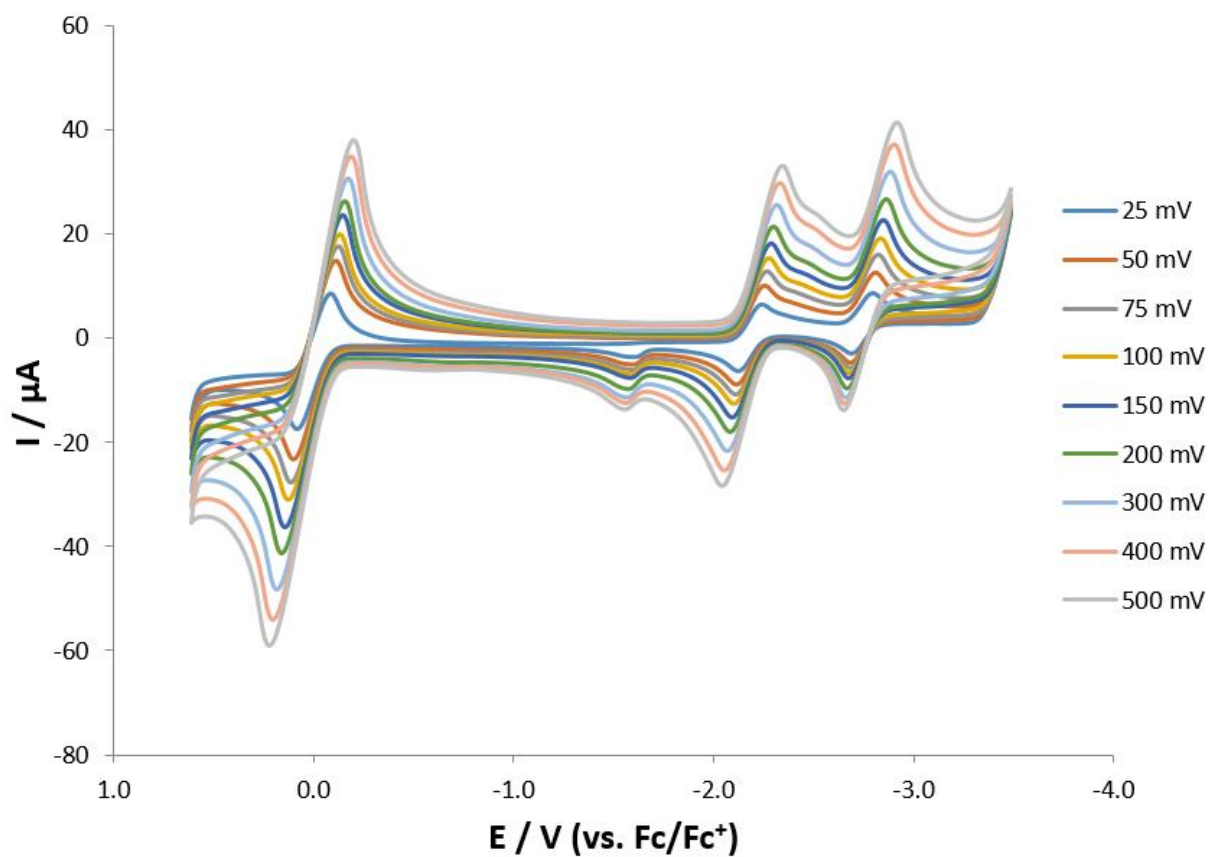


**Figure S26.** Room temperature cyclic voltammogram of **11** in DME (vs [Cp<sub>2</sub>Fe]<sup>0/+</sup>). (0.1M [NBu<sub>4</sub>][PF<sub>6</sub>] as supporting electrolyte).

**Table S11.** Electrochemical data for **11** in DME (vs. [Cp<sub>2</sub>Fe]<sup>0/+</sup>).

Feature 1 (11)	Scan rate, V/s	E <sub>p,c</sub> , V	E <sub>p,a</sub> , V	ΔE <sub>p</sub> , V	i <sub>p,c</sub> /i <sub>p,a</sub>
	0.025	-2.799	-2.693	0.106	1.04
	0.050	-2.813	-2.687	0.126	1.02
	0.075	-2.827	-2.687	0.140	1.07
	0.100	-2.838	-2.681	0.157	1.07
	0.150	-2.852	-2.678	0.174	1.06
	0.200	-2.867	-2.671	0.196	1.02
	0.300	-2.887	-2.663	0.224	1.02
	0.400	-2.906	-2.658	0.248	0.97
	0.500	-2.921	-2.653	0.268	0.96
Feature 2 (11)	Scan rate, V/s	E <sub>p,c</sub> , V	E <sub>p,a</sub> , V	ΔE <sub>p</sub> , V	i <sub>p,c</sub> /i <sub>p,a</sub>
	0.025	-2.245	-2.126	0.119	1.06
	0.050	-2.258	-2.117	0.141	1.14
	0.075	-2.270	-2.113	0.157	1.16
	0.100	-2.280	-2.104	0.176	1.13
	0.150	-2.291	-2.095	0.196	1.05
	0.200	-2.303	-2.085	0.218	1.17
	0.300	-2.319	-2.071	0.248	1.14
	0.400	-2.334	-2.056	0.278	1.09
	0.500	-2.347	-2.045	0.302	1.07

**Table S12** Electrochemical data for **12** in DME (vs. [Cp<sub>2</sub>Fe]<sup>0/+</sup>).

Feature 1 (12)	Scan rate, V/s	E <sub>p,c</sub> , V	E <sub>p,a</sub> , V	ΔE <sub>p</sub> , V	<i>i</i> <sub>p,c</sub> / <i>i</i> <sub>p,a</sub>
	0.025	-2.82	-2.697	0.123	1.79
	0.050	-2.864	-2.696	0.168	1.20
	0.075	-2.891	-2.688	0.203	1.10
	0.100	-2.909	-2.684	0.225	1.08
	0.150	-2.933	-2.676	0.257	1.06
	0.200	-2.952	-2.666	0.286	1.03
	0.300	-2.987	-2.649	0.338	1.01
	0.400	-3.015	-2.644	0.371	0.99
	0.500	-3.035	-2.633	0.402	0.97
Feature 2 (12)	Scan rate, V/s	E <sub>p,c</sub> , V	E <sub>p,a</sub> , V	ΔE <sub>p</sub> , V	<i>i</i> <sub>p,c</sub> / <i>i</i> <sub>p,a</sub>
	0.025	-2.65	-2.137	0.513	1.62
	0.050	-3.06	-2.126	0.934	1.17
	0.075	-2.329	-2.113	0.216	1.29
	0.100	-2.344	-2.106	0.238	1.27
	0.150	-2.365	-2.091	0.274	1.21
	0.200	-2.381	-2.077	0.304	1.23
	0.300	-2.41	-2.05	0.36	1.19
	0.400	-2.435	-2.035	0.4	1.26
	0.500	-2.451	-2.018	0.433	1.24

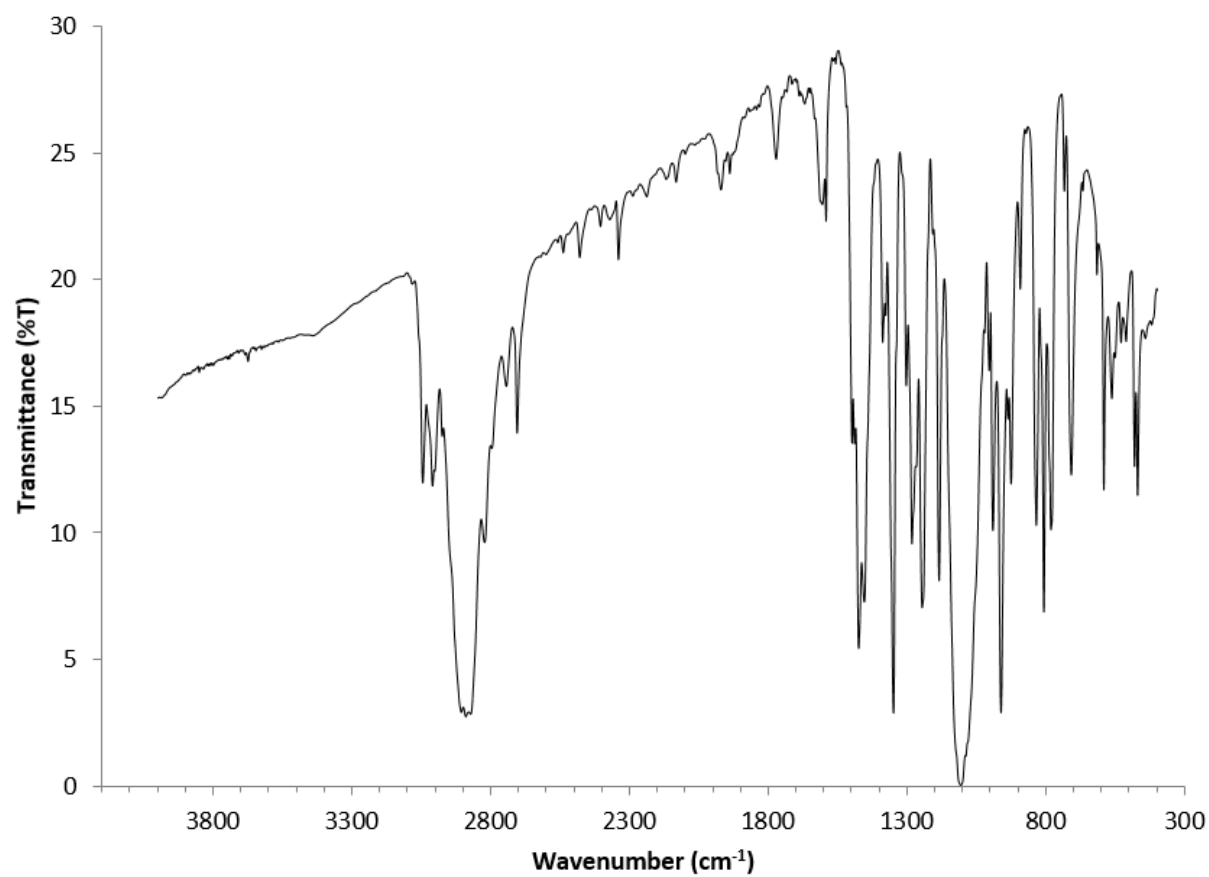


**Figure S27.** IR spectrum (KBr pellet) of **1**.

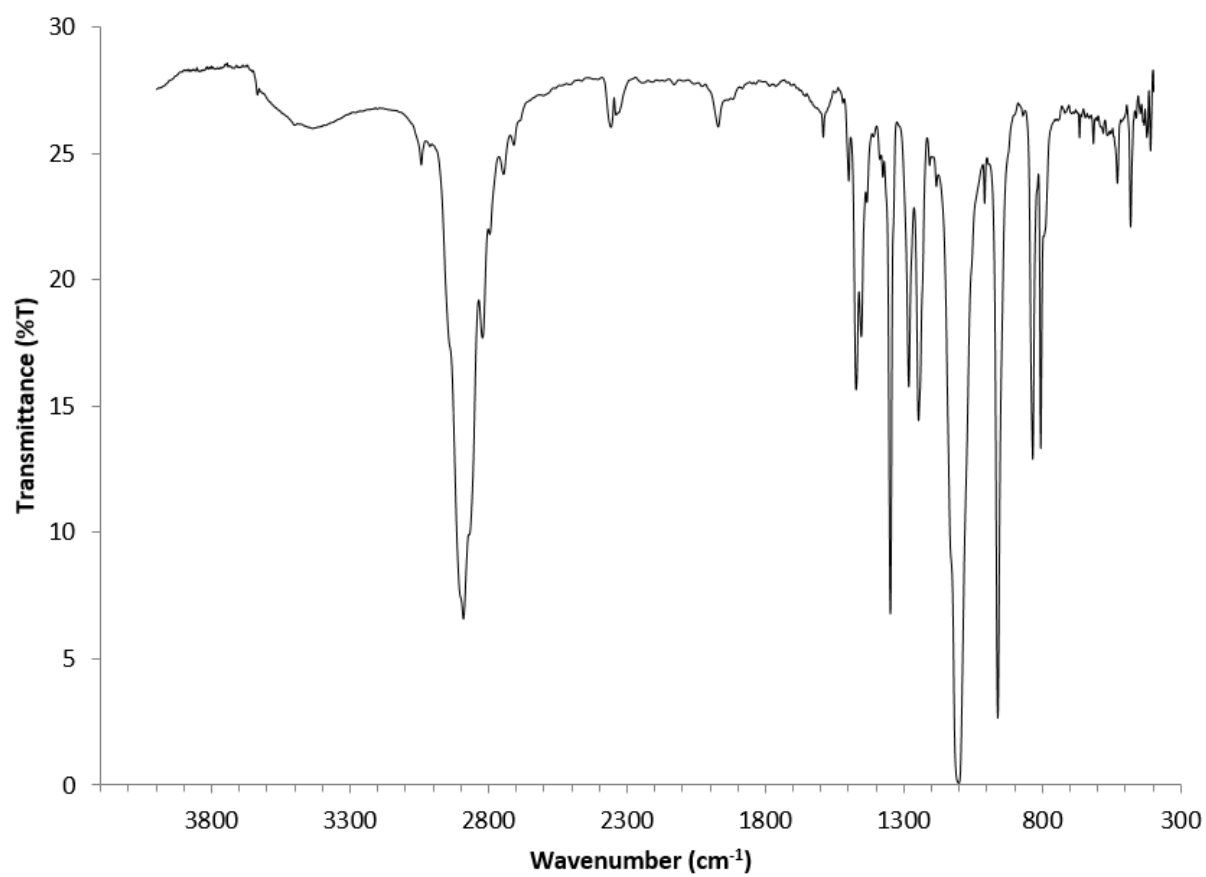


**Figure S28.** IR spectrum (KBr pellet) of **2**.



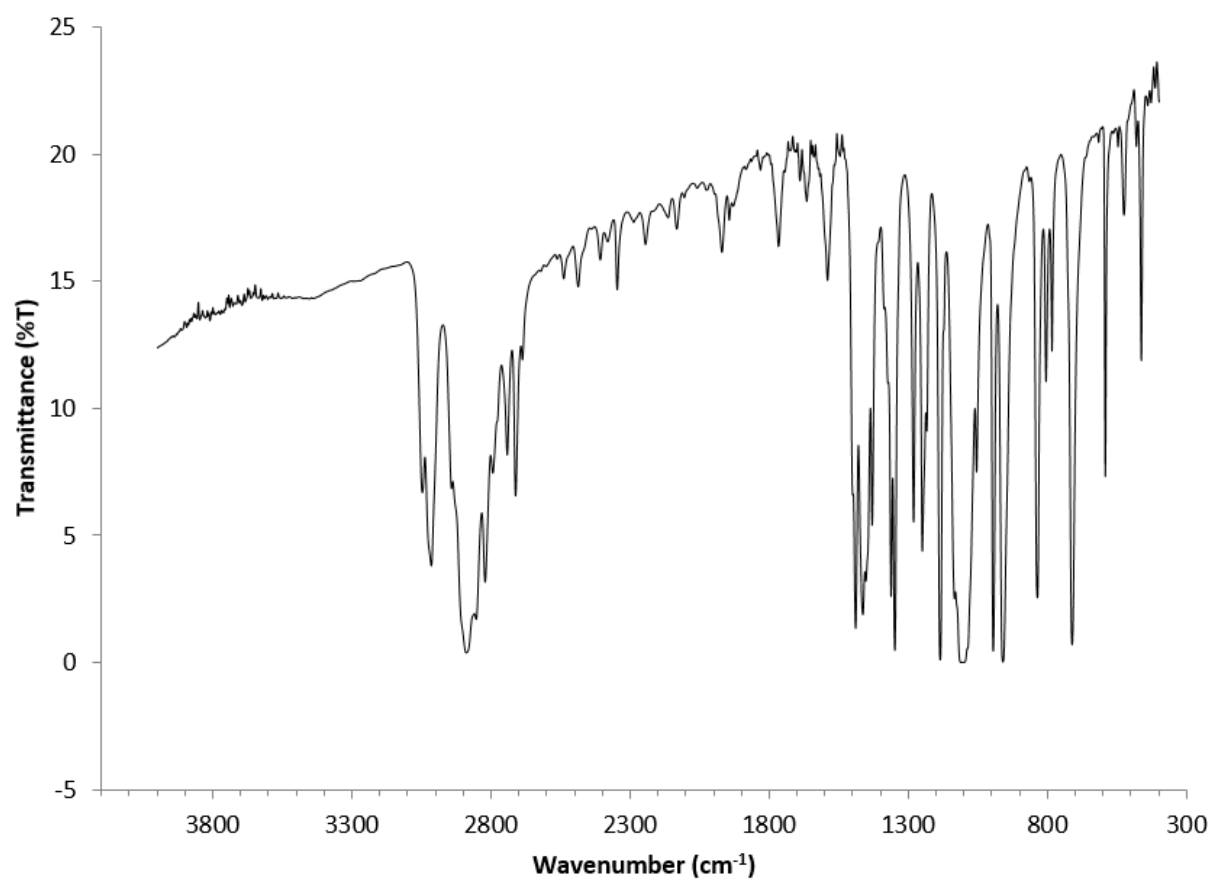


**Figure S29.** IR spectrum (KBr pellet) of **3**.

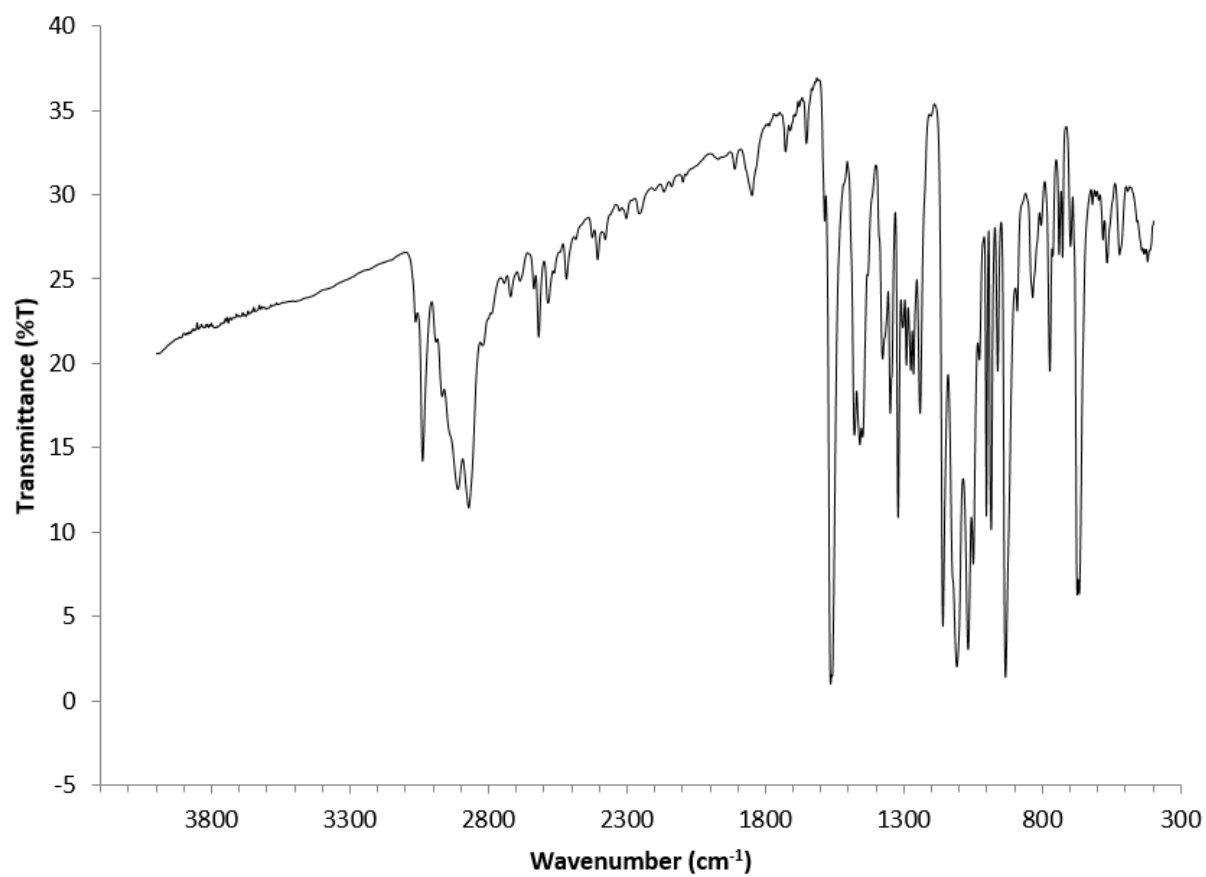


**Figure S30.** IR spectrum (KBr pellet) of **4**.

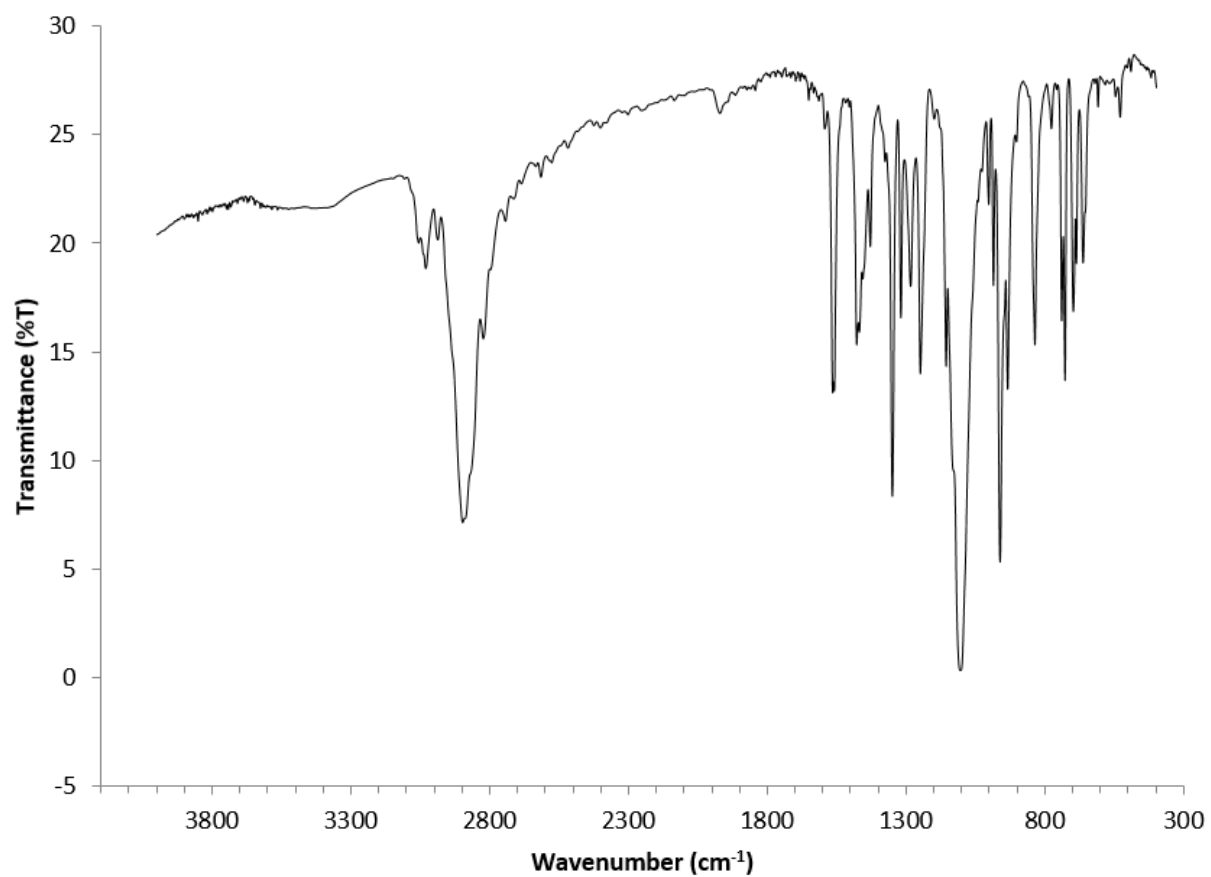


**Figure S31.** IR spectrum (KBr pellet) of **5**.

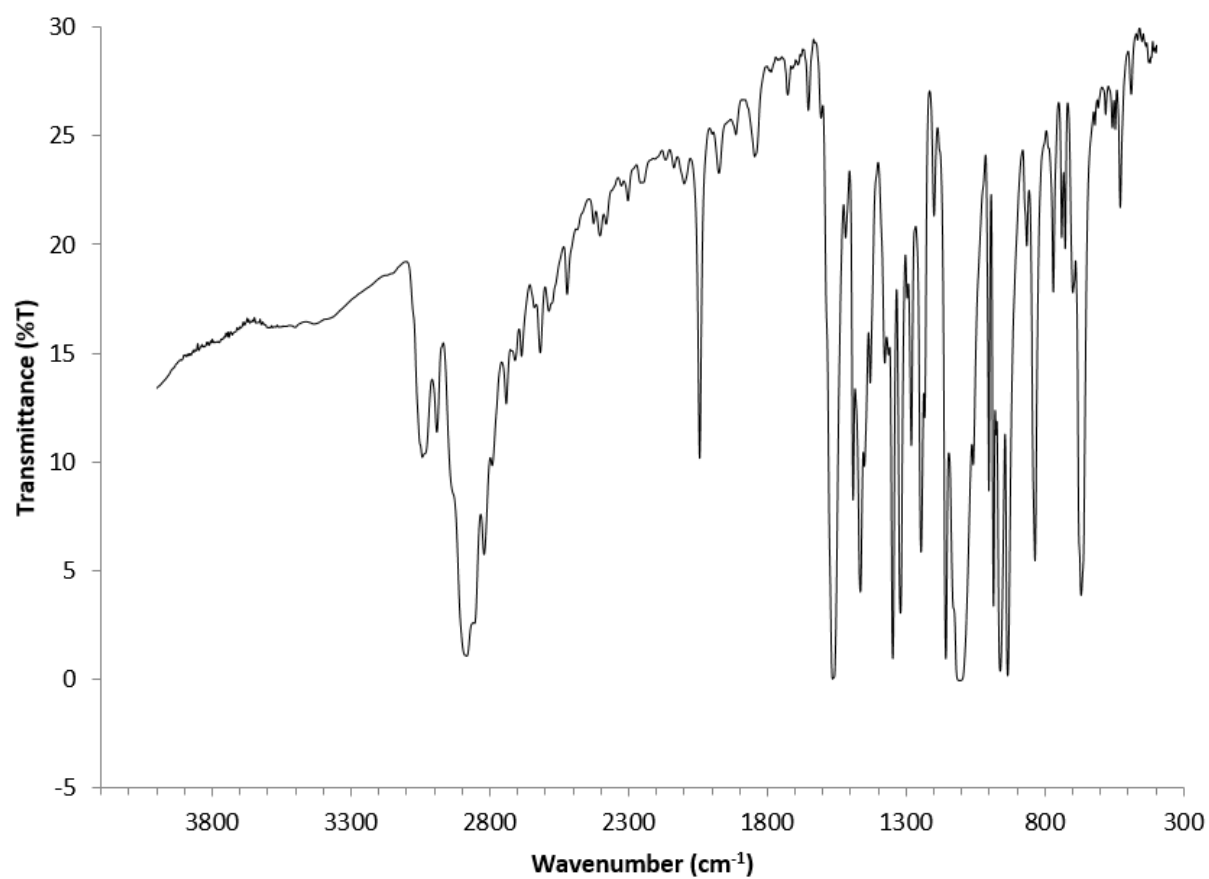


**Figure S32.** IR spectrum (KBr pellet) of **6**.

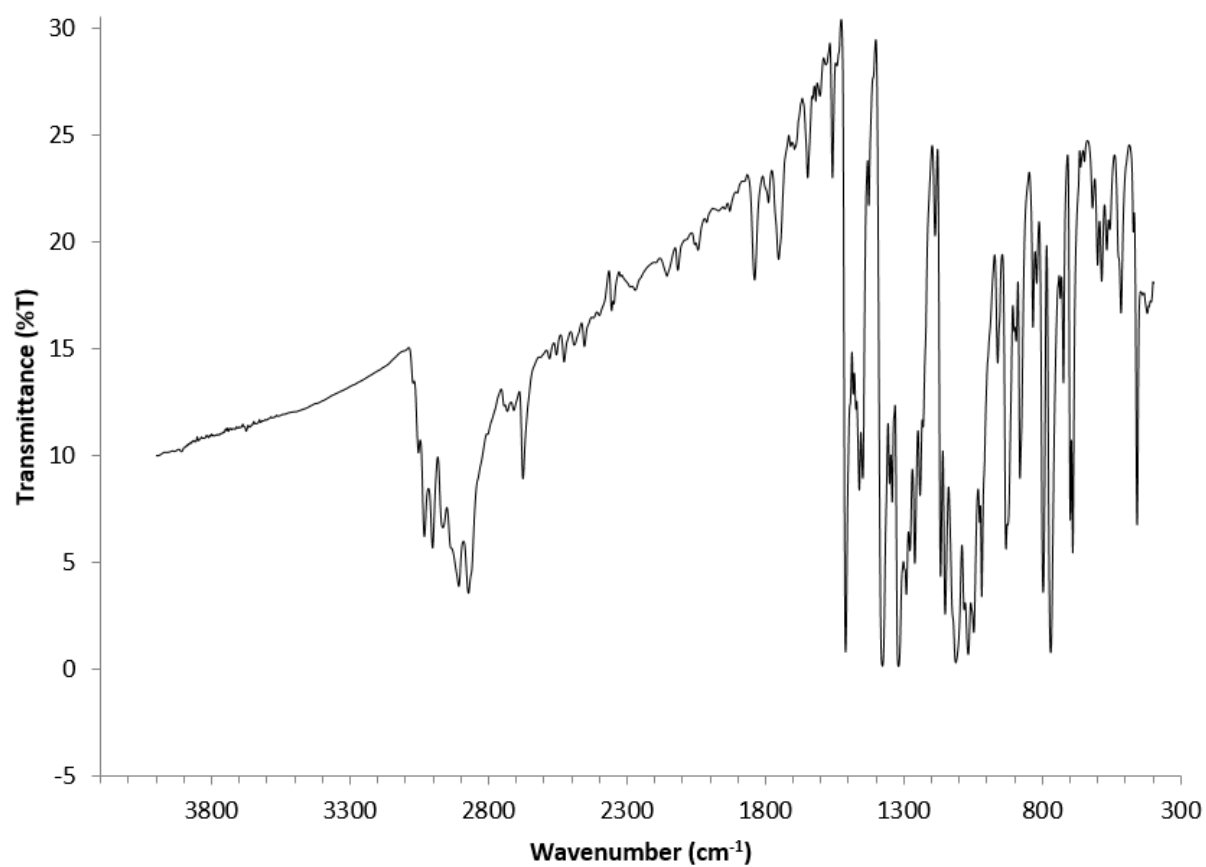


**Figure S33.** IR spectrum (KBr pellet) of **7**.

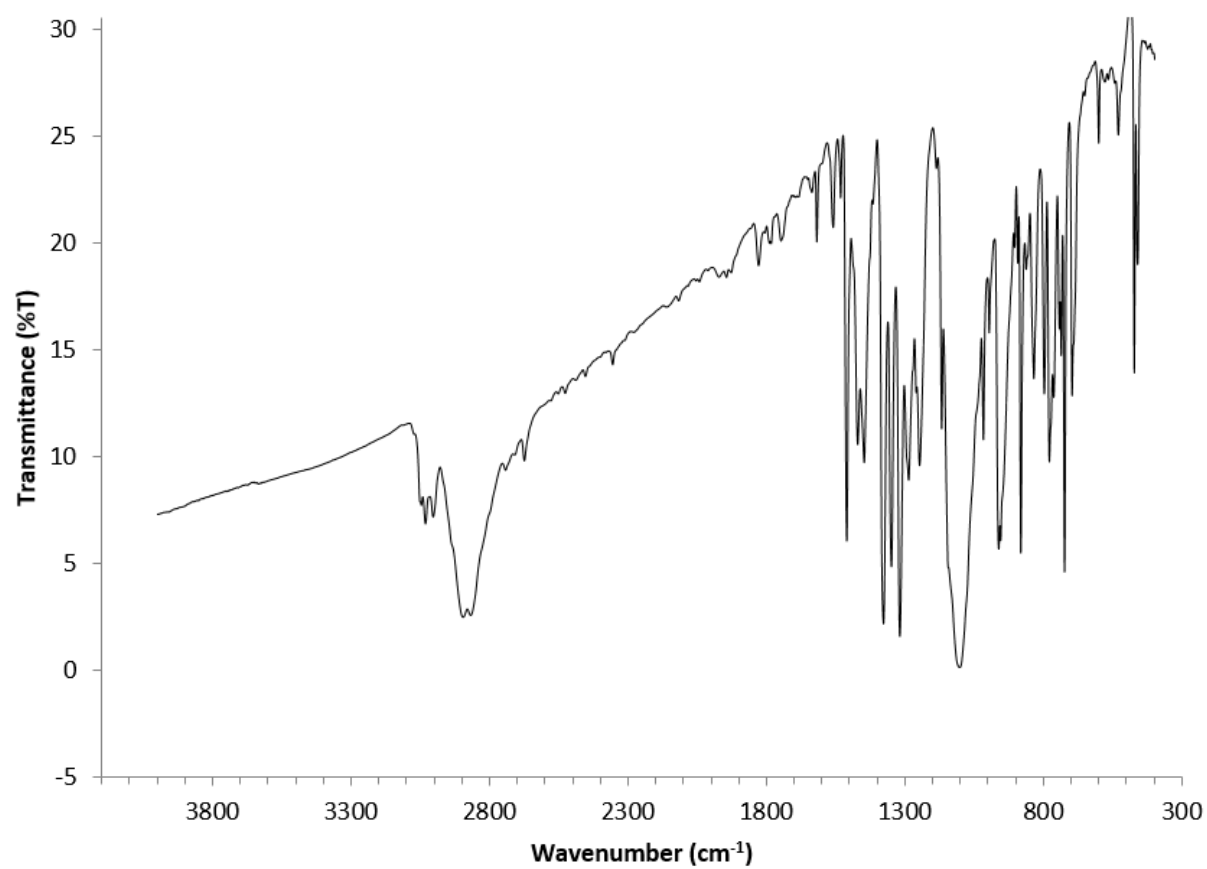


**Figure S34.** IR spectrum (KBr pellet) of **8**.

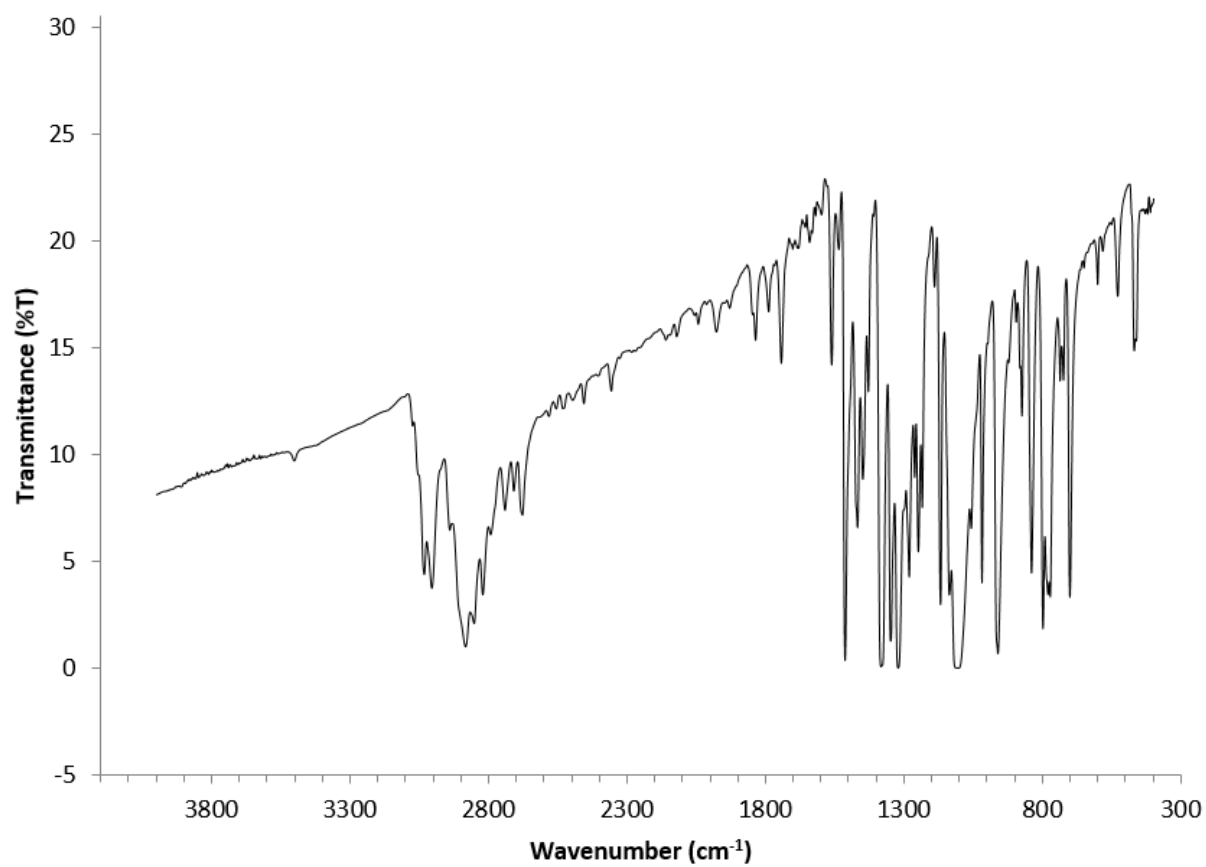


**Figure S35.** IR spectrum (KBr pellet) of **9**.

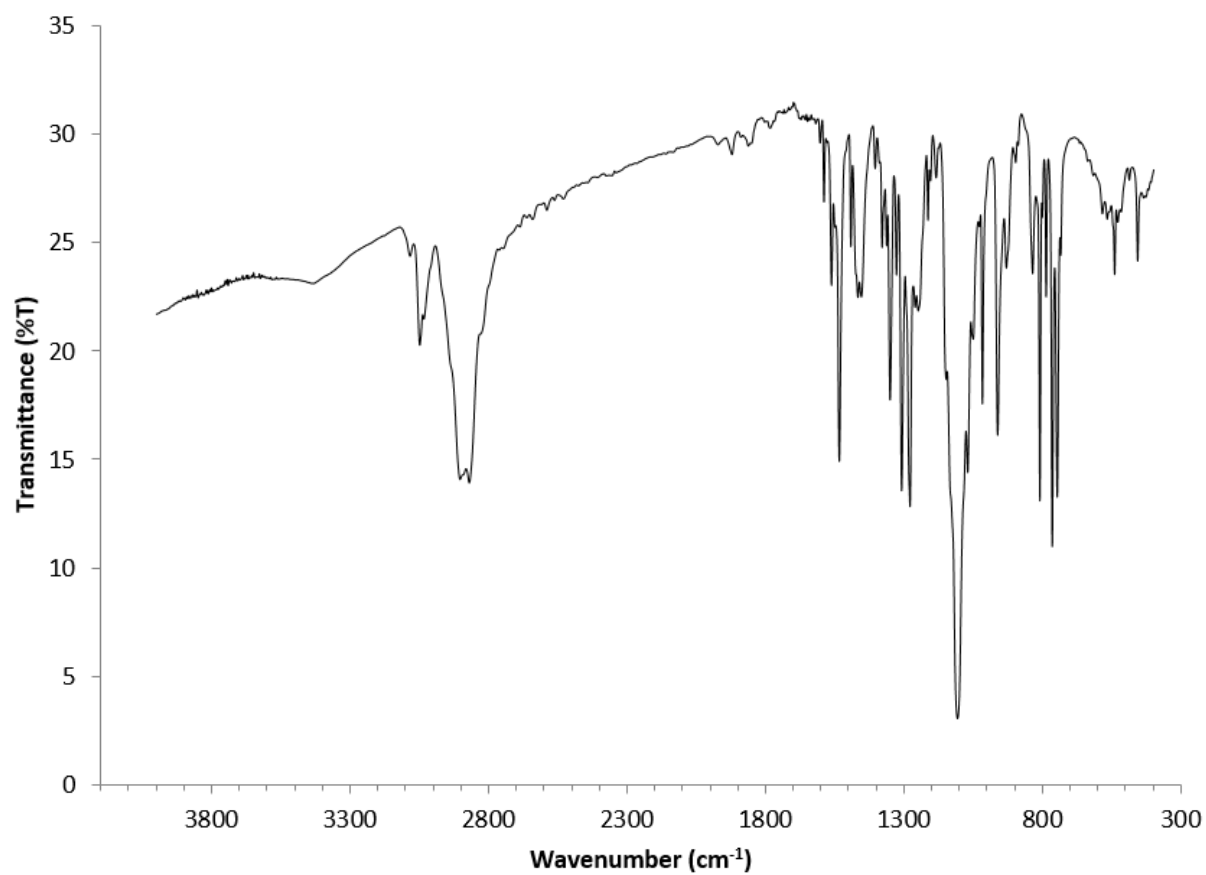


**Figure S35.** IR spectrum (KBr pellet) of **10**.



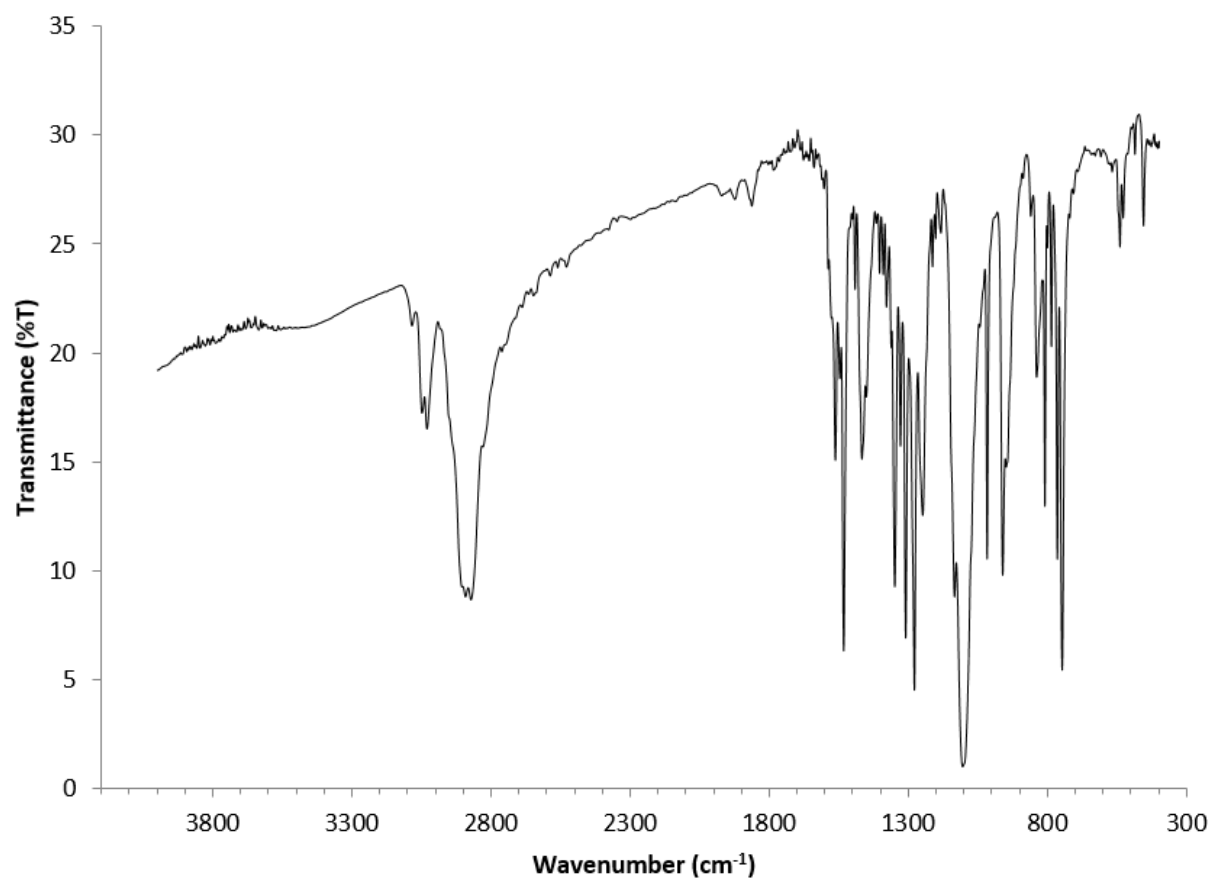


**Figure S36.** IR spectrum (KBr pellet) of **11**.

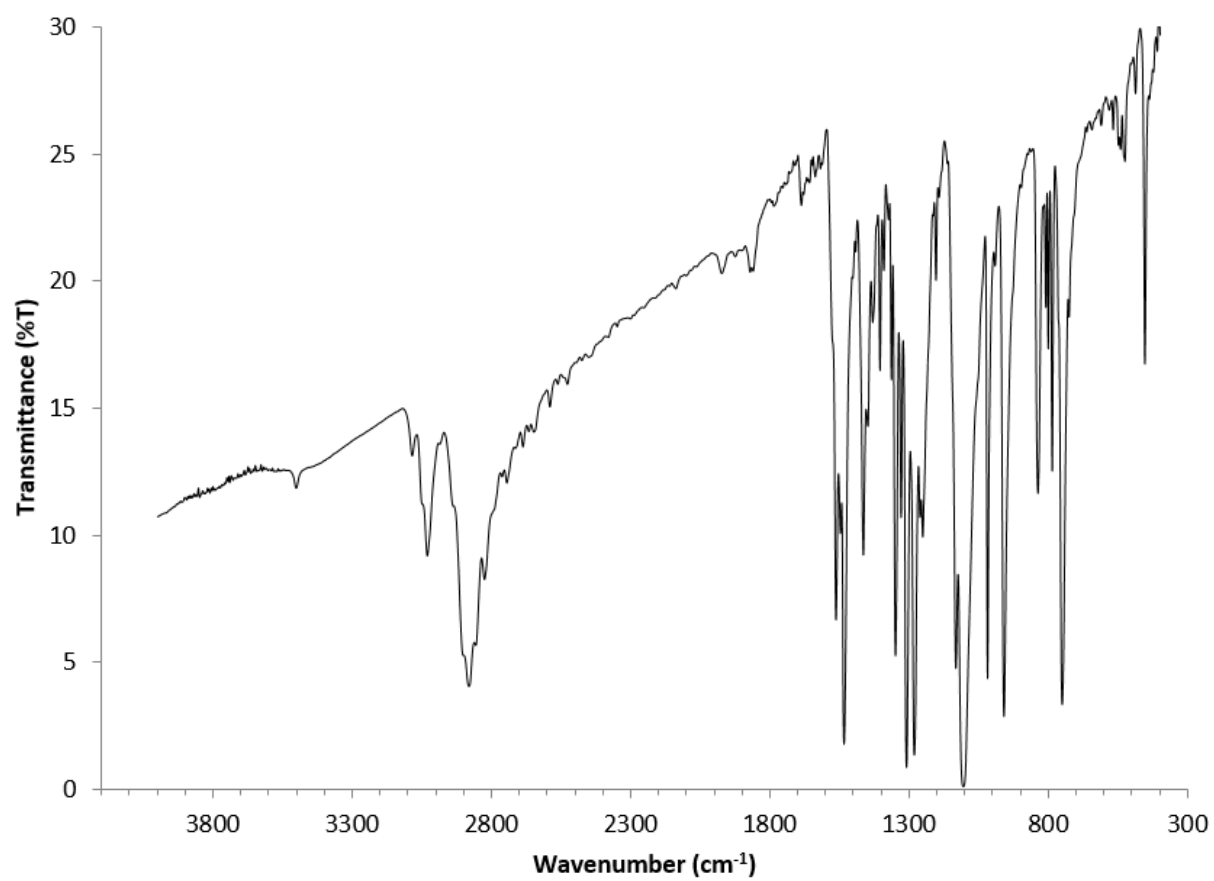


**Figure S37.** IR spectrum (KBr pellet) of **12**.

**Table S13** X-ray crystallographic data for 1-12.

	1	2	3	4
Empirical formula	C <sub>22</sub> H <sub>32</sub> LiO <sub>6</sub>	C <sub>26</sub> H <sub>42</sub> NaO <sub>8</sub>	C <sub>22</sub> H <sub>32</sub> KO <sub>6</sub>	C <sub>32</sub> H <sub>50</sub> LiO <sub>8</sub>
Crystal Habit, color	irregular, dark green	plate, dark green	block, dark green	rod, purple blue
Crystal size (mm)	0.10 × 0.08 × 0.05	0.4 × 0.3 × 0.05	0.27 × 0.13 × 0.11	0.90 × 0.37 × 0.15
Crystal system	orthorhombic	triclinic	triclinic	Monoclinic
Space group	<i>Pbca</i>	<i>P2<sub>1</sub>/n</i>	<i>P</i> $\bar{1}$	<i>P2<sub>1</sub>/c</i>
Volume (Å <sup>3</sup> )	4186.1(3)	2646.3(4)	1109.0(2)	3151.2(4)
a (Å)	8.6020(3)	8.6161(8)	8.7069(8)	12.1048(8)
b (Å)	21.8870(8)	15.756(1)	9.1354(8)	17.611(1)
c (Å)	22.2344(8)	19.686(2)	15.410(1)	15.213(1)
α(°)	90	90	98.506(2)	90
β(°)	90	98.022(2)	91.665(2)	103.670(1)
γ(°)	90	90	113.205(1)	90
Z	8	4	2	4
Formula weight (g/mol)	399.42	505.59	431.57	569.66
Density (calculated) (Mg/m <sup>3</sup> )	1.268	1.269	1.292	1.201
Absorption coefficient (mm <sup>-1</sup> )	0.090	0.106	0.274	0.084
F <sub>000</sub>	1720.0	1092.0	462.0	1236.0
Total no. reflections	4827	6523	5873	7229
Unique reflections	3792	3999	4238	5349
Final R indices [ <i>I</i> > 2σ( <i>I</i> )]	R <sub>1</sub> = 0.0368, wR <sub>2</sub> = 0.0918	R <sub>1</sub> = 0.0368, wR <sub>2</sub> = 0.0918	R <sub>1</sub> = 0.0513, wR <sub>2</sub> = 0.1081	R <sub>1</sub> = 0.0406, wR <sub>2</sub> = 0.1030
Largest diff. peak and hole (e <sup>-</sup> Å <sup>-3</sup> )	0.32 and -0.23	0.30 and -0.30	0.35 and -0.49	0.26 and -0.20
GOF	1.025	1.006	1.035	1.000

	5	6	8	9
Empirical formula	C <sub>32</sub> H <sub>50</sub> NaO <sub>8</sub>	C <sub>32</sub> H <sub>50</sub> KO <sub>8</sub>	C <sub>30</sub> H <sub>44</sub> NaO <sub>8</sub>	C <sub>34</sub> H <sub>50</sub> KO <sub>8</sub>
Crystal Habit, color	rod, purple blue	rod, purple	plate, purple	block, blue-purple
Crystal size (mm)	0.6 × 0.3 × 0.2	0.5 × 0.2 × 0.18	0.18 × 0.09 × 0.02	0.30 × 0.10 × 0.05
Crystal system	monoclinic	monoclinic	triclinic	monoclinic
Space group	P2 <sub>1</sub> /n	P2 <sub>1</sub> /n	P $\bar{1}$	P2 <sub>1</sub>
Volume (Å <sup>3</sup> )	3176.1(6)	3244.5(5)	1484.90(15)	3359.0(4)
a (Å)	12.7772(13)	12.892(1)	11.5114(7)	13.0082(8)
b (Å)	17.6539(18)	18.017(2)	11.8386(7)	18.1719(11)
c (Å)	15.1994(15)	15.295(1)	13.6270(8)	15.3774(10)
α(°)	90	90	65.2130(10)	90
β(°)	112.120(2)	114.036(2)	70.1690(10)	112.4700(10)
γ(°)	90	90	63.7510(10)	90
Z	4	4	2	4
Formula weight (g/mol)	585.71	599.80	555.64	625.84
Density (calculated) (Mg/m <sup>3</sup> )	1.225	1.228	1.243	1.238
Absorption coefficient (mm <sup>-1</sup> )	0.098	0.211	0.101	0.206
F <sub>000</sub>	1268.0	1292.0	598.0	1348.0
Total no. reflections	4798	7460	6810	14982
Unique reflections	3149	4130	4442	11167
Final R indices [ <i>I</i> > 2σ( <i>I</i> )]	R <sub>1</sub> = 0.0424, wR <sub>2</sub> = 0.1110	R <sub>1</sub> = 0.0607, wR <sub>2</sub> = 0.1708	R <sub>1</sub> = 0.0491, wR <sub>2</sub> = 0.1074	R <sub>1</sub> = 0.0444, wR <sub>2</sub> = 0.0878
Largest diff. peak and hole (e <sup>-</sup> Å <sup>-3</sup> )	0.21 and -0.23	0.76 and -0.43	0.25 and -0.27	0.33 and -0.26
GOF	1.004	1.020	1.011	1.004

	10	11	12
Empirical formula	C <sub>46</sub> H <sub>52</sub> LiO <sub>8</sub>	C <sub>36</sub> H <sub>46</sub> NaO <sub>8</sub>	C <sub>40</sub> H <sub>52</sub> KO <sub>8</sub>
Crystal Habit, color	block, purple	prism, purple	plate, dark purple
Crystal size (mm)	0.23 × 0.17 × 0.11	0.18 × 0.09 × 0.02	0.24 × 0.18 × 0.02
Crystal system	triclinic	monoclinic	monoclinic
Space group	<i>P</i> $\bar{1}$	C2/c	P2 <sub>1</sub> /c
Volume (Å <sup>3</sup> )	1923.1(2)	3277.9(2)	7361.5(13)
a (Å)	8.3174(5)	22.1045(7)	17.5120(18)
b (Å)	12.2288(8)	12.5068(4)	18.3856(19)
c (Å)	20.1448(13)	16.0000(9)	23.115(2)
α(°)	104.2740(10)	90	90
β(°)	99.6340(10)	132.18	98.461(2)
γ(°)	97.9080(10)	90	90
Z	2	4	8
Formula weight (g/mol)	739.81	629.72	699.91
Density (calculated) (M/g/m <sup>3</sup> )	1.278	1.276	1.263
Absorption coefficient (mm <sup>-1</sup> )	0.086	0.100	0.196
F <sub>000</sub>	790.0	1348.0	3000.0
Total no. reflections	9534	3809	18221
Unique reflections	5153	3414	11429
Final R indices [ <i>I</i> > 2σ( <i>I</i> )]	R <sub>1</sub> = 0.0635, wR <sub>2</sub> = 0.1438	R <sub>1</sub> = 0.0335, wR <sub>2</sub> = 0.0954	R <sub>1</sub> = 0.0656, wR <sub>2</sub> = 0.1784
Largest diff. peak and hole (e <sup>-</sup> Å <sup>-3</sup> )	0.33 and -0.25	0.38 and -0.21	0.84 and -0.46
GOF	0.976	1.024	1.040

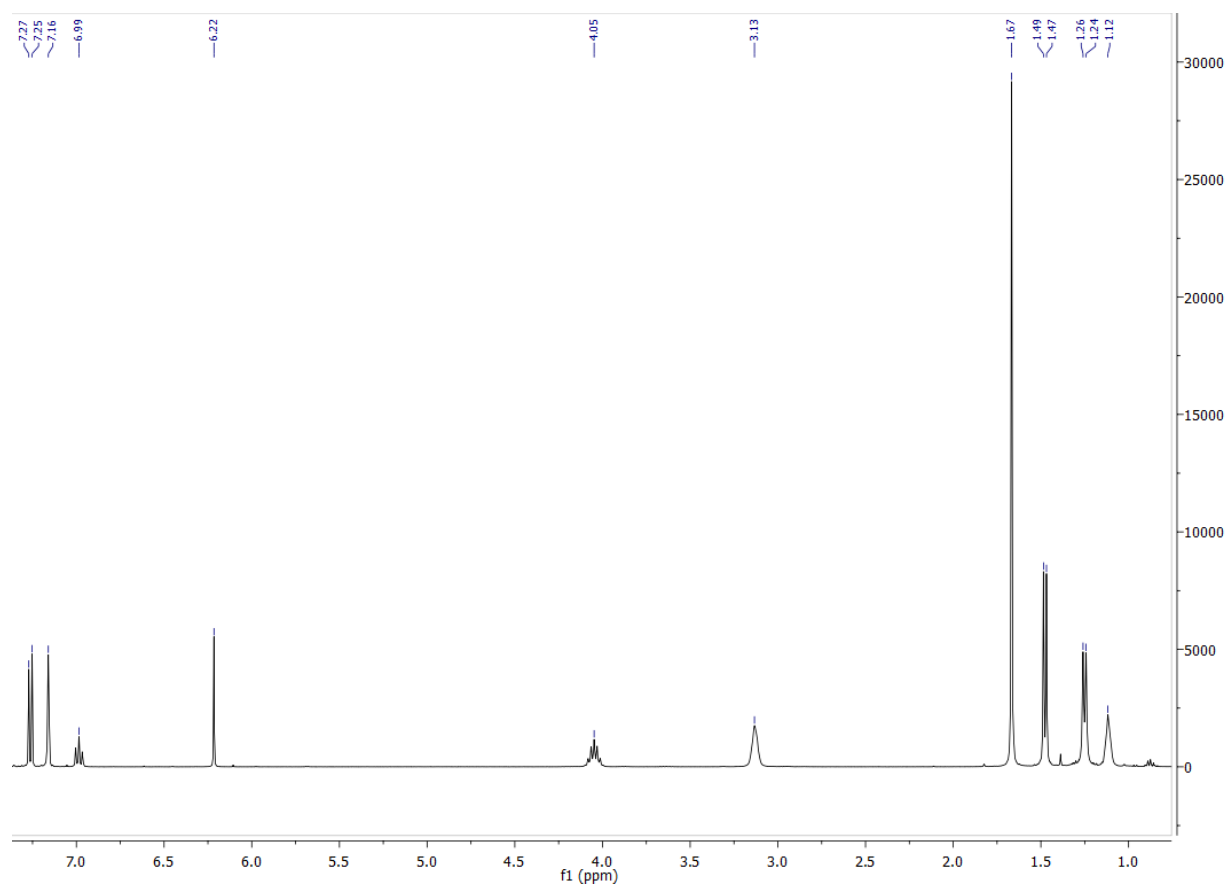


**Figure S38.**  $^1\text{H}$  NMR spectrum of **13** in  $\text{C}_6\text{D}_6$  at  $25^\circ\text{C}$ .

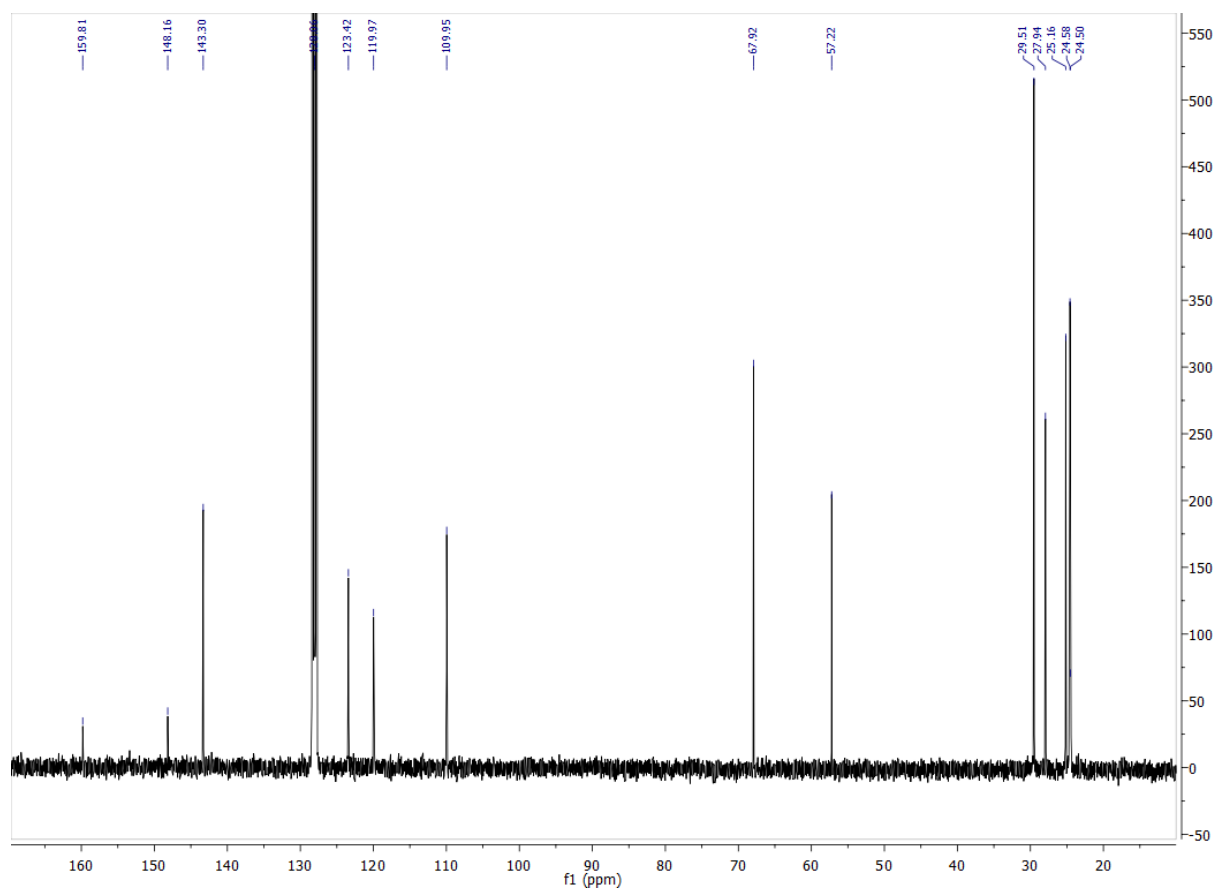


**Figure S39.**  $^{13}\text{C}$  NMR spectrum of **13** in  $\text{C}_6\text{D}_6$  at  $25^\circ\text{C}$ .

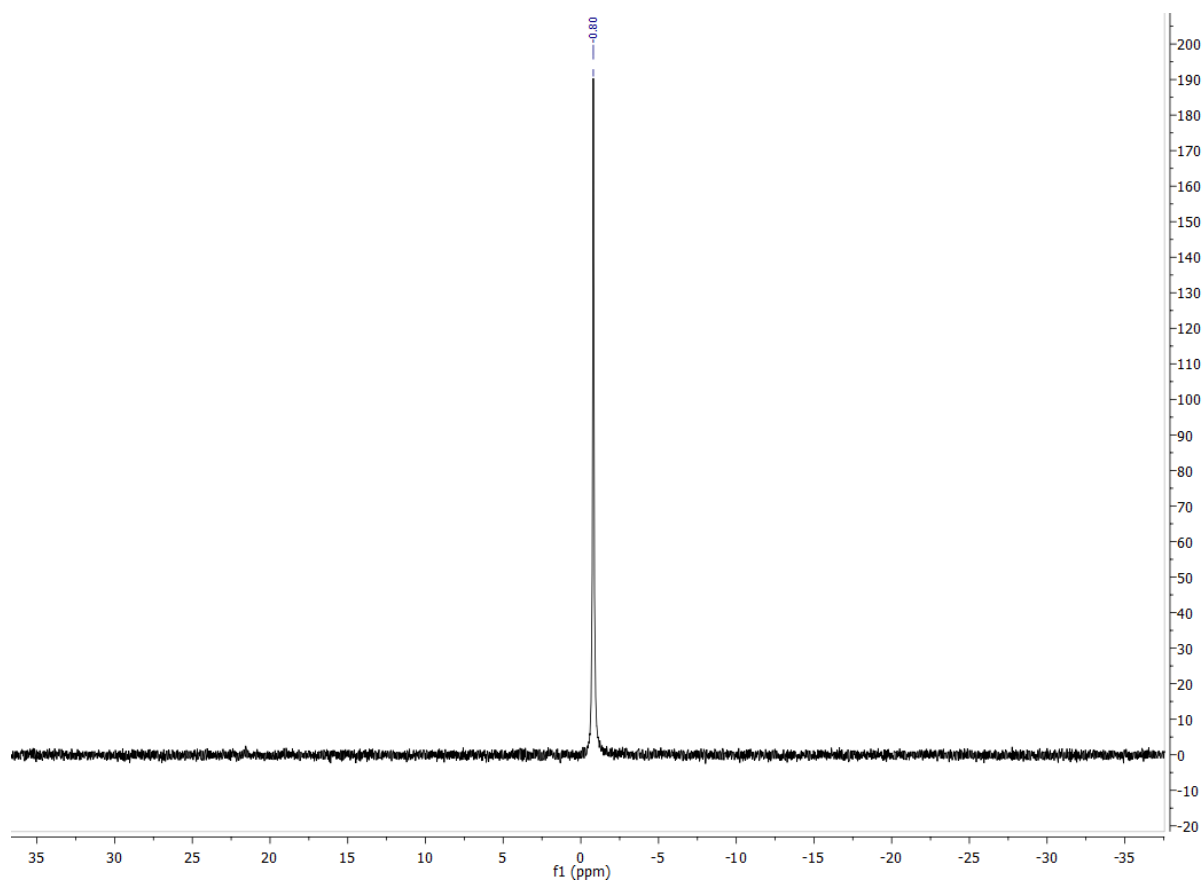


**Figure S40.**  $^7\text{Li}$  NMR spectrum of **13** in  $\text{C}_6\text{D}_6$  at 25 °C.



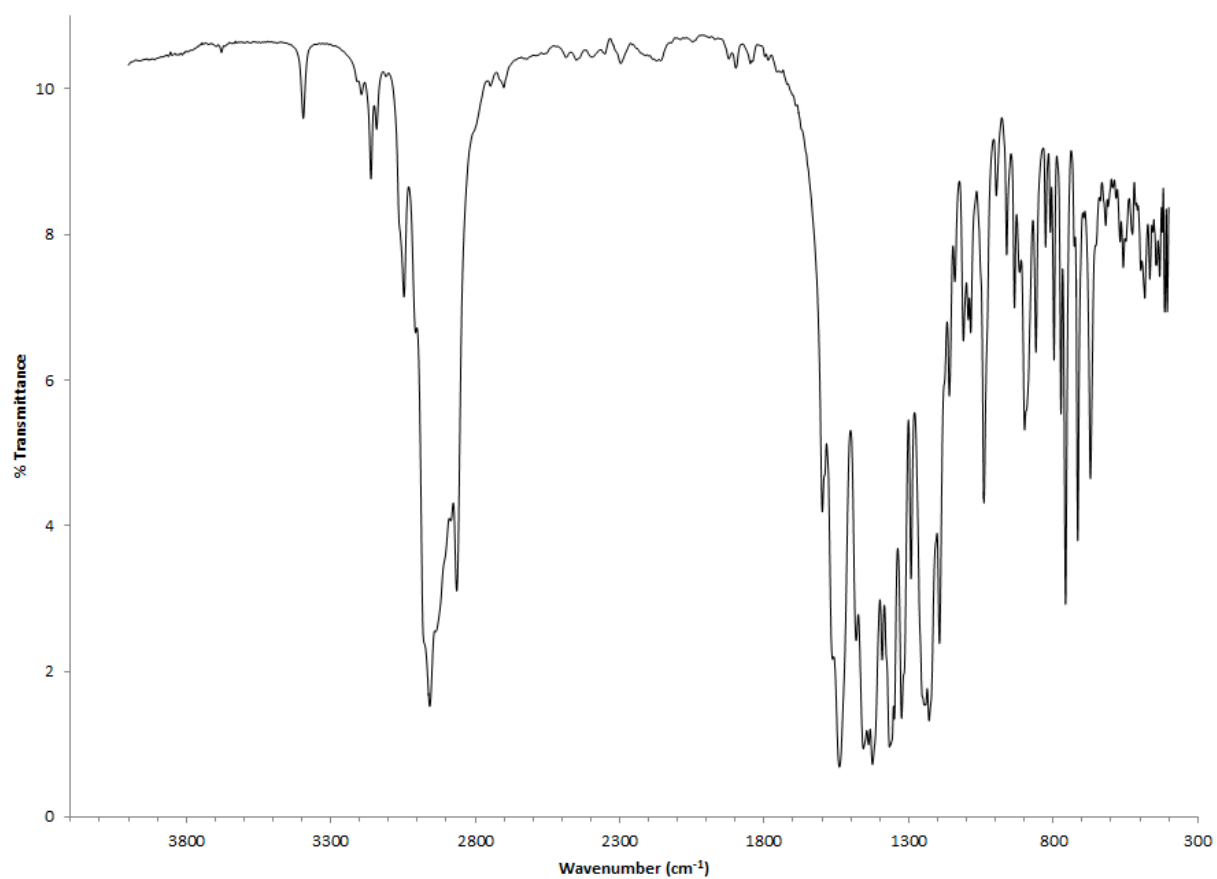


**Figure S41.** IR spectrum (KBr pellet) of **13**.

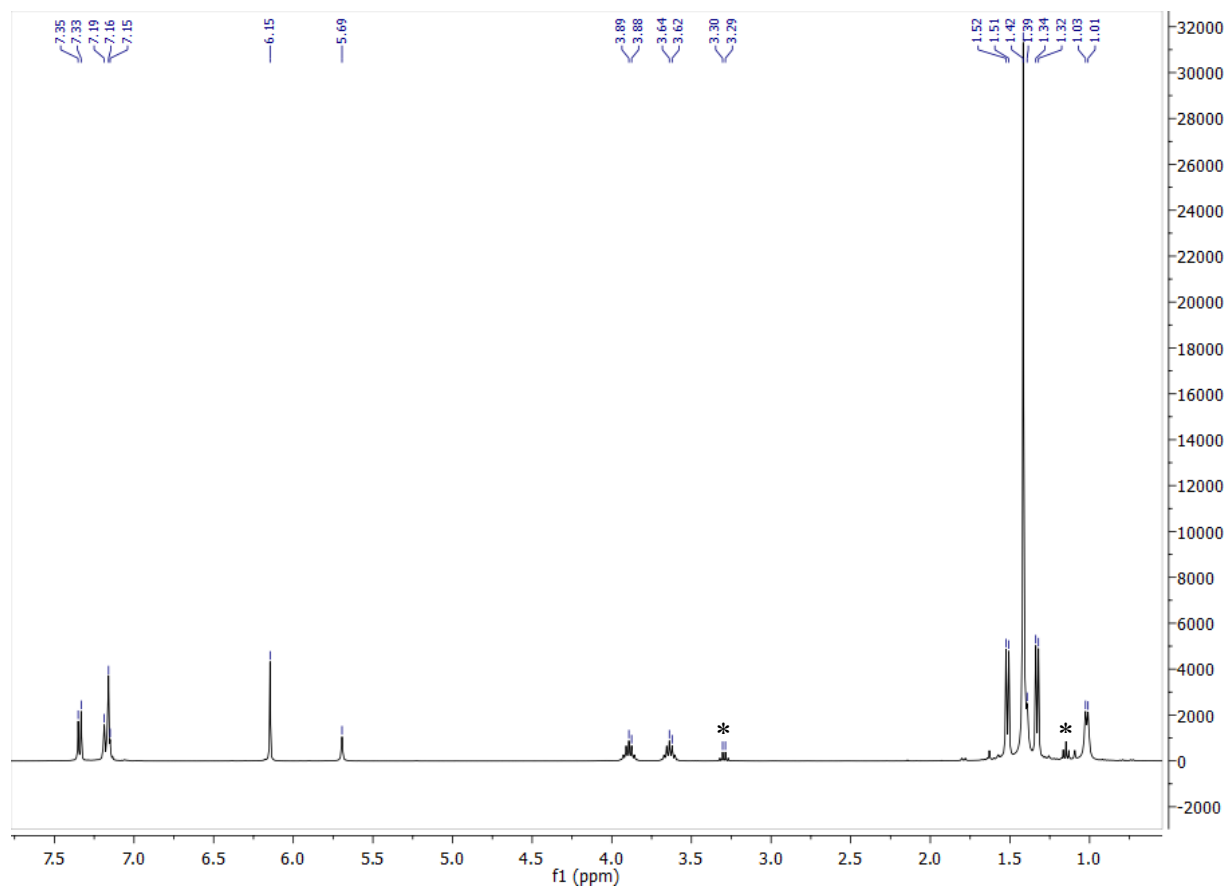


**Figure S42.**  $^1\text{H}$  NMR spectrum of **14** in  $\text{C}_6\text{D}_6$  at  $25^\circ\text{C}$ . Asterisks denote the presence of residual  $\text{Et}_2\text{O}$ .

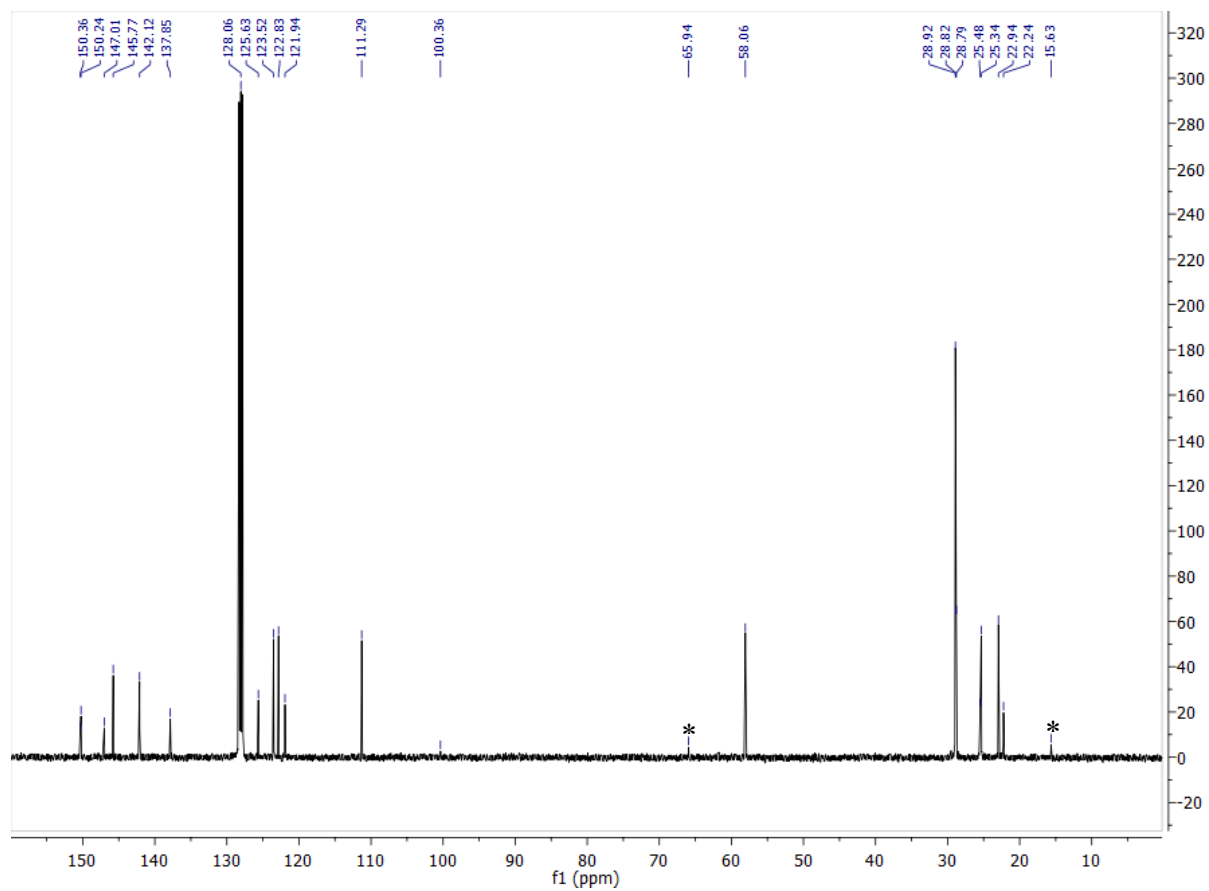


**Figure S43.**  $^{13}\text{C}$  NMR spectrum of **14** in  $\text{C}_6\text{D}_6$  at 25 °C. Asterisks denote the presence of residual  $\text{Et}_2\text{O}$

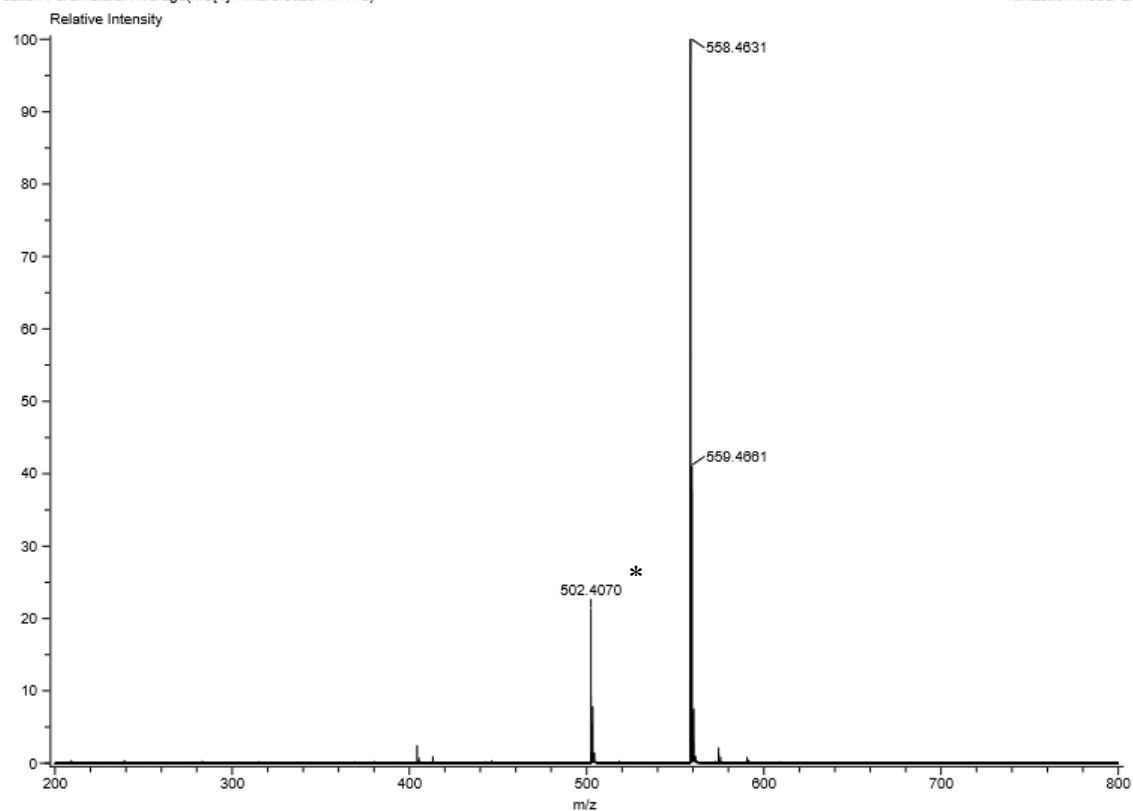


**Figure S44.** ESI mass spectrum of 14. Asterisk denotes -<sup>t</sup>Bu fragmentation of a group from the imidazolin-2-iminato ring ( $[M+H-{}^t\text{Bu}]^+$ ; calcd  $m/z$  502.39).

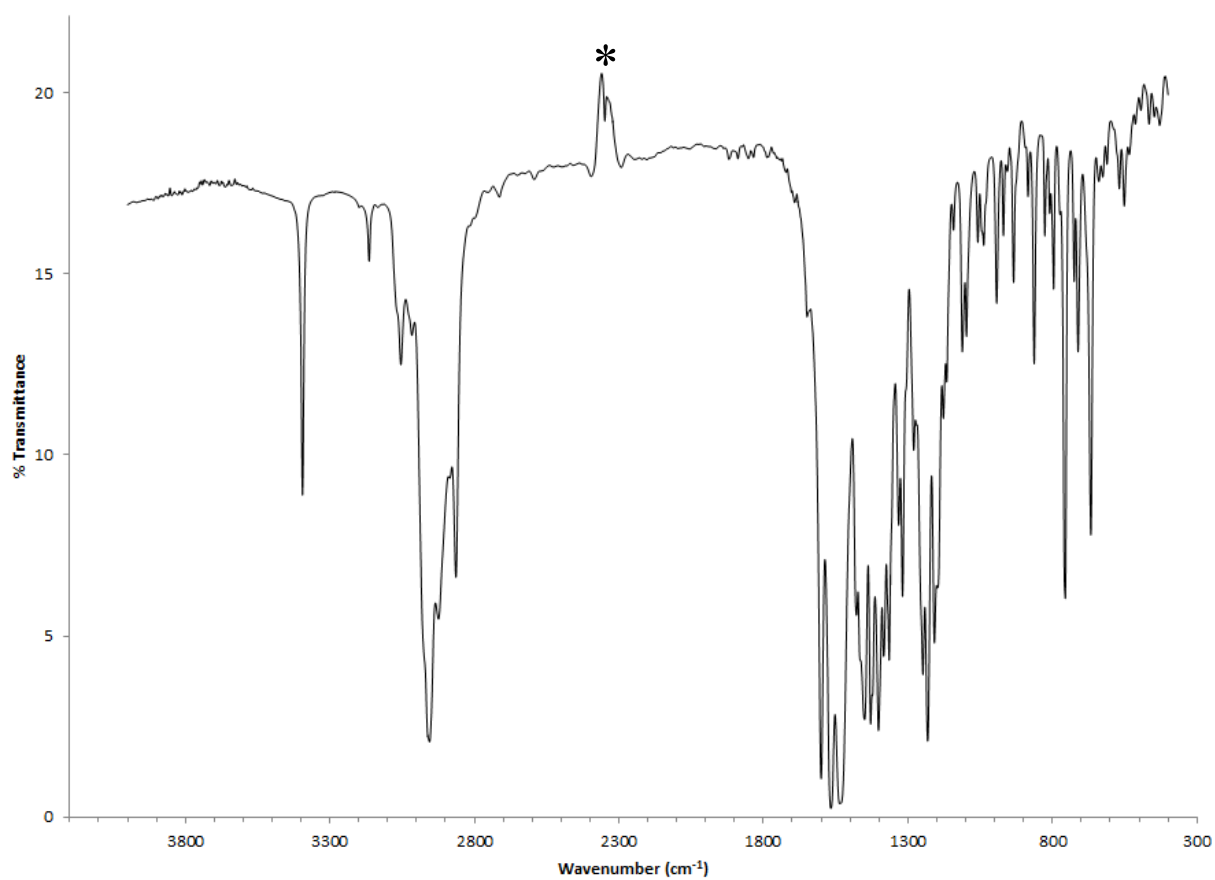


**Figure S45.** IR spectrum (KBr pellet) of **14**. Asterisk denotes background subtraction error.

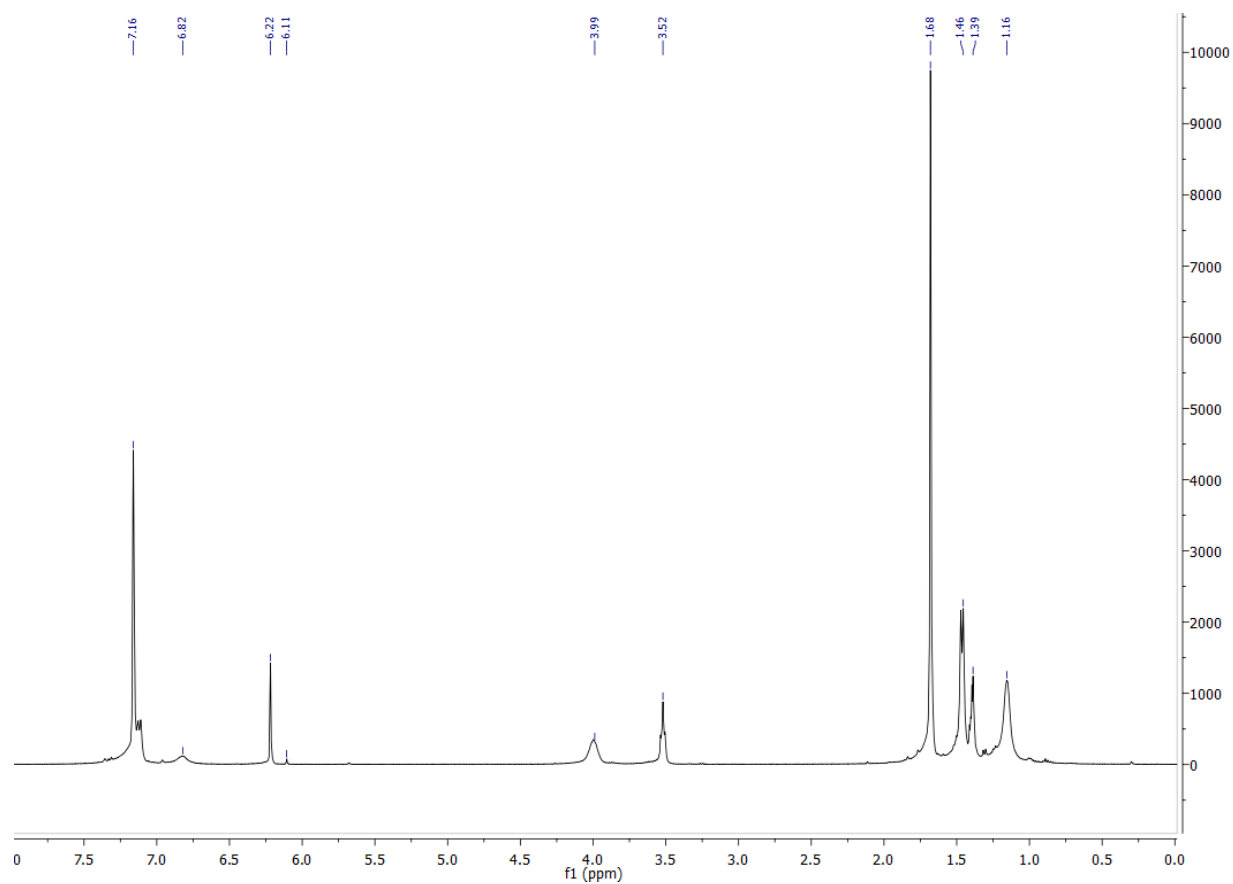


**Figure S46.**  $^1\text{H}$  NMR spectrum of **15** in  $\text{C}_6\text{D}_6$  at  $25^\circ\text{C}$ .

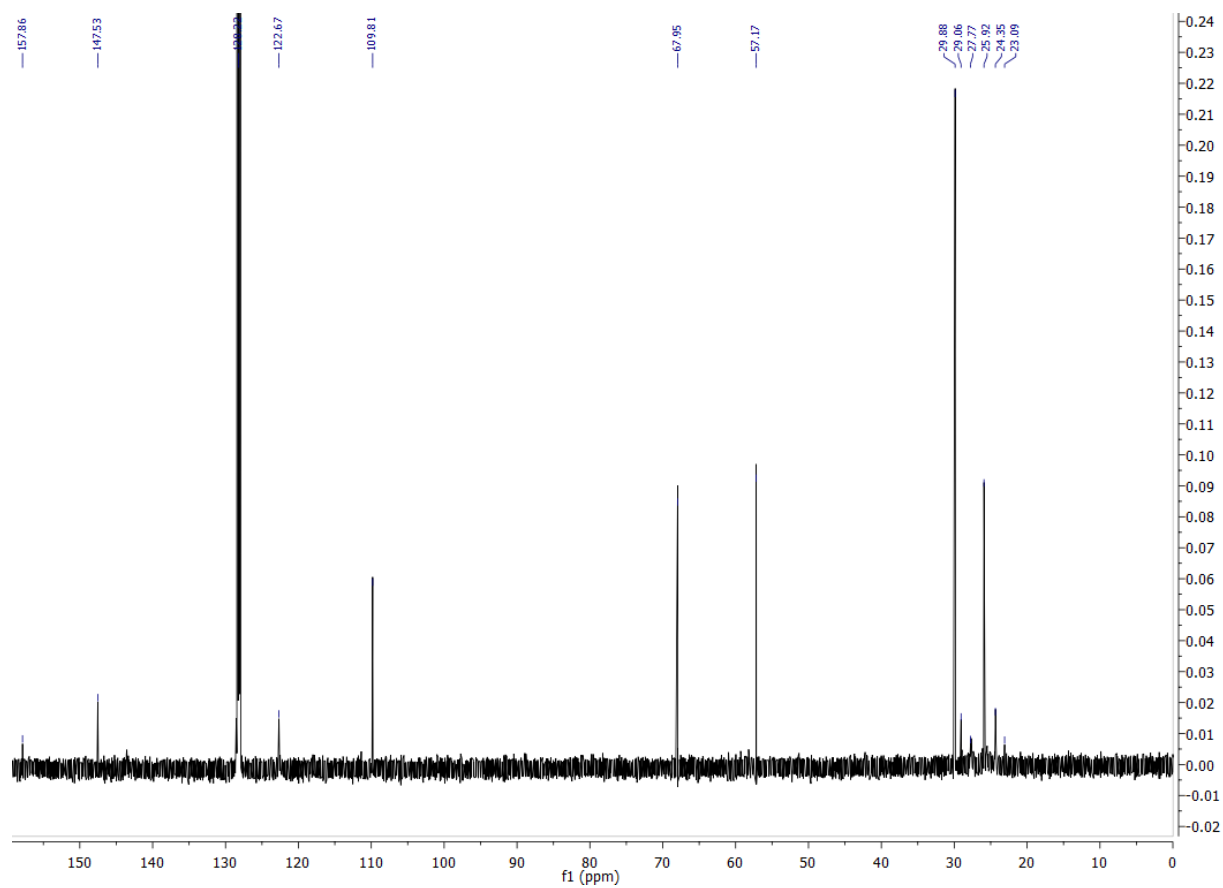


**Figure S47.**  $^{13}\text{C}$  NMR spectrum of **15** in  $\text{C}_6\text{D}_6$  at  $25^\circ\text{C}$ .

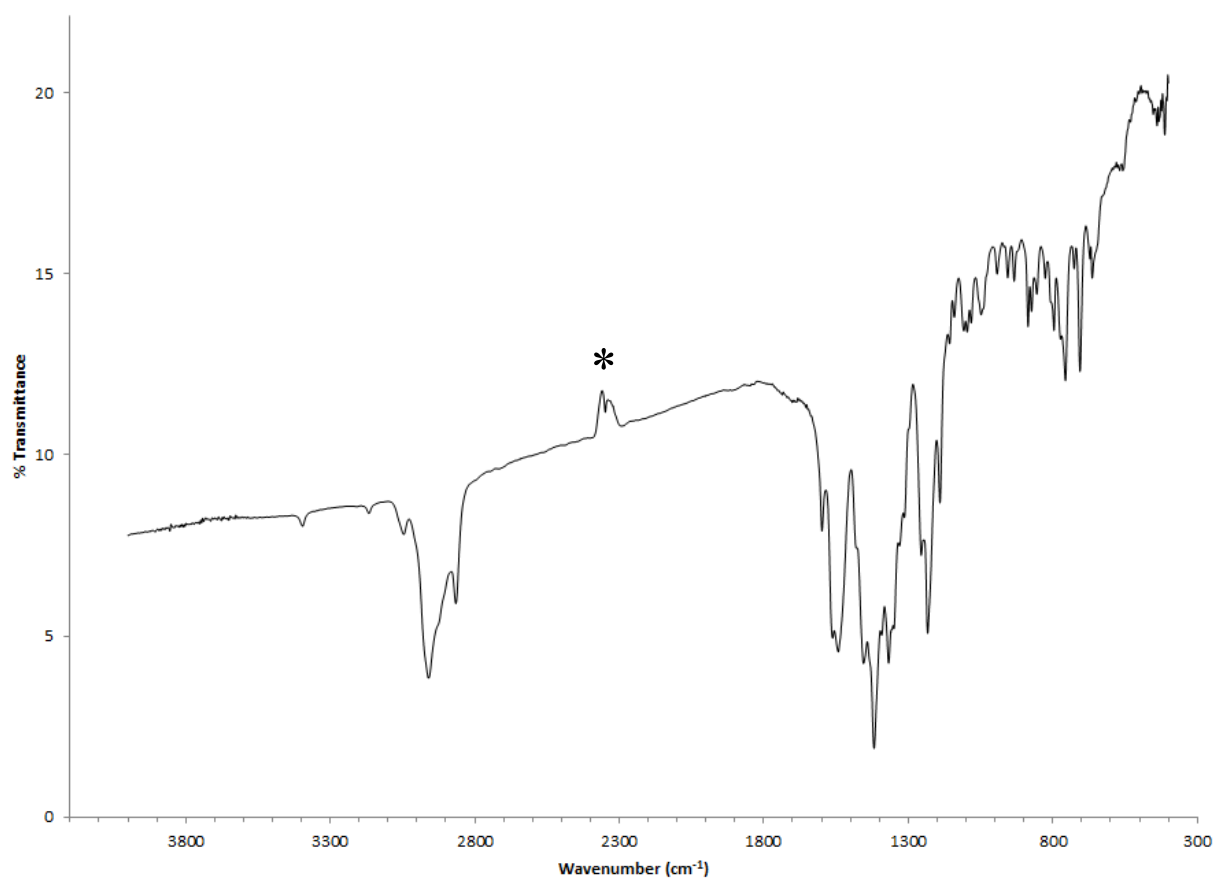


**Figure S48.** IR spectrum (KBr pellet) of **15**. Asterisk denotes background subtraction error.



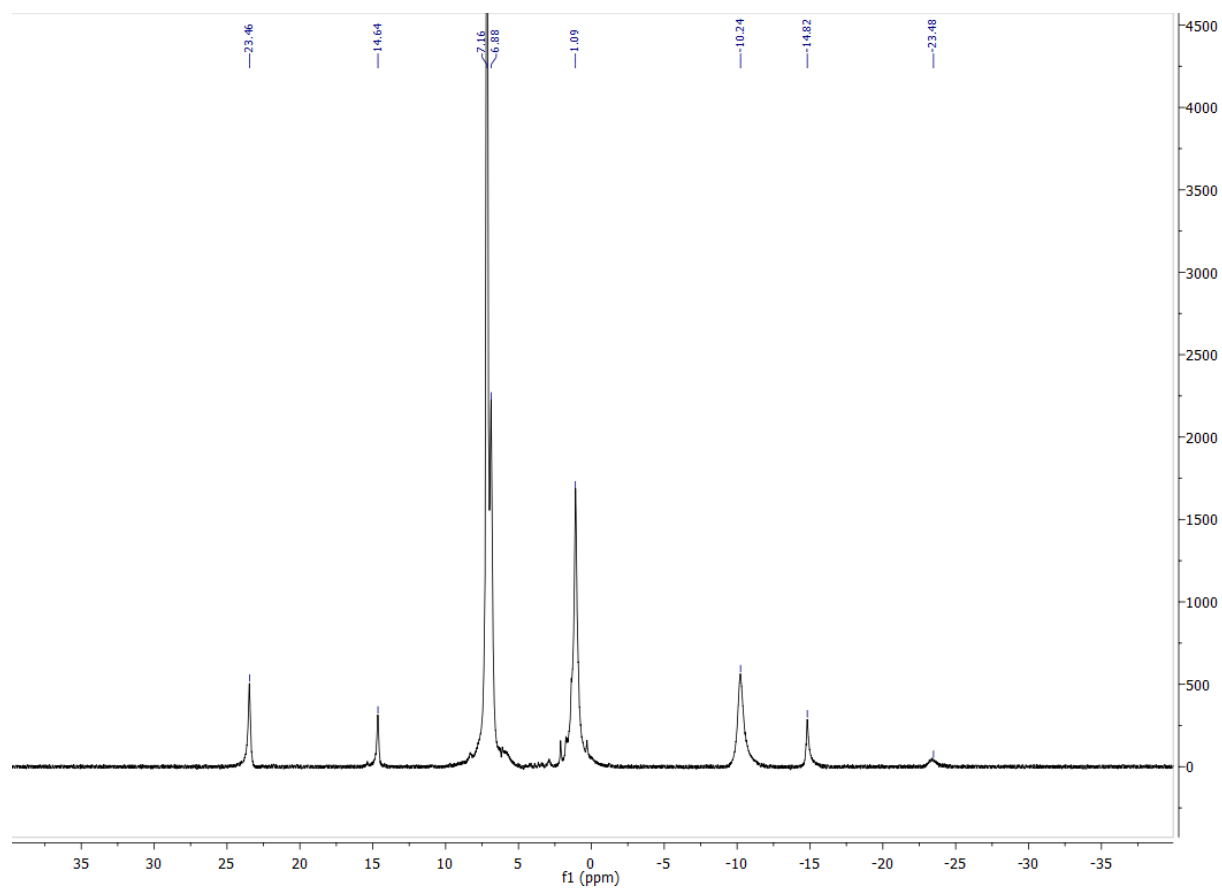


**Figure S49.**  $^1\text{H}$  NMR spectrum of **16** in  $\text{C}_6\text{D}_6$  at  $25^\circ\text{C}$ .

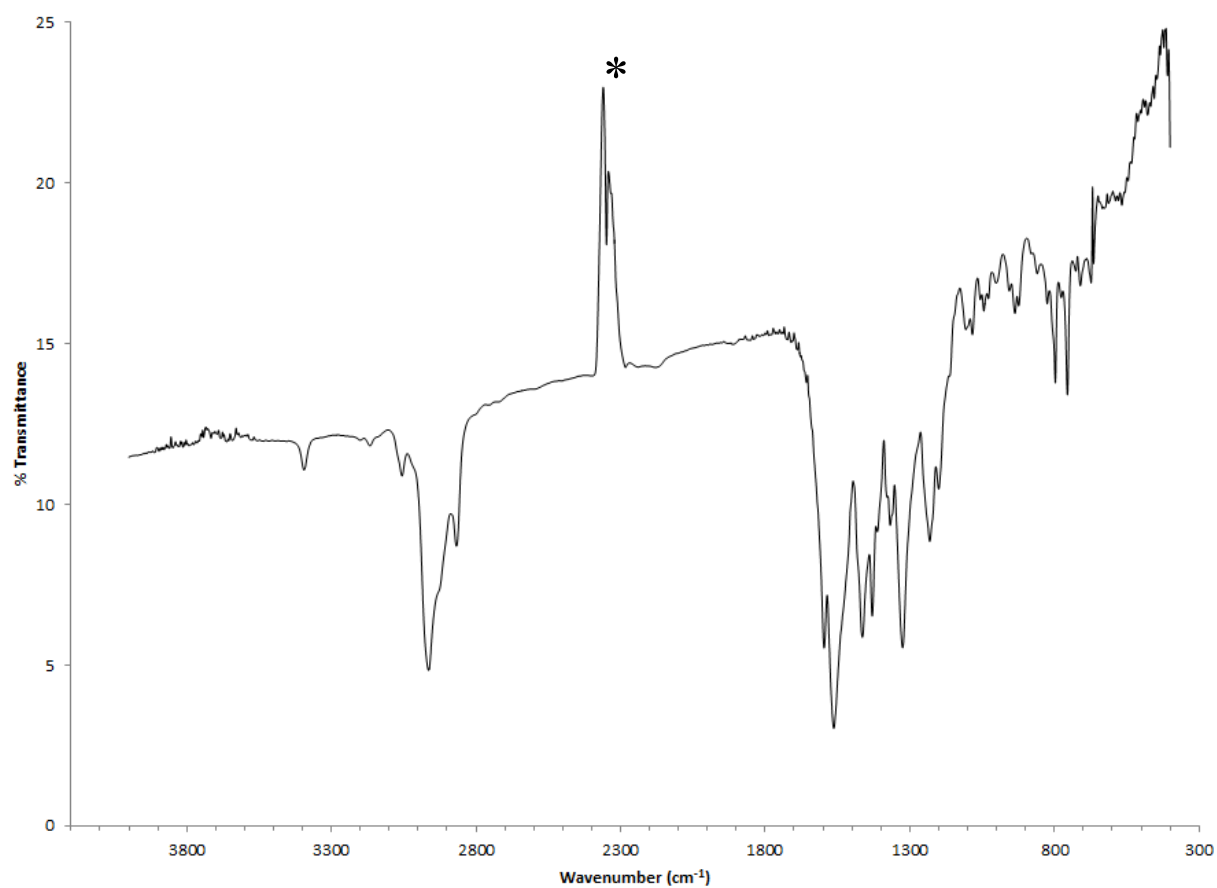


**Figure S50.** IR spectrum (KBr pellet) of **16**. Asterisk denotes background subtraction error.

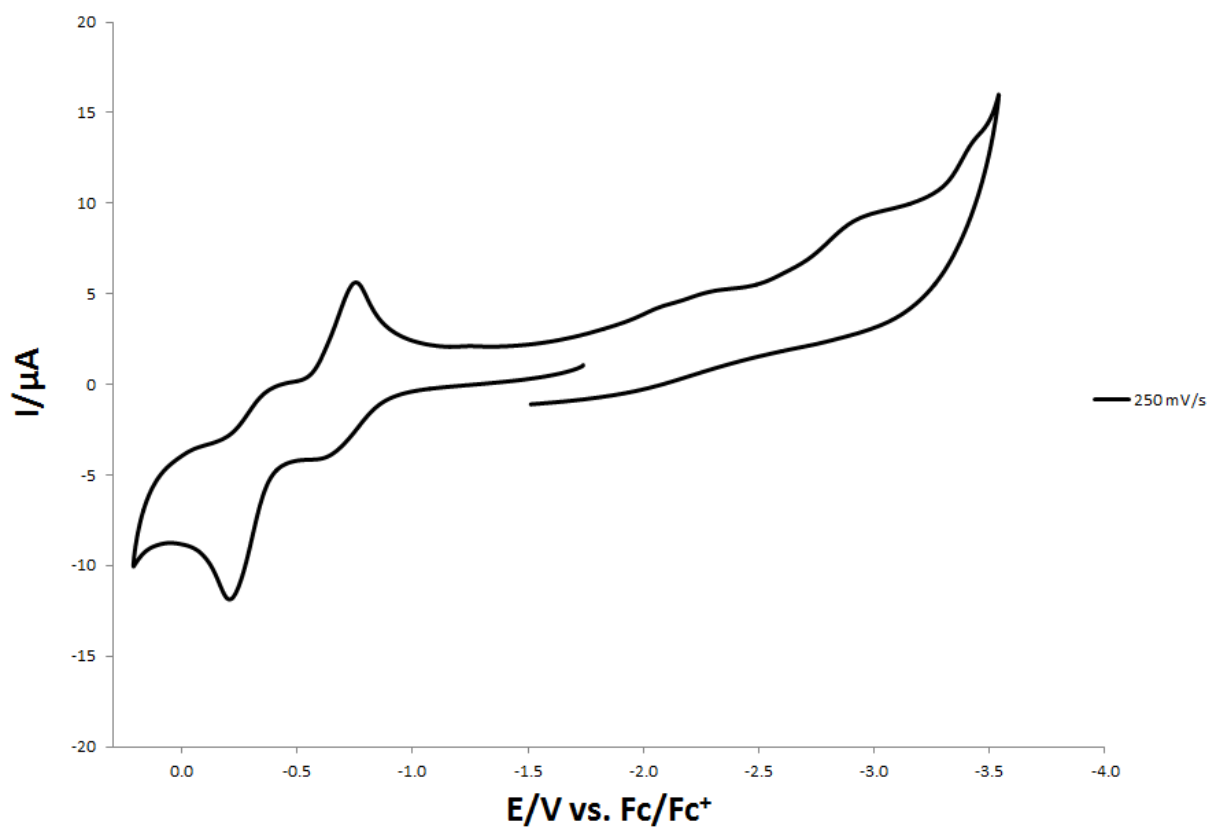


**Figure S51.** Room temperature cyclic voltammogram of **16** in THF vs  $[\text{Cp}_2\text{Fe}]^{0/+}$  using 0.1 M  $[\text{nBu}_4][\text{PF}_6]$  as supporting electrolyte.

**Table S14** Electrochemical data for **16** in Fig. 2.3 in THF (vs. [Cp<sub>2</sub>Fe]<sup>0/+</sup>).

Oxidation feature (4)	Scan rate, V/s	E <sub>p,c</sub> , V	E <sub>p,a</sub> , V	ΔE <sub>p</sub> , V	<i>i</i> <sub>p,c</sub> / <i>i</i> <sub>p,a</sub>
	0.025		-0.251		
	0.050		-0.236		
	0.075		-0.223		
	0.100		-0.213		
	0.150		-0.201		
	0.200		-0.193		
	0.300		-0.18		
	0.400		-0.169		
	0.500		-0.161		
Reduction feature (4)	Scan rate, V/s	E <sub>p,c</sub> , V	E <sub>p,a</sub> , V	ΔE <sub>p</sub> , V	<i>i</i> <sub>p,c</sub> / <i>i</i> <sub>p,a</sub>
	0.025	-0.705			
	0.050	-0.723			
	0.075	-0.732			
	0.100	-0.738			
	0.150	-0.748			
	0.200	-0.757	-0.552	0.205	2.57
	0.300	-0.77	-0.567	0.203	2.29
	0.400	-0.778	-0.6	0.178	2.19
	0.500	-0.788	-0.586	0.202	1.92

## **Vita**

Maximiliano Castillo was born and raised in Juarez/ El Paso, international border between the United States and Mexico. After finishing high school studies at Colegio de Bachilleres de Chihuahua Plantel 5 in Juarez, he envisioned into the journey of college in The University of Texas at El Paso in 2010. In sophomore year, he was admitted to do undergraduate research in the Michael Lab and was co-author of a publication. He received his B.S. of Science degree in chemistry in May 2014 and got accepted to the M.S program in the University of Texas at El Paso under Dr. Skye Fortier mentorship. After publishing 2 articles, he had been recently accepted into the Ph.D. program at Indiana University, expecting to start in August 2016.

Permanent address: 7208 Benson Dr.  
El Paso, TX, 79915

This thesis was typed by Efrain M. Castillo.